DESIGN CONSIDERATIONS FOR HIGH SURFACE-SPEED AND HIGH-LOAD SWITCHED RELUCTANCE MACHINES

DESIGN CONSIDERATIONS FOR HIGH SURFACE-SPEED AND HIGH-LOAD SWITCHED RELUCTANCE MACHINES

By EARL FAIRALL, B.S.

A Thesis Submitted to the School of Graduate Studies

in Partial Fulfillment of the Requirements for the Degree

Doctor of Philosophy of Mechanical Engineering

McMaster University

© Copyright by Earl Fairall, Mar. 2017

McMaster University
Hamilton, Ontario

Doctor of Philosophy (2017)
(Mechanical Engineering)

TITLE: **DESIGN CONSIDERATIONS FOR HIGH SURFACE-SPEED AND HIGH-LOAD SWITCHED RELUCTANCE MACHINES**

AUTHOR: Earl Fairall, Double B.S. (Illinois Institute of Technology)

SUPERVISORS: Ali Emadi, B.S., M.S., Ph. D., Fellow IEEE Canada Excellence Research Chair in Hybrid Powertrain Director, McMaster Institute for Automotive Research and Technology, McMaster University

Nigel Schofield, B.Eng., Ph.D., C.Eng., MIET Professor, Department of Electrical and Computer Engineering, McMaster University

NUMBER OF PAGES: xx, 183

Abstract

This thesis investigates and determines the design considerations to be addressed when designing switched reluctance machines (SRMs) operating at high surface-speeds and high-loads. A new method is introduced to the traditional machine design procedure that captures all of the mechanical, thermal and electro-magnetic considerations for such electric machines. This method is applicable to any motor design; however, is most suitable for machines with rotors that sustain mechanical stresses near the rotor core material limits. The method begins by using common application specifications to identify the maximum diameter and length of a rotor through a series of structural analyses. Maximizing rotor diameter and axial length enables designers to evaluate a machine's theoretical mechanical and electro-magnetic performance limits. The design method is structured such that the designer must use theoretical limits as a constraint for assessing future design decisions which ultimately influence machine cost and performance.

The proposed design method is applied to a case study example typical of a large electric vehicle traction machine, a 22,000rpm, 150 kW switched reluctance machine, while attempting to adhere with design practices commensurate with automotive mass manufacturing. To achieve this, a parallel connected 12/8 pole topology was finally developed. The thesis research suggest that a 440 MPa yield strength, 0.27mm thickness lamination with 30 turn stator coils is sufficient to meet the specification requirements within a prescribed power electronic converter voltage and current constraints, while

satisfying material mechanical and thermal considerations. Detailed analysis of AC effects, performance characteristics, thermodynamics, noise and vibration is presented to simultaneously demonstrate and validate the proposed machine design and design method.

Acknowledgments

This thesis embodies one of the largest PhD student led research initiatives at McMaster Automotive Resource Centre, so I must take this opportunity to thank the countless individuals and entities who have been involved with this research over the years.

First, I would like to thank Dr. Emadi, McMaster University, Canada Excellence Research Chairs Program, the Natural Sciences and Engineering Research Council of Canada (NSERC) Discovery Grants Program, and the Government of Canada for providing me with an opportunity to expand my knowledge as part of McMaster Automotive Resource Centre. Life really is too short to waste on anything less than important. I chose this research subject not only because it interested me, but because I saw it as important. This thesis attempts to address some of the most challenging issues in transportation. The automotive industry is widely considered one of the most difficult industries to institute change due to it's shear size and economic reach. It is my highest hope that this thesis will help change the way engineers think and approach machine design in the automotive industry, or any industry for that matter.

To visiting scholars Koen Moussen, Bas Houben, Daniel Hilgersom, and Jochem Harx: I would like to thank you guys for working really hard on my project. Your work helped improve my understanding of electric machines on multiple fronts. I know my project was a little out of your research area, but I hope you enjoyed getting to research something different while visiting Canada.

Dr. Arun Mitra Phil Woodley: You guys were immensely helpful to me in the beginning of my research. I admit, I was sad when you elected to pursue other opportunities. I trust our paths will meet in the future.

Haoding Li and Jack Gillies: You two are going places, and I am glad I got to work with you. Keep on keepin' on. I have no doubt you will find yourself where you want to be in life.

Martin Wong and Manbir Dhillion: My PhD work was going great until you two came along! Seriously though, you guys helped me discover some issues that took years to fully understand and resolve. It was great getting to work with you guys, and I hope you enjoyed working on my research. I wish you the best luck in the future.

Cody Rheberhegen, Elizabeth Rowan, Jason Lo, and all the technical specialists at canmetMATERIALS: I had not worked with materials engineers on interdisciplinary basis before this project and the Natural Resources Canada Program of Energy Research and Development grant. I am truly honored by the opportunity of getting to work with you guys. I was repeatedly impressed by your ability to interpret and propose novel solutions based on the things I would say, even if I was not expressing myself effectively. I believe our collaborative efforts turned out really great and we should all be proud of that.

Sandra Castano and the folks at SIEMENS/LMS: The biggest hurdle in my research was understanding machine dynamics. It took me literally years of reading and asking questions before I could finally simulate, analyze and interpret vibration results with some level of confidence. The importance of this cannot be understated, since vibrations analysis underpins my entire thesis. Thank you for answering my random questions, regardless of how trivial or silly they were. Thank you for taking the time to help me (and the lab too) learn about things I did not have much knowledge of. Your kindness, patience, and generosity has not gone unnoticed, and I wish you all well in the future.

Engineers at Powersys Solutions: My research is rather broad and covers many different

areas of machine engineering. JMAG and the engineers at Powersys were absolutely crucial to enabling the broad depth of this research. Thank you to everyone who helped process my bug reports and answer my countless questions about JMAG.

McMaster machine shop technicians, mechanical engineering faculty, and my colleagues: There's too many people to name individually, but you know who you are. Thanks for being patient with me and answering all my questions. Your feedback has been invaluable over the years.

Dr. Berker Bilgin: One of my favorite parts of being in the lab was seeing not only the students and department grow, but my supervisors grow as well. I had the unique position of starting at MARC about two weeks before Berker. Berker was instrumental not only in my project, but most of the other projects at MARC over the years. I think back to the beginning of my research and I laugh about how much we both have learned since then. Thank you for your help and support in this arduous pursuit of knowledge.

Dr. Nigel Schofield: By the end of my PhD work, I became more frustrated, short tempered, and burned-out with my work than I have ever been in my life. No one should have to work with me in that condition! I am grateful you looked past all that to help me finalize my work. I am really not sure I would have made it without you. You have an eye for a thesis, and without a shred of doubt had a positive influence on my the work. Thank you for all your efforts.

Lastly, I'd like to thank my family for their endless support and understanding during my time away from home.

Contents

List of Tables

List of Figures

Chapter 1

Introduction

Hybrid and electric vehicles are becoming increasingly prevalent as nations shift away from fossil fuel dependence. Range remains a major challenge facing all-electric vehicle adoptions which are predominately battery powered to date. Improving range can be accomplished by increasing either on-board energy storage capacity, or efficiency at which stored energy is converted to propulsive energy. Increasing energy storage is currently a costly solution as suggested by Table 1.1, where battery price is a significant portion of the vehicle manufacturer suggested retail price (MSRP). The significant expense batteries add

Table 1.1: Comparison of Commercial Electric Vehicles in Production in Model Year 2016

Vehicle	**Range (km)**	**Battery Energy (kWhr)**	**Battery Pack Mass (kg)**	**Battery Cost* ($)**	**Curb Weight (kg)**	**MSRP Base Model ($)**	**Ref.**
Tesla Model S	416	75	544	15,000	2,108	74,500	[8–10]
Nissan Leaf	135	24	294	4,800	1,476	29,010	[11, 12]
Fiat 500 Elec.	135	24	272	4,800	1,352	31,800	[13–15]
Ford Focus Elec.	122	23	303	4,600	1,642	29,170	[16–19]
BYD e6	300	61	600	12,200	2,380	55,000	[20, 21]

*Battery cost estimation based on a constant $200/kWhr [22, 23]

to vehicle cost coupled with historically slow research and development progression has motivated vehicle designers to evaluate alternative methods of extending vehicle range.

Aside from increasing energy storage capacity, several options are available for enhancing vehicle range, which are listed below:

1. Reducing vehicle mass
2. Designing high efficiency powertrain architectures
3. Designing high efficiency powertrain components
4. Reducing auxiliary loads
5. Reducing parasitic loads

Reducing vehicle mass is perhaps the most obvious method of extending vehicle range, and is derived from Newtons Laws of Motion. Moving an object requires more energy per unit mass; therefore, lighter weight automobiles will go further on a specific unit of energy.

High efficiency powertrain architectures could be hybridized systems or battery electric vehicles, although electro-chemical batteries contribute significantly to vehicle mass as shown in Table 1.1. In hybrid vehicles, power production is improved by the addition of electric machines and drives which assist less efficient internal combustion engines and enables regenerative braking capabilities.

Range can also be improved by increasing the powertrain efficiency on a component level. Reducing loss in engines, machines, transmissions, differentials and bearings will improve energy consumption significantly over the vehicle lifetime.

Auxiliary loads are devices not generally critical to power production; however, are necessary for successful operation of the vehicle itself. Several examples of auxiliary loads are oil pumps, alternators, fuel pumps, cooling pumps, radiator fans, windshield wipers, heating, ventilation and air-conditioning (HVAC) systems. Reducing energy consumption of these types of devices permits more energy use for propulsion itself.

In the context of this thesis, parasitic loads refer to auxiliary systems which impact the efficiency of other components. In traditional internal combustion engine vehicles, auxiliary loads are typically driven by the engine itself; therefore, effectively all auxiliary loads can be considered parasitic loads; however, for battery electric vehicles, auxiliary and parasitic loads are not necessarily mutually inclusive. For example, an alternator takes energy from an internal combustion engine to power vehicle electrical systems. There is, of course, some loss in this energy conversion process. On the other hand, in electric vehicles, HVAC systems consume energy; however, they do not have to be driven by the primary propulsion device. In this case, the HVAC system; therefore, does not directly reduce efficiency of the primary propulsion device. While efficiency of the propulsion system would be unaffected, vehicle range will still be impacted since both systems are powered from the same electrical energy source. It follows that maximizing electric vehicle range entails careful design of all systems to minimize auxiliary and parasitic loads.

Ultimately all the methods listed for improving range can be positively influenced with the use of more expensive material and manufacturing methods for each system; however, minimizing cost is necessary to maintain consumer afford-ability, especially in high volume manufacturing applications typical of the automotive industry. Due to the conflicting nature of cost and efficiency of a machine, meeting both design requirements can be a delicate balance and very challenging to achieve.

In order to enable the electric mobility revolution, an overarching strategy of minimizing powertrain mass by investigating high-speed propulsion systems has been proposed. The reduced-mass benefit of high speed propulsion systems can be realized from the general torque and power equations for electric machines [24, 25] which respectively are:

$$\tau = \frac{\pi}{2} D^2 L B_{avg} Q \tag{1.1}$$

$$P = \tau \omega_r \tag{1.2}$$

where B_{avg} is average airgap flux density, or magnetic loading, with units $\frac{kg}{s^2 A}$; Q is the electrical loading in $\frac{A}{m}$; D and L are the machine airgap diameter and active axial length in meters and $\omega_r$the machine rotation speed in radians per second.

From Eqn. 1.1, it can be seen that for a given magnetic and electrical loadings rotor volume is directly related to maximum torque. From Eqn. 1.2, shaft power is a product of rotational velocity and torque, average airgap flux density and electrical loading remain approximately constant for two machines of a given power requirement and differing speed ratings. As a result, increasing the designed speed of the machine could result in a decrease in the main dimensions of the machine i.e. diameter and or length. Of course, in a physical context, reduced machine length or diameter corresponds to decreased machine mass.

1.1 Electric Machine Power Limit

Transportation industries are increasingly interested in electric machines with low cost and high specific power to enable the electric mobility revolution. As mentioned, low cost is necessary to maintain consumer affordability, while large specific power decreases vehicle mass and enhances range of a given energy storage system. Cost and specific power are competing parameters, especially in high volume manufacturing applications typical of the automotive industry. Therefore, meeting both design requirements can be very challenging.

Interestingly, both specific power and cost can be related by machine power limit. For example, highest specific power is the smallest mass machine with the largest power limit. Additionally, the best value electric machines are those with lowest cost and largest power capability. If an application power requirement is specified, both cost and specific power could be optimized based on the machine power limit; therefore, a method of evaluating power limit presents value for machine design optimization.

Power is constrained by mechanical and electro-magnetic relationships. Relating power to the theoretical mechanical and electro-magnetic envelopes of a machine is shown conceptually in Fig. 1.1, here machines with an electromagnetic envelope greater than the mechanical envelope, represent situations where mechanical failure occurs before the entire magnetic envelope can be realized (a). Conversely, machines with mechanical potential greater than electro-magnetic potential describes situations where machines are physically capable of speed or torque greater than electro-magnetics allow (b); while machines at their mechanical limit, where electro-magnetics and control are optimized to coincide with the structural envelope are shown in (c). Certain damage or failure results from operation beyond these envelopes, thus Fig. 1.1 (a) and (b) will have a lower power capability than Fig. 1.1 (c).

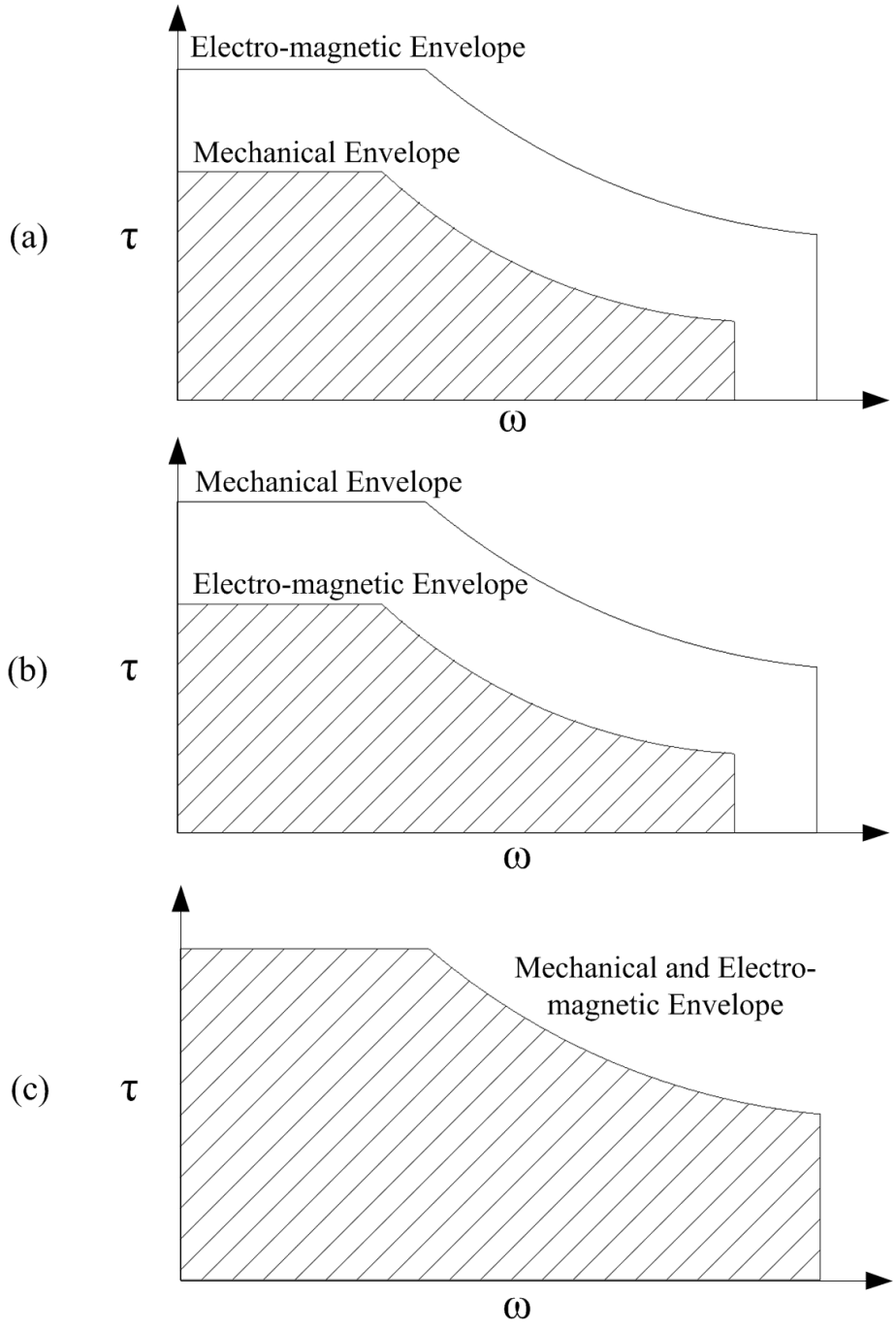

Figure 1.1: Theoretical electro-magnetic and mechanical torque versus speed envelopes for machines with usable area shaded (a) Electro-magnetic larger than mechanical (b) Mechanical larger than electro-magnetic (c) Coincident structural and electro-magnetic envelopes.

Fig. 1.1(b) is the most common case. Application requirements are less than the machine's mechanical capability. Fig. 1.1(b) suggests the usable envelope could be achieved with differing machine designs. For example, if core material strength is of minimal importance, identifying minimum required material strength will result in more coincident structural and magnetic envelopes. Such mechanical identification provides design flexibility because lower strength material may be lower cost, have better magnetic characteristics, or both.

Characterizing machines as high-speed or high-power can be misleading. Researchers have attempted to disambiguate these terms with empirical relations between speed and peak power capability. Maeda et al, describes the limiting boundary between high-speed and super high speed electric machines [2, 26] as:

$$P_{kW}\omega_{krpm}^{3.3} \leq 6.2 \times 10^{6} \tag{1.3}$$

Where P_{kW} and ω_{krpm} are the peak power in kW and speed in krpm, respectively.

Van Millingen et al introduce dynamic speed, a numerical parameter described by:

$$\omega_{rpm}\sqrt{P_{kW}} \tag{1.4}$$

Where ω_{rpm} is rotation velocity in rpm and P_{kW} is peak power in kW. Eqn. 1.4 is used as a guide number to assess possibility of dynamic challenges such as critical speeds, material stress, peripheral velocity and balance sensitivity [4].

Moghaddam introduces a high-speed index [5]:

$$\omega_{rpm}P_{kW} \tag{1.5}$$

Using empirical relations, Moghaddam shows that:

$$P_{kW} \propto Diam_{rotor}^{2.6} \tag{1.6}$$

While the empirical relations help deduce power limits for the existing state-of-the-art, they present little information on how to achieve power limit. Nor are the relations particularly useful for evaluating power limit in novel machines, as can be deduced from Fig. 1.4.

Binder and Schnieder [7] discuss rotor surface speed as a benchmarking and design parameter. The major drawback of surface speed as a benchmarking parameter is that commercially available motors often do not provide geometric details of the rotor in technical specification sheets, so surface speed cannot be accurately calculated. In the context of machine design, surface speed is important for indicating the level of stress in the rotor [7]. A large surface speed could indicate rotors with a small diameter and large rotational velocity, a large diameter and small rotational velocity, or anywhere in between.

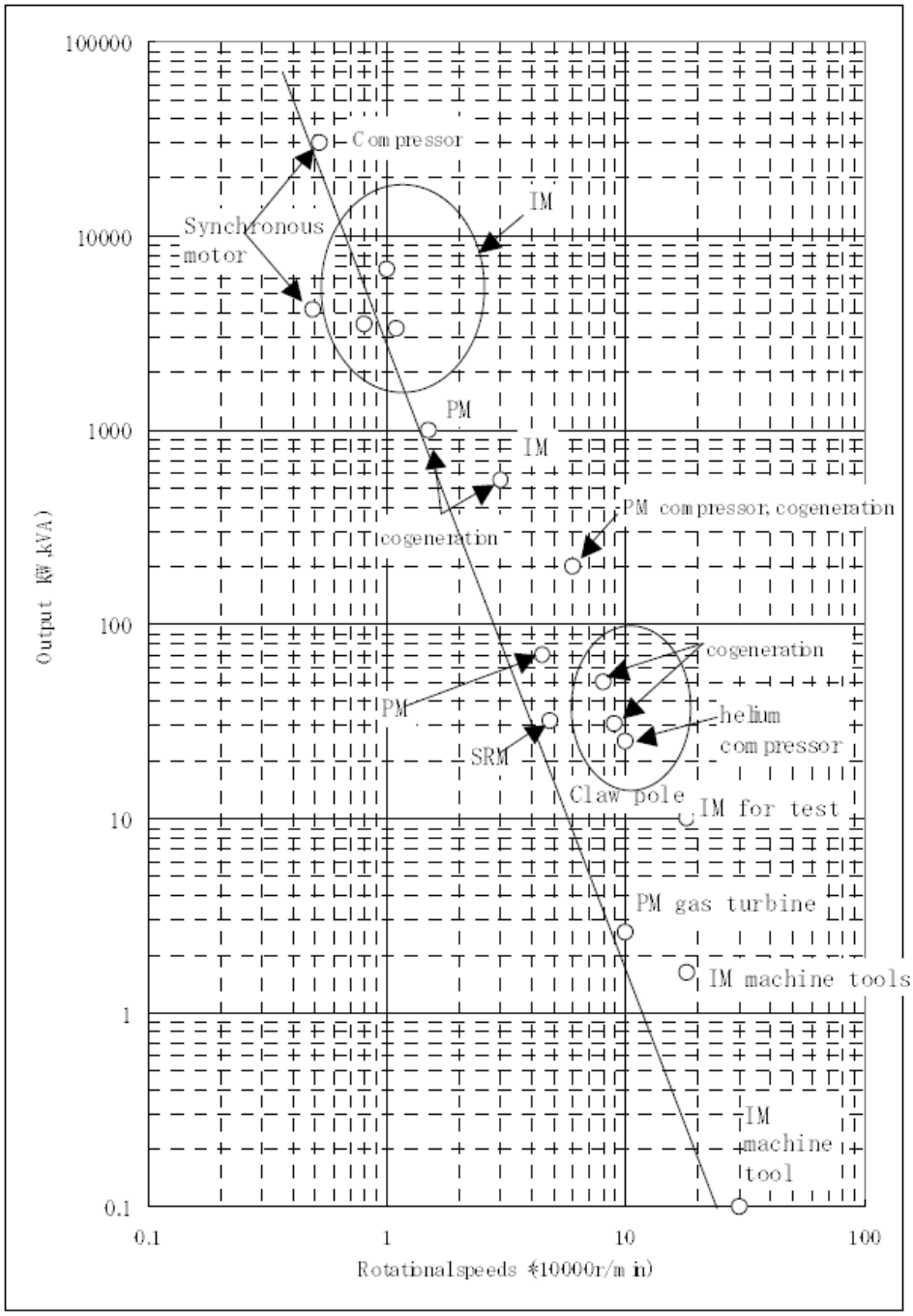

Figure 1.2: Speed versus power plot for different machine topologies by Rahman [1], with linear correlation from Maeda [2].

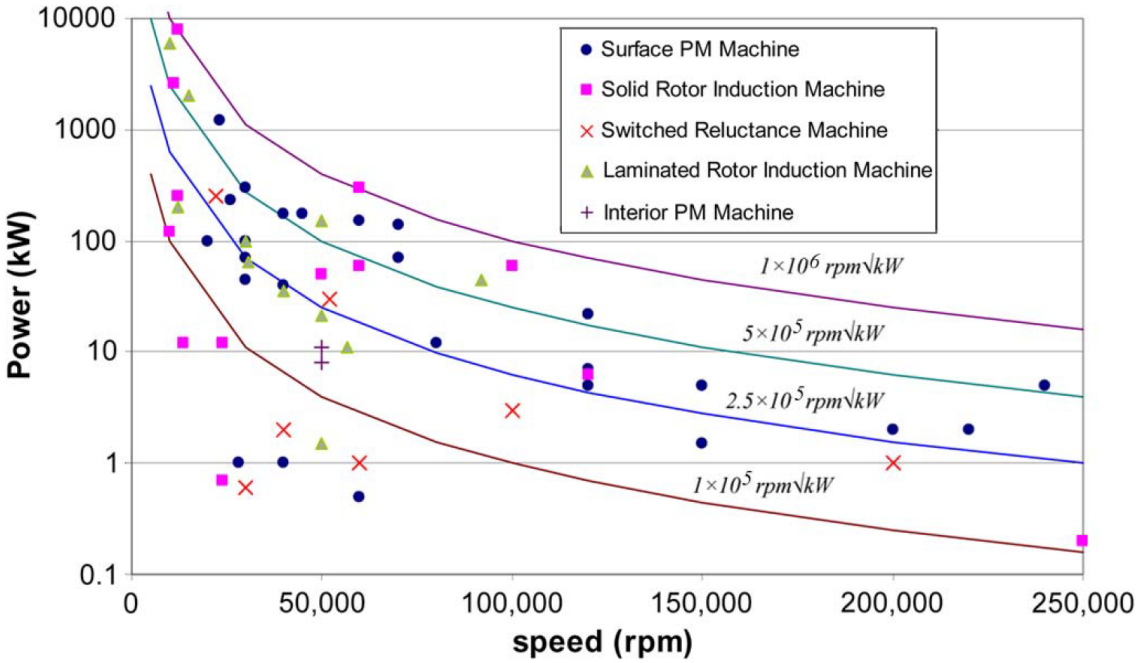

Figure 1.3: Speed versus power plot for different machine topologies by Gerada [3], with non-linear rpm$\sqrt{kW}$ correlations as proposed by van Millingen [4].

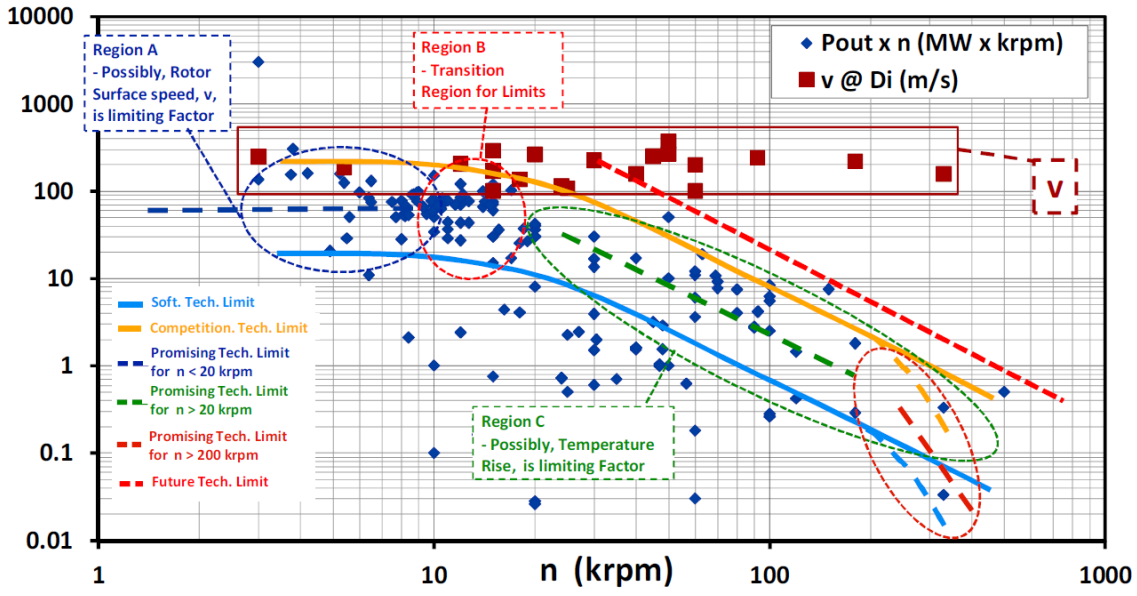

Figure 1.4: Plot of Speed versus High-Speed Index by Moghaddam for various machine topologies [5].

1.2 High Speed SRMs in Industry

When considering motors for high speed application, the system requirements and machine attributes must be thoroughly evaluated. Gerada et al. provides an overview of high speed electric machines [3]. One conclusion that can be drawn from this work is that no machine can be easily developed for high speed application. Every machine topology has trade-offs which makes high speed operation difficult. Surface and interior permanent magnet motors require containment bands and significant attention to rotor cooling to prevent the magnets from overheating and demagnetizing [27, 136]. Containment bands require larger airgaps and can produce parasitic loss, both of which can reduce machine efficiency [28–30]. Rotor cooling can be a challenging part of the motor to address because it is not a static component, and modes of heat transfer are generally limited to conduction via the shaft or convection to the air [136]. In recent years, rare-earth permanent magnets have been subject to significant price variation, shaking electric machine industries with the cost per kilogram spiking more than 10 times higher than the normally anticipated price due to supply restrictions [31, 32]. High speed induction machines can suffer from reduced efficiency [3], necessity to use specialty materials such as beryllium copper [33], and have reliability challenges [34, 35] all which extend from rotor complexities.

While permanent magnet (PM) and induction machines are mature technologies, switched reluctance motors boast a number of advantages over alternative motor topologies such as fault tolerance, potentially low cost, and robust design. Fault tolerance of switched reluctance machines has been thoroughly investigated in both the motoring and generating environments, driving their adoption in the aerospace industry [36, 37]. SRMs have electrical phase isolation which by itself puts SR technology above competing motor technologies from a reliability perspective. In addition to phase isolation, reluctance machines have no rotor field windings or permanent magnets. Not having a rotor field is

both a positive and negative attribute. Negative, in that rotor fields generally improve specific power. Positive, in that back-electromotive force (back-EMF) is not physically produced, since back-EMF can be problematic in the event of a system fault. Rotor excitation can present a fire hazard as power can be generated in a faulted phase [38]. Beyond the machine, power electronic control of SRMs via an asymmetric bridge offers another layer of fault tolerance by not suffering from shoot through faults as with traditional AC phase-leg converters [38].

The SR machine construction itself is another major advantage for the motor. The rotor can be simply comprised of laminated electrical steel and shaft. Unlike PM or induction machines, there are no additional components which add complexity to the mechanical or electrical design process. Rotor thermal limitations are also less stringent compared to induction or PM machines, because temperature imposes mechanical limitations from degradation of lamination insulation material, or degradation of the core material yield strength itself, the latter of which is really only a theoretical limit for most practical applications [39].

In addition to fault tolerance and robust construction, reluctance motors are widely considered to be a low cost electrical drive [40]. Concentrated windings can be formed externally and inserted to the stator [41]; core laminations can be fabricated and assembled like any traditional laminated core, and the rotor has no windings, magnets, slip rings, or commutators [40]. The drive is often a larger contributer to cost than the machine, and is the subject of considerable research, because it is dictated by many parameters including number of switches, converter topology, reliability requirements, voltage, current, and other performance ratings [42].

High reliability, robust construction and low cost are the driving attributes behind finding performance and cost benefit in high speed switched reluctance machines over other motor topologies. These attributes suggest SR technologies may be more

economical than comparable PM or induction machine technologies in what might normally be considered an aggressive environment. Switched reluctance machines (SRMs) will, therefore, be further investigated in this thesis as a low cost drive at high-surface speed and load.

A comprehensive listing of SRMs operating above 20,000rpm is shown in Table 1.2 by order of increasing power output. The application is listed in addition to a number of details about each machine. High speed switched reluctance machines are being researched for a number of present and future industrial applications. The highest power high-speed SRMs in literature are integrated engine starter-generators (IESG). IESGs are found on the high pressure spool of a gas turbine, where temperatures, pressures and shaft rotational velocities are most harsh. Other common research applications include switched reluctance generators (SRG), pumps, and machine tool spindles.

From Table 1.2, the state-of-the-art suggests high speed machines with reasonable peak efficiency above 90% are possible. Many publications do not list efficiency, despite manufacturing and testing a prototype, presumably because accurate torque measurement is challenging and expensive at high speed. Machines tend to have a low pole count likely to improve efficiency by reducing core loss; however, Richter et al. was able to achieve and verify 89% efficiency with a 250kW, 12/8 machine [43].

Table 1.2: List of high speed SRMs by power output

Power (kW)	**Speed (krpm)**	**rpm$\sqrt{kW}$**	**Voltage (VDC)**	**Poles N_S/N_R**	**Efficiency Mot/Gen (%)**	**Steel Stator/Rotor**	**Application**	**Ref.**
0.1	750	2.37×10^5	108	6/4	73*	Metglas 2605SA1	Micro Machining	[44]
0.12	30	1.04×10^4	160	6/4	80@7kRPM	M250-35A	Textile Spindle Drive	[45]
0.12	40	1.39×10^4	310	6/6	-	-	Vacuum Pump	[46, 47]
0.223	50	2.36×10^4	12	6/4	75*	29 Gauge M15 C5	Toroidal Coil Demo	[48, 49]
0.28	60	3.17×10^4	60	16/8	78	Mn-Zn Ferrite/Vitrovac 6025	SRG	[50]
0.5	30	2.12×10^4	150	8/6	-	-	Bearingless Demo	[51–54]
0.63	40	3.17×10^4	150	4/2	72@30kRPM	35PN210	Air Blower	[55–58]
1.0	48	4.80×10^4	-	4/2	-	-	-	[59]
1.0	50	5.00×10^4	250	4/2	-	-	-	[60, 61]
1.0	60	6.00×10^4	250	4/2	-	-	Vacuum Pump	[62]
1.0	200	2.00×10^5	-	6/2	-	-	-	[63]
1.7	24	3.13×10^4	75	12/2	85	-	SRG	[64, 65]
1.7	50	6.52×10^4	50	6/4	-	35A300	E-Supercharger	[66]
2.0	150	2.12×10^5	50	6/4	93	6.5% Silicon 0.1mm	-	[67]
5.0	100	2.24×10^5	96	6/4	-	V300 0.35mm/CK-26 0.5mm	E-Supercharger	[68]
30	50	2.74×10^5	270	6/4	89@20kRPM	M270-35A	IESG	[69–74]
32	48	2.72×10^5	270	6/4	89/93	Iron Cobalt Vanadium 0.15mm	IESG	[75–78]
45	32	2.15×10^5	270	6/4	$<$96*	-	IESG	[79]
60	50	3.87×10^5	600	6/4	91@10kRPM*	M250-35HS	Automotive Traction	[80, 81]
90	25	2.37×10^5	270	6/4	-	Iron Cobalt Vanadium	Fuel Pump	[82, 83]
100	100	1.00×10^6	600	6/4	35.2*	4340	SRG	[84]
127	30	3.38×10^5	-	6/4	96.4*	TKES M235-35A	Automotive Traction	[85]
250	22.2	3.51×10^5	270	12/8	89	Iron Cobalt Vanadium	IESG	[43, 86–89]
300	30	5.20×10^5	600	6/4	90.8*	M-15	SRG	[84]
300	30	5.20×10^5	600	6/4	90.4*	M-15	SRG	[84]
300	60	1.04×10^6	600	6/4	62.7*	4130	SRG	[84]
300	100	1.73×10^6	600	6/4	40.0*	4340	SRG	[84]

*estimated value -Undefined value

1.3 Thesis Contributions

This thesis has three primary research aims that define the contributions of the research study. The first contribution is an investigation into the merit of high-speed switched reluctance machines. A review of the state-of-art is presented in Chapter 2, where all switched reluctance machines and drives that operate above 20,000rpm are investigated. Machines range from 100W to 300kW; 22,000rpm to 750,000rpm, for applications ranging from spindle drives to gas turbine starter-generators. This Chapter aims to compile all the challenges and solutions relevant to switched reluctance machines operating above 20,000rpm, from machine design to power electronics and control.

Based on the conclusions from Chapter 2, the second contribution is the proposal of a new design methodology for switched reluctance machines. Introduced in Chapter 3, the design methodology recommends initial machine electromagnetic sizing based on Krishnan [90] or similar, followed by a series of structural analyses on the rotor, which identify the maximum possible rotor volume for a chosen magnetic material. Structural analysis is followed by stator design and electromagnetic performance analysis in Chapter 4. Here, electromagnetic transient analysis is conducted to evaluate magnetic performance envelope, torque ripple, and electro-magnetic losses. Additional analyses are also suggested to help identify and minimize losses brought about in high frequency machines by manufacturing and assembly practices.

Once the electro-magnetic loadings, magnetic and mechanical loss and distribution have been defined from Chapters 3 and 4, thermal, noise and vibration analysis can be conducted. Chapter 5 describes the cooling systems considered, thermal analysis, and a strategy for minimizing parasitic losses created by the thermal system. Chapter 6 demonstrates noise and vibration performance analysis.

This new design methodology is demonstrated in Chapters 3 through 6 by case example

of a 22,000rpm 150kW switched reluctance machine considered as a primary traction drive for automotive application. This machine design strives to be commensurate with industry design and mass manufacturing practices.

The final thesis contribution is an electro-magnetic, noise and vibration comparison of two three-phase SRM topologies, a 12/8 and a 12/10 SRM. In Chapter 6, the 12/10 was considered as a possible improvement to the 12/8 topology, since it offers shorter flux paths and more rotor poles than the 12/8, suggesting that torque ripple, core loss, noise and vibration could potentially be lower. A thorough comparison of 12/10 and 12/8 pole topologies was not found in literature.

Finally, Chapter 7 concludes the thesis and presents suggestions for future research.

Chapter 2

State-of-the-Art Switched Reluctance Machines Speed-Rated Above 20,000rpm

2.1 Fundamentals of SRM

Switched reluctance machines operate on the physics principle of reluctance torque. Reluctance in magnetic circuits is analogous to resistance in electrical circuits. Reluctance, R, is defined as:

$$R = \frac{l}{\mu_0 \mu_r A} \tag{2.1}$$

where l and A are the magnetic circuit length and circuit cross sectional area, respectively, μ_0 and μ_r are the permeability of a vacuum ($4\pi \times 10^{-7}$) and permeability of the material respectively.

Reluctance is then related to magnetic circuits by Equation 2.2. Where $M.M.F.$ is the magnetomotive force in Ampere-turns and Φ is magnetic flux in Webers:

$$R = \frac{M.M.F.}{\Phi} = \frac{Ni}{\Phi} \tag{2.2}$$

Fig. 2.1 shows a simple actuator device manufactured from soft ferromagnetic material in the shape of a horseshoe with a keeper bar in (a) and a rotary reluctance circuit in (b). Here, the magneto-motive-force ($M.M.F.$) is developed by a coil of N turns pulsing a current of i Amperes. This $M.M.F.$ creates a magnetic flux, Φ, which circulates through the airgap, horseshoe and keeper bar reluctances R_g, R_1 and R_2.

The flux-linking the coil, λ, is given by:

$$\lambda = \Phi N \tag{2.3}$$

Fig. 2.2 shows the $\lambda - i$ diagram for the simple horseshoe magnetic circuit with the keeper in two positions, closed (or aligned) and open (unaligned). Coenergy defined as the area beneath the $\lambda - i$ characteristic curve, whereas stored field energy is defined as the area above the $\lambda - i$ characteristic curve, as shown in Fig. 2.2. Here, co- and stored energy for the aligned position are represented by a vertical hatch pattern, whereas co- and stored energy for the unaligned position are represented with a horizontal hatch pattern.

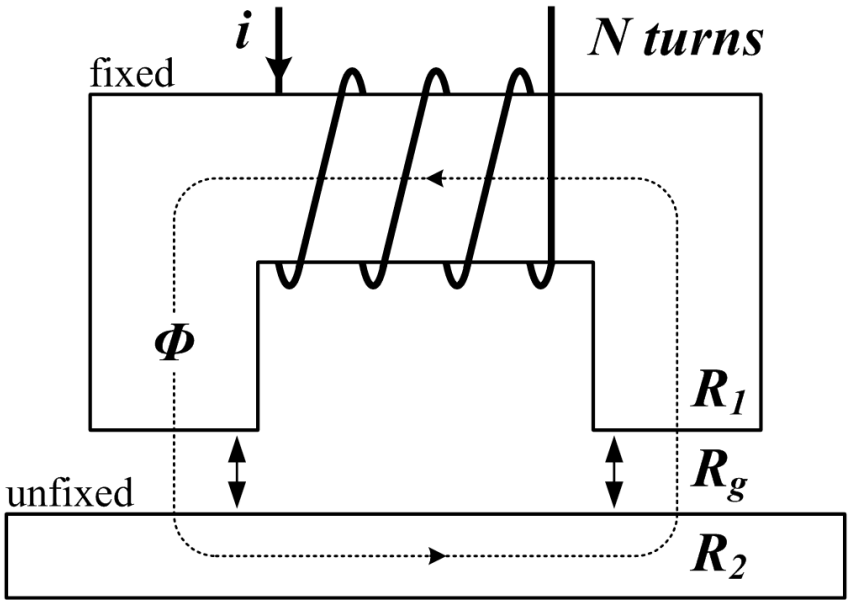

(a)

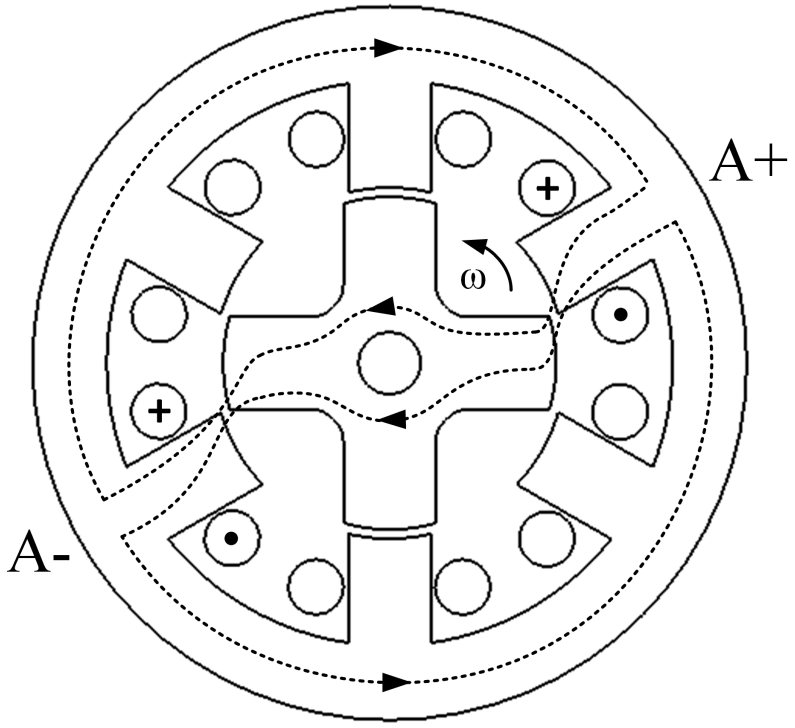

(b)

Figure 2.1: Simple magnetic circuit diagram for a (a) horseshoe and keeper bar made of soft ferromagnetic material (b) rotary machine implementation 6/4 SRM.

Substituting Eqn. 2.2 into Eqn. 2.3 yields:

$$\lambda = \frac{N^2 i}{R} \tag{2.4}$$

Where the change in coil flux-linkage due to current flowing through the coil is defined as the coil self-inductance:

$$L = \frac{\lambda}{i} = \frac{N^2}{R} \tag{2.5}$$

Sometimes expressed as:

$$L = \frac{\lambda}{i} = N^2 P \tag{2.6}$$

Where P is the magnetic circuit permeance.

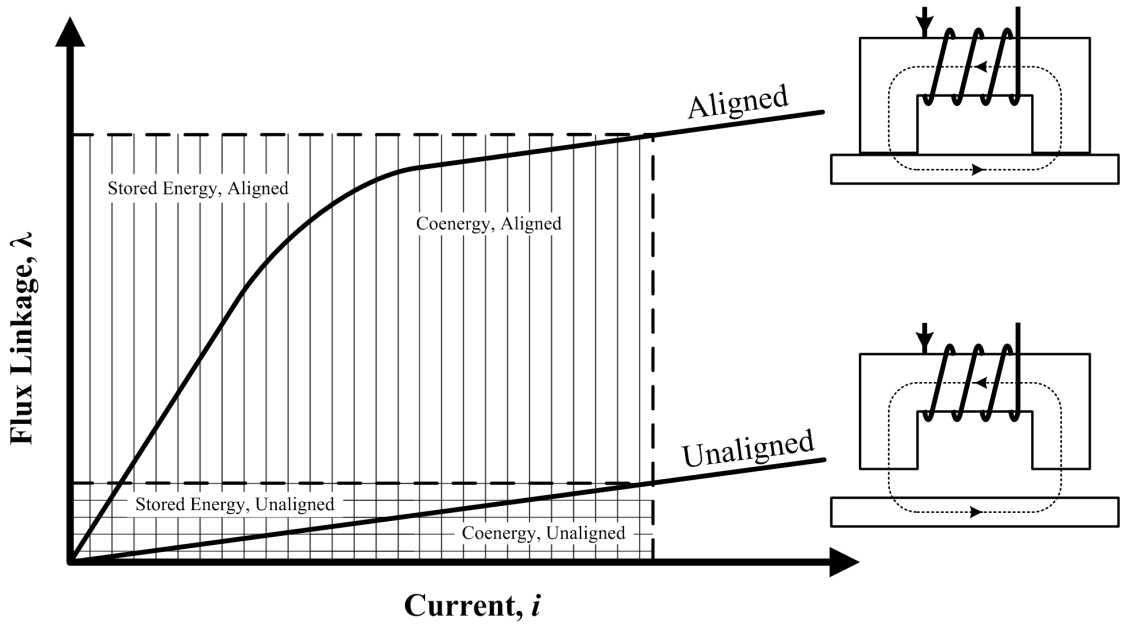

Figure 2.2: Flux-linkage versus current plot for the horseshoe and keeper bar.

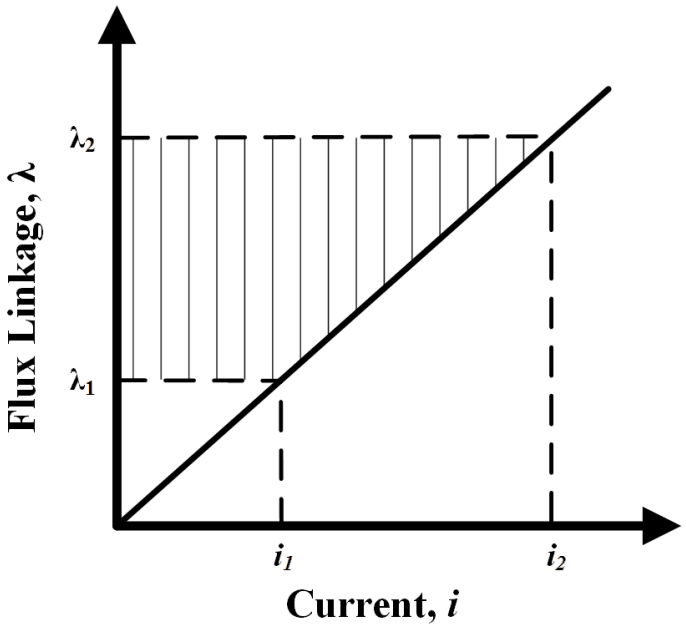

Figure 2.3: $\lambda - i$ diagram demonstrating a change in current and the corresponding change in flux linkage for an unsaturated soft ferromagnetic material.

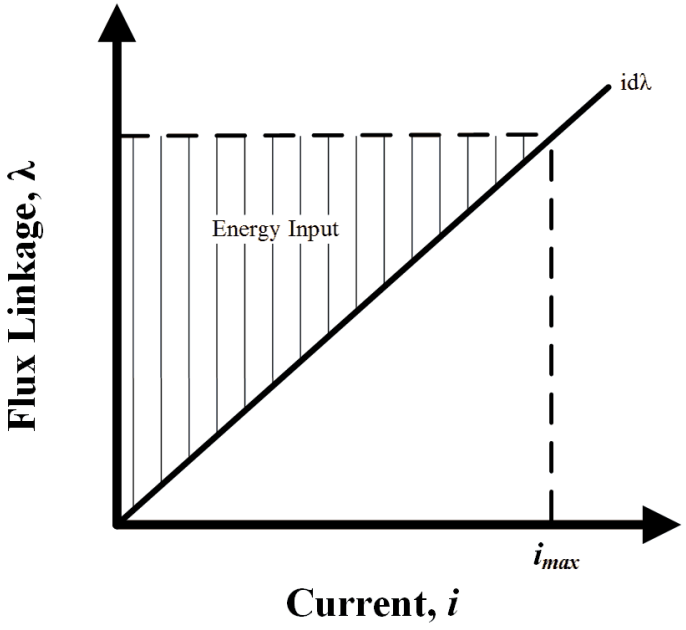

Figure 2.4: $\lambda - i$ plot from $i = 0$ to $i = i_{max}$ for an unsaturated soft magnetic material.

If the variation of flux linkage with current is as in Fig. 2.3, then the change in stored energy is given by the shaded area.

If the current is increased from zero to i_{max} as shown in Fig. 2.4 then energy input is:

$$w = \frac{i\lambda}{2} \tag{2.7}$$

Rearranging and substituting Equation 2.5 into Equation 2.7 yields:

$$w = \frac{i^2\lambda}{2} \tag{2.8}$$

The area under the $\frac{\lambda}{i}$ characteristic is known as co-energy. The change of co-energy in time interval dt is given by:

$$dw' = \lambda di \tag{2.9}$$

For a linear system, stored field energy is equivalent to the co-energy as shown in Fig. 2.5a. However in nonlinear systems, this will not be the case as shown in Fig. 2.5b. Compared to the linear system, the energy for a given i_{max} will be less for the nonlinear system. Saturated operation is an important feature of SRM technology, most other machine technologies operate in their magnetic linear region.

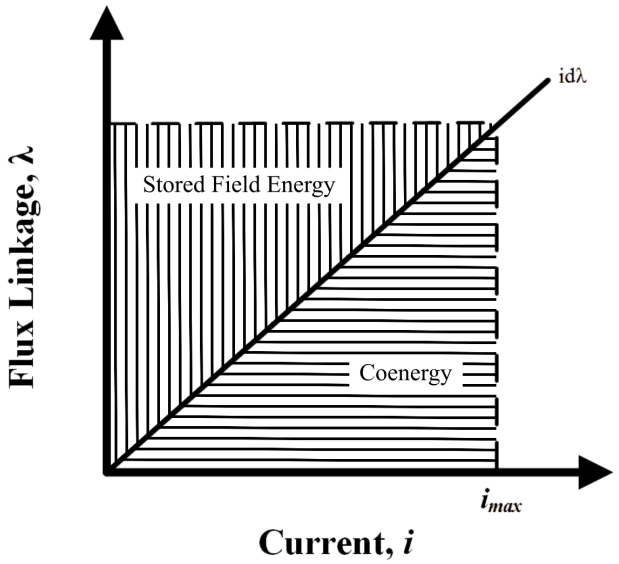

(a)

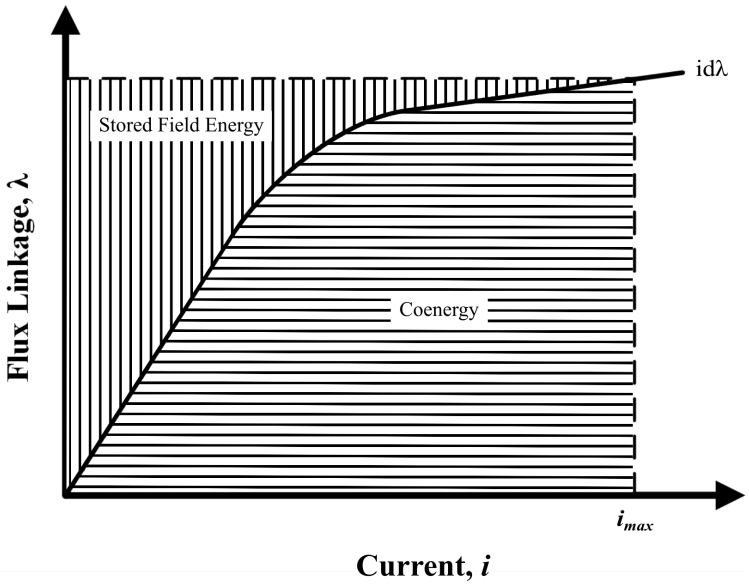

(b)

Figure 2.5: $\lambda - i$ diagram for a (a) linear (unsaturated) (b) non-linear (saturated) ferromagnetic material.

2.1.1 The Electrical Equivalent Circuit

A switched reluctance machine has a simplified representation as an inductor, phase resistance and back-electromotive force source, as shown in Fig. 2.6.

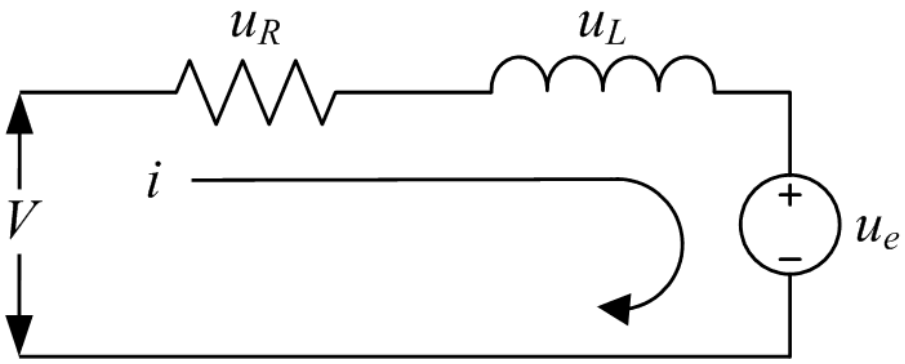

Figure 2.6: Equivalent circuit for a single phase in a switched reluctance machine.

The equivalent circuit can be represented mathematically by:

$$V = Ri + \frac{d\lambda(\theta, i)}{dt} \tag{2.10}$$

and flux-linkage is given by [90, 91]:

$$\lambda = L(\theta, i)i \tag{2.11}$$

where $L(\theta, i)$ represents inductance at an instantaneous current and position, ω is rotational frequency, V and R are the phase voltage and resistance respectively. Equation 2.10 can be expanded to yield:

$$V = \underbrace{Ri}_{u_R} + \underbrace{L(\theta, i)\frac{di}{dt}}_{u_L} + \underbrace{\frac{idL(\theta, i)}{d\theta}\omega}_{u_e} \tag{2.12}$$

2.1.2 Operation of an SR machine

For the rotary SRM, consider one stator tooth and one rotor tooth of an electrical machine in which the only torque producing mechanism is a reluctance torque, e.g. switched reluctance machine.

Rotor teeth are pulled into alignment with stator teeth by stator currents as illustrated in Fig. 2.7. Direction of rotation is independent from current polarity as shown in Fig. 2.8. Clearly, the reluctance of the magnetic circuit will be lowest in the aligned position. Neglecting saturation, the $\lambda - i$ diagram of the two positions takes the form illustrated in Fig. 2.9.

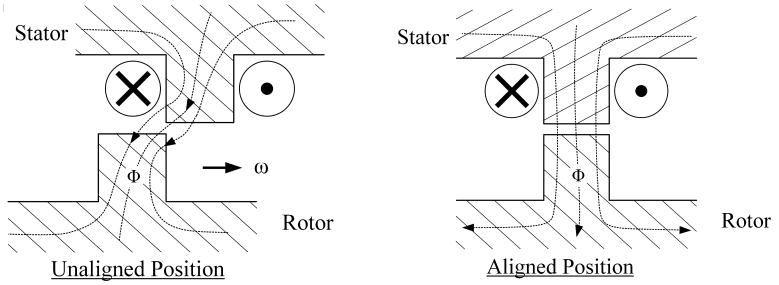

Figure 2.7: (a) unaligned and (b) aligned rotor position.

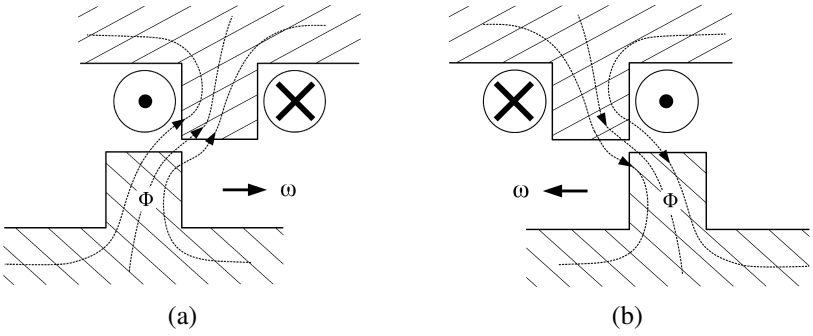

Figure 2.8: Bidirectional operation independent of current direction (a) clockwise (b) counterclockwise.

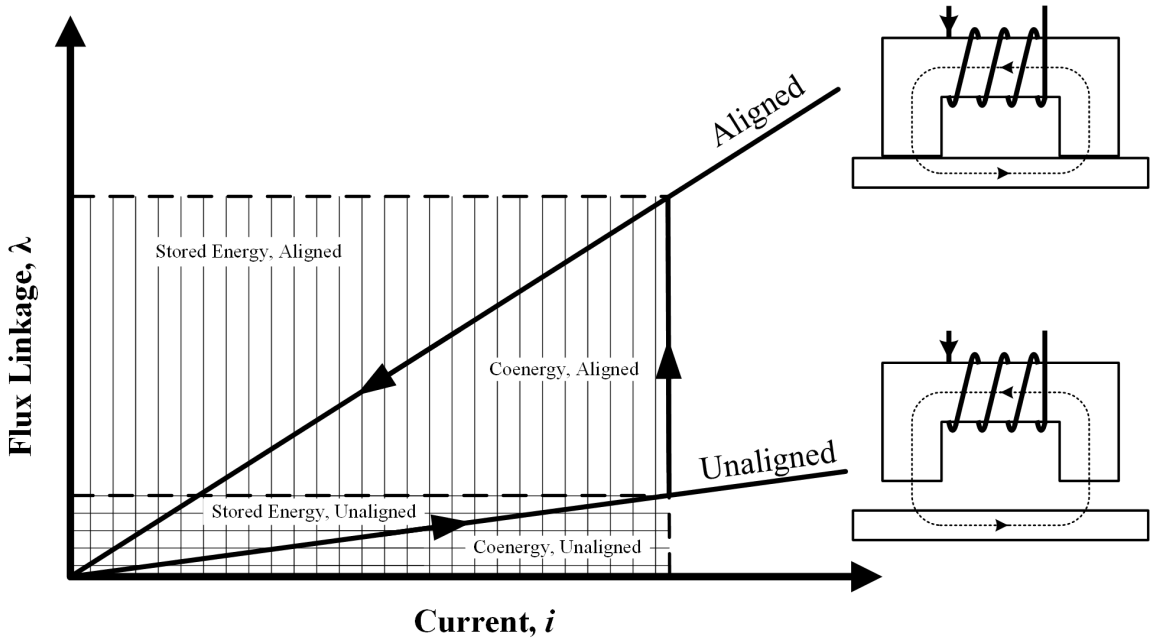

Figure 2.9: $\lambda - i$ diagram for a linear (unsaturated) undergoing a cycle of magnetization and demagnetization

For saturated systems, if the rotor is in the unaligned position and a constant DC current is flowing in the stator winding, the rotor will move to the aligned position, where the trajectory of the $\lambda - i$ diagram takes the form illustrated in Fig. 2.10. The work done in moving the rotor from the unaligned position to the aligned position is given by:

$$\triangle w' = T_{avg} \triangle \theta \tag{2.13}$$

Where $\triangle w'$ is change in co-energy, $\triangle \theta$ is change in angular position and T_{avg} is average developed torque.

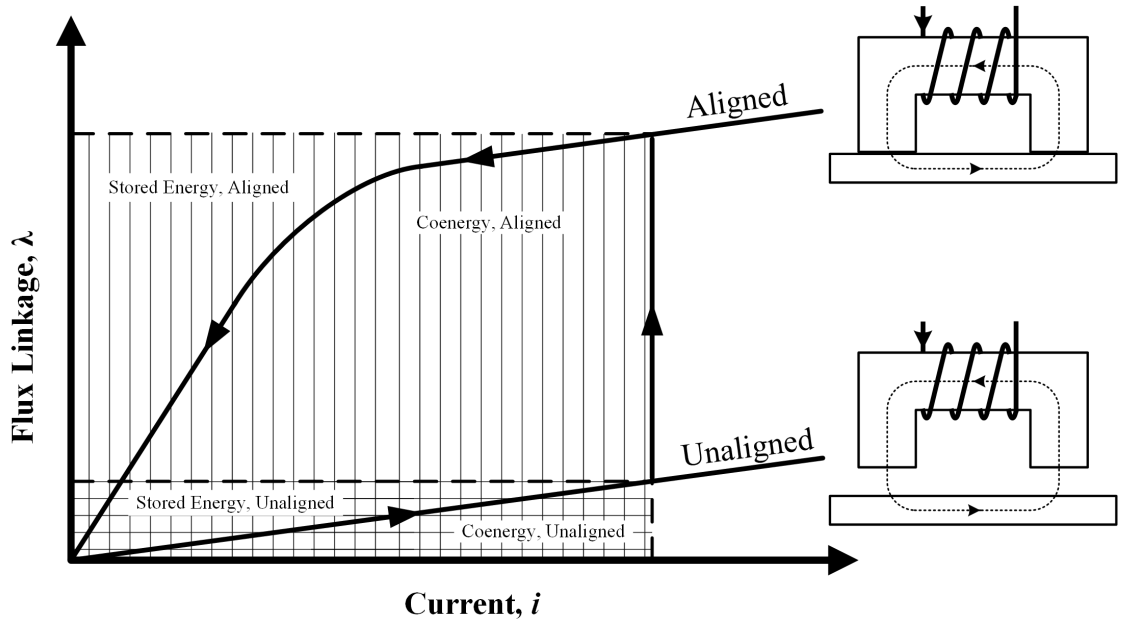

Figure 2.10: Trajectory as coenergy changes between aligned and unaligned position.

2.1.3 Torque Production

Alternatively, multiplication of Equation 2.12 by current yields the machine instantaneous electrical power:

$$Vi = Ri^2 + iL(\theta, i)\frac{di}{dt} + \frac{i^2 dL(\theta, i)}{d\theta}\omega \tag{2.14}$$

The first term on the right-hand side is the winding joule loss. The second term is the system stored electro-magnetic power and the third term is the mechanical input or output power. Hence, given that torque is mechanical power divided by mechanical speed, torque becomes:

$$T = \frac{1}{2}i^2\frac{dL(\theta, i)}{d\theta} \tag{2.15}$$

which is a function of current and change in inductance with position [90]. From Equation 2.15, significant variation between aligned and unaligned inductance is necessary to maximize torque production.

2.2 Loss Mechanisms

Application requirements impact the cost and complexity of any machine design. The electric machines presented in this Chapter range from simple designs for machine tools to advanced designs for power generation systems. Dictating design complexity is largely loss mechanisms within the machine. While traditional SRM design concerns such as torque quality and noise can be improved with various design practices, these improvements often come at the expense of increased losses or cost. In some cases, solutions commonly applied to improve performance of low speed machines are not applicable to high speed machines as the loss or financial trade-off is simply too great. As a result, a brief review of the loss mechanisms in switched reluctance machines will be presented to help identify challenges and proposed solutions for high speed switched reluctance machines and drives.

2.2.1 Soft Magnetic Core Losses

Core losses are used as inputs to thermal analysis; therefore, being able to quantify the core losses is important to the machine design process. Core losses are typically estimated using the Steinmetz equation for sinusoidal currents, or the modified Steinmetz equation for non-sinusoidal currents [6]:

$$P_{loss} = k_h f B^2 + k_c f^2 B^2 + k_e (fB)^{3/2} \tag{2.16}$$

where, f is flux frequency, B is the core peak flux density, k_h, k_c and k_e are the hysteresis, classical eddy current and excess loss coefficients respectively. Hence, the total core loss is the sum of hysteresis, eddy current and residual losses.

Hysteresis loss is associated with magnetization of a core and is the energy lost during the transition of a flux loop, further represented by the area enclosed by a B-H curve, as

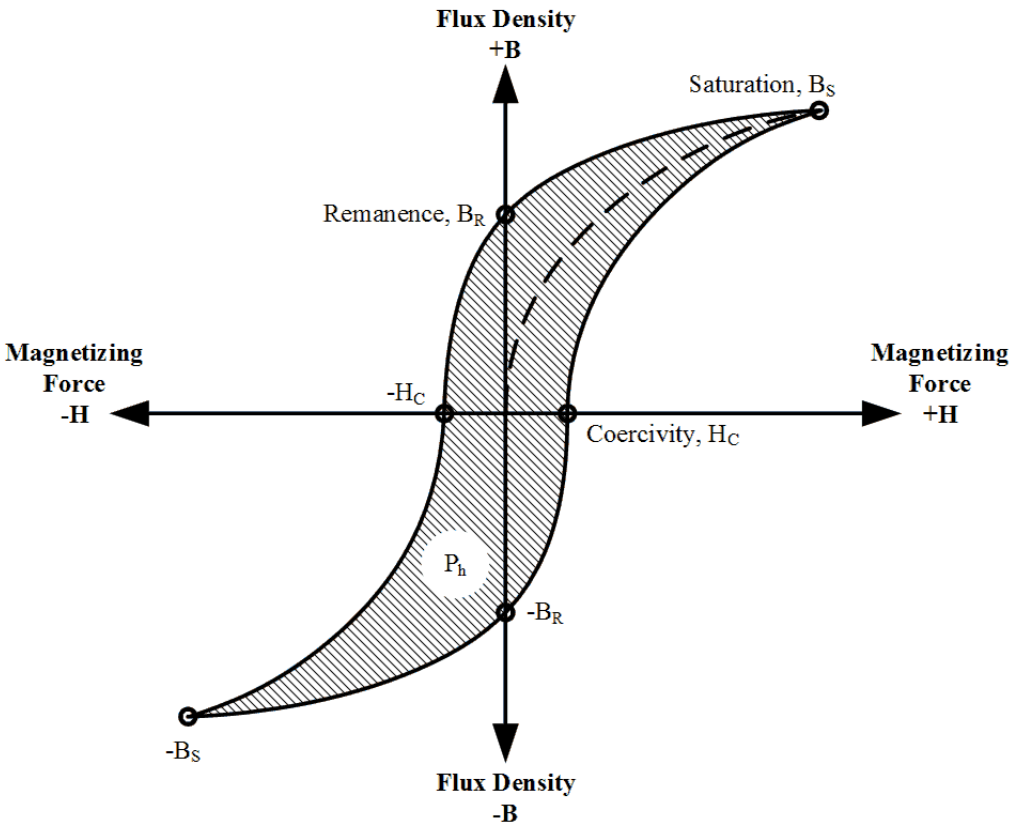

Figure 2.11: Hysteresis loop for ferromagnetic material during magnetization [6].

shown in Fig. 2.11. As frequency increases, hysteresis loss increases proportionally.

Eddy current loss is generated in an electrically conductive material as a result of currents induced from a magnetic field. The currents dissipate energy based on material resistivity. As power and frequency increases, the eddy current effect becomes more significant due to induction and skin effect.

Fig 2.12 shows a magnetic field, B, inducing currents, i, in laminated steel and solid ferromagnetic material. Eddy currents are the reason why electrical machines use laminated steel. Laminating the core reduces the current circulation path; therefore, reducing the losses generated. Tong [6], states that eddy current losses are approximately equivalent to the square of the thickness. Suggesting that a reduction of lamination thickness by one half will result in a eddy current reduction of one fourth.

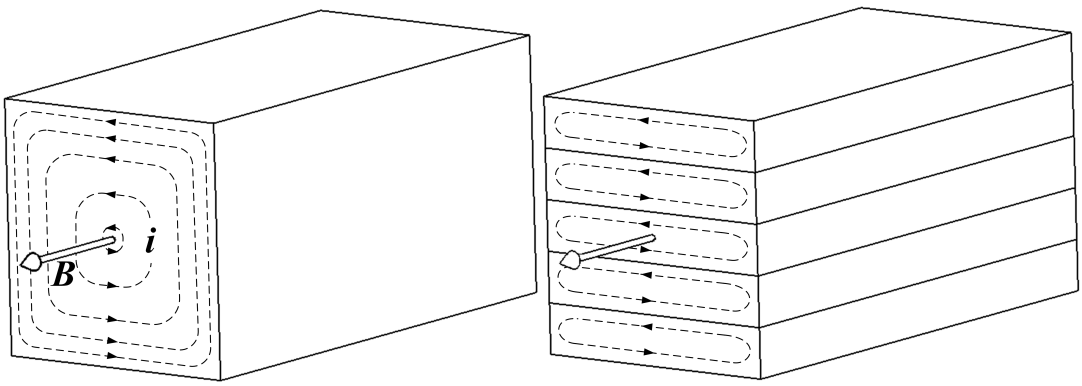

Figure 2.12: Instantaneous eddy currents in (a) solid material (b) laminated material.

Residual loss is any loss not described by hysteresis or eddy current losses. Such effects could arise from manufacturing methods [92–95] or stresses applied during assembly such as interference fits. Designers have to be careful when cutting or stamping the laminations, certain manufacturing processes can locally change material properties resulting in lower saturation flux density and higher losses. A common prototype method which can have significant impact on lamination performance is laser-cut laminations. The intense heat changes the material properties along the edges of the laminations. This is particularly disadvantageous near the airgap where flux densities are highest. Some residual losses can be removed with a post-processing annealing [96].

2.2.2 Machine Winding Losses

Total winding losses are the sum of DC and AC losses [97].

DC resistive loss is the I^2R loss associated with the windings conducting electricity, where I is the root mean square of the conducted current and R is the winding resistance given by:

$$R = \frac{l}{\sigma A} \tag{2.17}$$

where σ is the electrical conductivity of the material.

AC resistive loss is the winding losses produced by eddy currents when the individual strands of a winding are exposed to external magnetic fields. External magnetic fields arise from stray fluxes, fringing flux, or local eddy current effects in the winding. These effects can be significant in high frequency machines.

AC losses are the result of leakage and fringe flux in the stator slots. The leakage and fringe flux creates a bi-directional magnetic field around the windings as shown in Fig. 2.13. This bi-directional magnetic field produces bi-directional current in the windings. Given that resistance is a function of frequency, inducing additional directional currents in the windings subsequently increases the frequency and hence the winding resistance. In high frequency machines, the effects of AC losses can be significant [97].

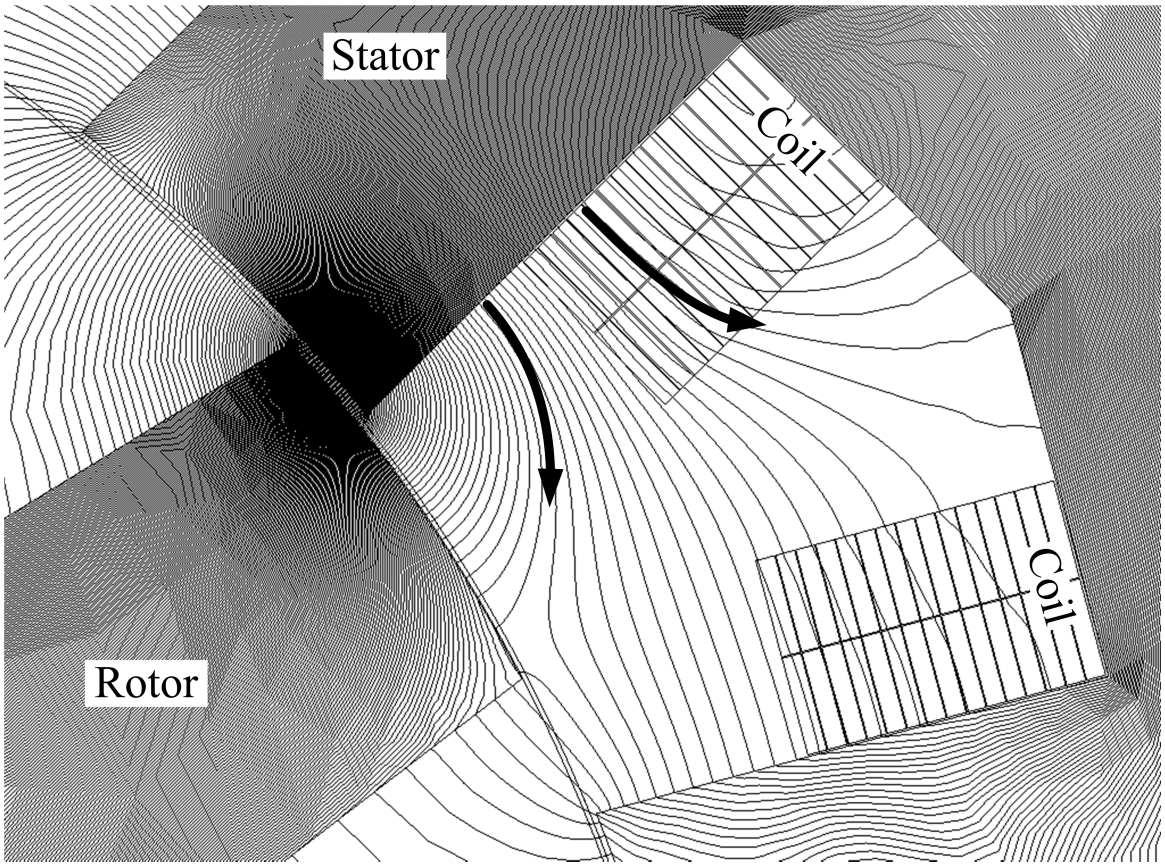

Figure 2.13: Flux line plot around stator and coils.

2.2.3 Machine Mechanical Losses

Windage loss is friction caused by relative motion between motor components and surrounding environment fluid, most commonly, air. Windage in switched reluctance machines is particularly important due to the doubly salient structure of the motor, which increases the drag coefficient over an ideally cylindrical rotor.

Bearing loss is loss associated with the mechanical device supporting the rotor in the housing. In the case of rolling element bearings, bearing loss is caused by friction between the rolling elements and the raceways. Friction between rolling elements and the lubricant itself can also be an issue particularly in high speed machine design. In the case of magnetic bearings, bearing loss is caused by eddy currents and hysteresis In the case of plain/fluid film and gas bearings, friction losses are caused by relative motion between the shaft and supporting fluid. Significant startup and stop friction between shaft and stationary components can occur if external fluid pressure is not present.

2.2.4 Power Electronic Drive System Losses

Beyond passive component loss which is generally small, there are two primary sources of loss in an electrical drive, those being conduction and switching loss in the switching devices.

Conduction loss is I^2R power loss created when current flows between a collector and an emitter of a switching device. In the case of an isolated gate bipolar transistor (IGBT), the collector-emitter resistance is known as $R_{DS(on)}$. Fig. 2.14 shows the relationship between voltage, current, $R_{DS(on)}$ and conduction power loss during a switching cycle.

Switching loss is generally small compared to switching loss. Switching loss is generated when a switching device transitions from on-state to off-state or off-state to on-state.

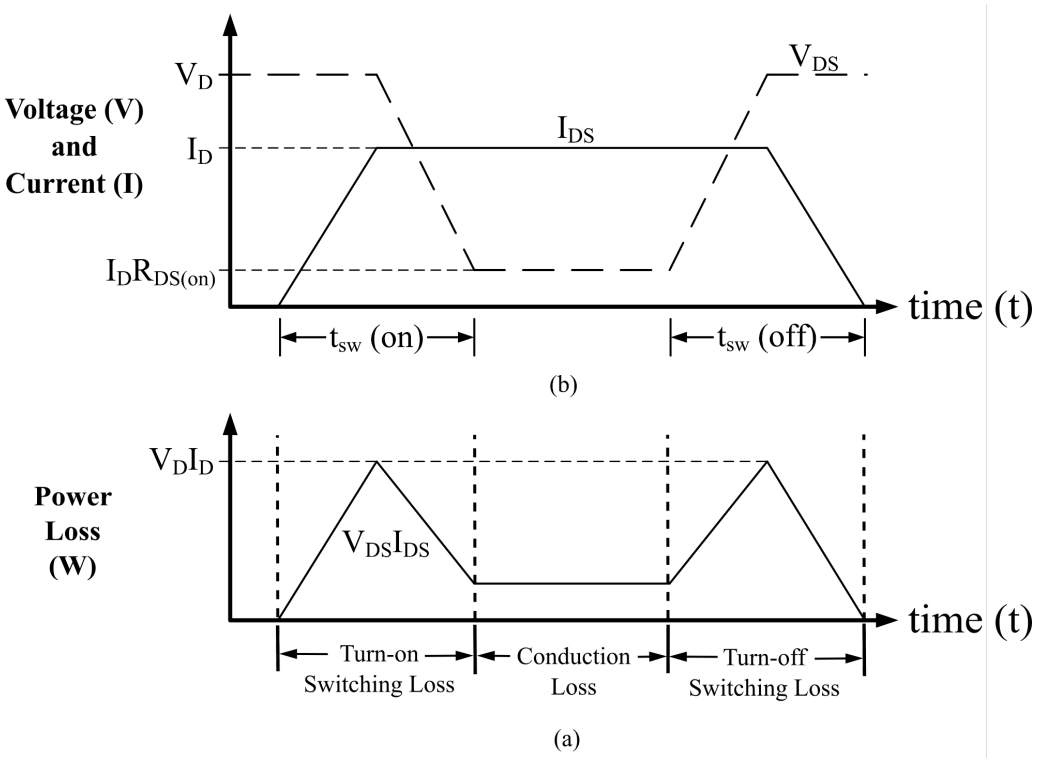

Figure 2.14: General IGBT switching characteristic diagram; (a) current and voltage (b) power loss.

2.3 High Speed Mechanical Design Considerations

High speed machines have significant structural challenges. In this section, solutions to rotor design challenges are presented first, beginning with aerodynamics and progressing to lamination stresses and shaft dynamics. Finally, design considerations relevent to the stator will be discussed.

2.3.1 Rotor

Switched reluctance machines have doubly salient structure. Compared to the aerodynamically ideal cylindrical rotor geometry, the salient structure of reluctance machines contributes to a higher drag coefficient. In addition to saliency, as airgap length approaches zero, the drag coefficient also increases presenting compounding aerodynamic

challenge for the traditionally small airgap machines. Several researchers have attempted to address this problem. In [46, 47] and [60, 61], a cylindrical rotor geometry has been examined which prohibits airflow between teeth without additional rotor components or manufacturing methods. A novel two pole cylindrical geometry composite rotor design is presented in [63] for a 200,000rpm SRM. The design in [44] has cast magnesium between the teeth and then places a carbon fiber band around the rotor for windage loss minimization. This band also serves an additional important function, which is retaining the cast material and reducing the lamination stresses.

Lamination stress must be carefully examined on high speed machines. Electrical steels with around 3.5% silicon generally have 250-460MPa yield strength. Amorphous materials and vanadium cobalt steels can have extremely high strength. Vanadium cobalt steels can have up to 1,200MPa yield strength and 1% elongation as cold rolled [98]. Elongation influences the lamination manufacturing method, for example a brittle material cannot be easily stamped and will require a more expensive manufacturing method such as waterjet, laser or wire electrical discharge. Cobalt steels can be annealed to enhance ductility; however, this influences both yield strength and magnetic properties [98]. Rotor containment features such as carbon fiber or superalloy banding can be difficult to implement in certain circumstances due to the magnetic trade-offs of the increased airgap length. Thus, minimizing the lamination stress is critical for reluctance machines to reach their maximum mechanical performance envelope. As can be seen in Fig. 2.15, shaft-less laminations have significantly lower stresses than a rotor with a through shaft. Shaft-less designs are presented in [63, 80, 81, 99] in effort to minimize lamination stresses. In addition to traditional rotordynamic and centrifugal force analysis, a shaftless high speed motor design requires fatigue analysis of the bolts and laminations, as well as careful attention to alignment of the shafts and assembly balancing [81].

On all rotating equipment, the length of the shaft can not be unboundedly large. At

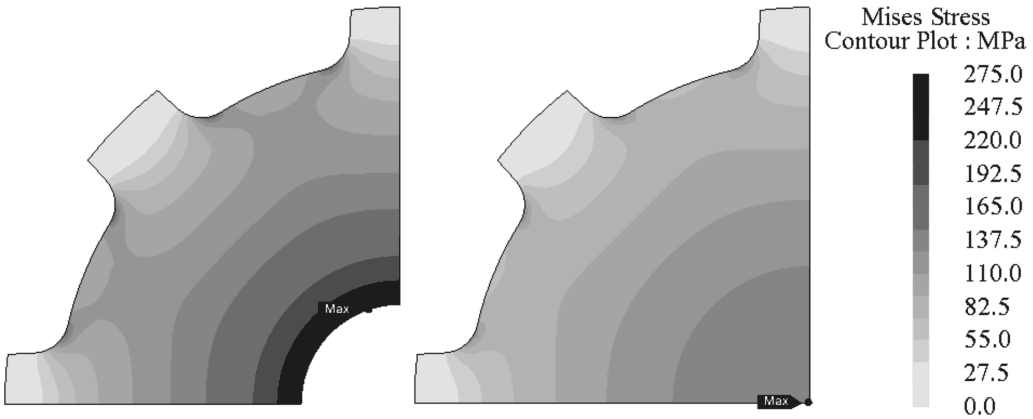

Figure 2.15: Quarter model stress contour for laminations rotating at 20,000rpm (a) with shaft σ_{max}=296MPa (b) without shaft σ_{max}=144MPa

some rotational velocity, rotationally induced vibrations called critical speeds will occur. The longer and narrower the shaft, the lower the velocity at which vibrations will occur. In machines designed and rated for low speed operation, it is possible that the shaft can be designed such that critical speeds can be put above the excitation frequencies experienced by the system. In fixed speed machines, it is possible that the critical speeds be placed in a speed region that is not commonly excited during normal operation. In the case of high speed, variable frequency machines, shifting critical speeds out of the operational frequency range can be difficult. When a machine operates above a critical speed, careful attention needs to be made to ensure that the shaft does not exhibit unstable behavior. Improper design can lead to unusually high shaft deflection, high stresses, and high bearing loads leading to bearing failure or shaft or lamination fatigue failure. Introductions to shaft dynamics and analysis in high speed switched reluctance machines are provided in [68, 84]. Bearing stiffness estimations are presented in [68] in addition to analysis of various bearing types and arrangements. Squeeze film dampers, a damping mechanism, are presented in [84] for additional damping when a rotor must pass through a critical speed. Ferreira and Richter [88], discuss bearing design, critical speeds, and stiffness

analysis of bearings and bearing support structure. A bearing-less 30,000rpm motor is designed and implemented at low speed in [51–54]. In this work, the phases are controlled independently and force balancing algorithms control current to levitate and rotate the rotor without the use of bearings.

2.3.2 Bearings

Many different types of bearings exist which are grouped into three primary brackets according to Tong: journal/contact, non-contact, and rolling element bearings [6].

Journal is the simplest type of bearing. There are no moving parts beyond the rotor. The rotating and stationary components of the bearing are often in physical contact. Journal bearings may or may not require an auxiliary fluid pump depending on the design and application. Fig. 2.16b shows a journal bearing without external fluid pressurization, operating on fluid film created by hydrodynamic pressure. Friction between the two components must be low and cooling may be necessary under large loads. Journal bearings are often used in applications where considerable damping is required [6].

Rolling element bearings, as represented in Fig. 2.16a, comprise the majority of the electric machine market and are characterized by rolling elements between the rotating and stationary parts of the bearing races. These rolling elements create low friction, which is usually lower than journal type bearings. In general, rolling element bearings provide very little damping [6].

Fluid film bearings are a non contact bearing producing low friction between the rotating and stationary surfaces. Fluid film bearings are produced by injecting a high pressure liquid or gas between shaft and bearing surfaces which are precisely machined to the appropriate tolerance. Fluid film bearings are particularly common in pump applications due to their low loss and reliable nature.

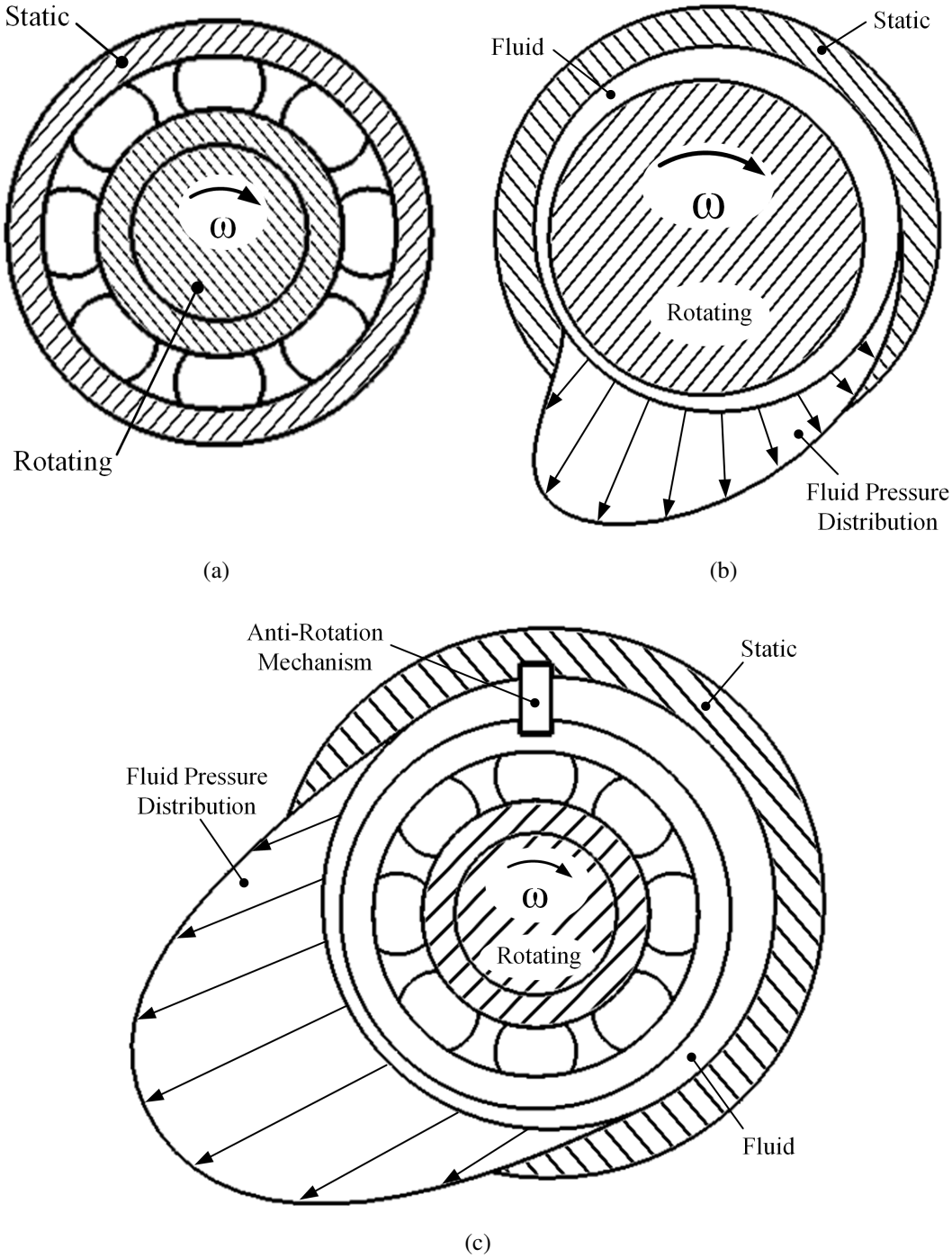

Figure 2.16: Comparison of (a) rolling element bearings, (b) fluid film bearings (c) rolling element bearing with squeeze film damper

Air and magnetic bearings are non-contact solutions. These bearings may or may not need an auxiliary power source [6]. For example, air bearings can be externally pressured, but there is also air-foil bearings, which function on a similar hydrodynamic principle as fluid-film journal bearings.

Many bearings are in essence hybrid bearings, which work on multiple physics principles to achieve particular bearing characteristics. Fig. 2.16c depicts a squeeze film damper, which is effectively a rolling element bearing and a journal bearing, which yields low friction as a result of the rolling elements, but better damping characteristics as seen on a journal type bearing.

Binder et. al presents bearing type for several different machine designs in Fig. 2.17 [7]. From the chart, it is easy to see that rolling element type bearings become progressively less viable as power increases. Instead, journal type and magnetic bearings become more economical. To compare and contrast the different types of bearings, Table 2.1 was compiled with general performance characteristics.

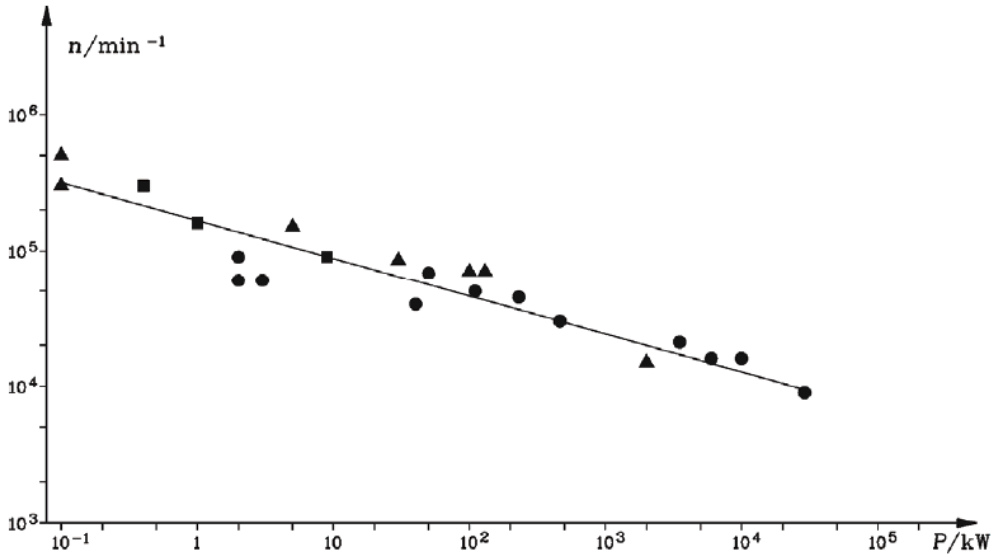

Figure 2.17: Bearing type for a number of machines as aggregated by Binder [7].

Table 2.1: Bearing Characteristic Comparison Chart

	Stiffness	Damping	Reliability	Friction	External Lubrication
Rolling Element	High	Low	Low	Low	No
Journal	Low	High	High	High	Yes
Squeeze Film	Moderate	Moderate	Moderate	Low	Usually Yes

2.3.3 Stator

The majority of machines have straightforward air-cooled designs for the stator. As power increases, more unique designs arise. Cooling channels are integrated into the yoke in [72]. Slot cooling with an epoxy potting is applied in [76]. In addition to slot cooling, [76] and [86] also have oil cooling for the shaft and the jacket. A type of slot-cooling and yoke-cooling channels are integrated into the stator backiron in [68] to better target cooling of the windings and tip of the teeth without the use of a cooling jacket. The stator laminations have fins which are left exposed to the air for convective cooling of this turbocharger.

In high-speed high-power applications, high frequency and high field strength creates high frequency slot leakage and fringing flux, which can result in significant AC currents and non-uniform current density distribution in the windings. In [88], windings are made from copper tubes and oil coolant is passed in the windings. Thermal analysis including the effect of AC currents on the windings is also investigated in this work.

Airgap selection is crucial for switched reluctance machines as it has direct impact on torque production. In general, the airgap size is dictated by the available manufacturing and assembly tolerances. References [67, 68] design machines with over 100,000rpm capabilities and have 0.2mm and 0.15mm airgaps respectively. A 0.35mm air gap is chosen for the 1.7kW 50,000rpm turbocharger in [66]. The 45kW 32,000rpm IESG design in [79] investigates a 0.64mm gap.

2.4 Materials and Magnetic Design

In Table 1.2, pole configuration, lamination material, DC link voltage and rated-speed efficiency is documented for a number of SR machines reported in the literature. The general trend in high speed machines is to select a low pole count design to minimize core losses; however, this is not without consequence. Several non-generator machine designs employ two pole rotors, by way of example, a stepped rotor is presented in [58] which mitigates self-starting challenges. Torque quality for high speed machines is also generally poor and even worse with low pole count designs, as low inductance and single pulse operation is usually required to reach high speed and will be further explained in Section 2.5. Examples of finite element generated torque profiles are shown in [44, 80]. Where reported torque ripple, i.e. peak-peak torque, can easily be 100% of the average torque.

MacMinn et al. [76, 77] details a 105VDC, 32kW, 48,000rpm starter-generator for a gas turbine. The machine and drive are later redesigned for 270VDC, MIL compliancy in [75]. The machine motors up to 26,000rpm and generates beyond that speed. The author quotes 93% generating efficiency, 89% high speed motoring efficiency and 46% low speed motoring efficiency. Radun [82], designs and tests a 90kW, 25,000rpm motor and drive for a gas turbine fuel pump. The motor has rotor and stator oil cooling in addition to fuel cooled windings. The complete 6/4 motor geometry is presented in [83] to validate analytical design calculations such as unaligned inductance, static torque, flux-linkage, rate of change of flux-linkage and maximum rotor torque density. References [43, 86–89] outline a 22,200rpm, 250kW integrated starter-generator for gas turbine application. The machine is a three-phase two-channel 12/8 topology. The authors use the term “two-channel” to describe that the machine and drive can be physically thought of as a six-phase machine which is powered by two electrically isolated three-phase drives and two electrically isolated power supplies that connect to the motor in

parallel. This high speed, high torque machine coupled with the high permeability of vanadium cobalt laminations results in a 124lb, 19in total length by 10.5in diameter motor (equating to 56.3kg, 482.6mm length and 266.7mm diameter). This 250kW machine has a continuous power density of 4.5kW/kg, and at the time of writing, is the most powerful switched reluctance motor operating above 20,000rpm in published literature. However, the machine uses exotic magnetic materials, mechanical implementation, and cooling. Thus, the challenge for this thesis is to explore the limits of more conventional materials and practices that would make SRM a machine technology suitable for the high volume automotive market sector.

Two 30,000rpm, one 60,000rpm and one 100,000rpm machines are compared in a design study in [84] as potential candidates for auxiliary power units in large industrial vehicles and armoured vehicles. For the 30,000rpm machines, M-15 electrical steel is analyzed. For the 60,000 and 100,000rpm machines, structural steels AISI 4130 and 4340 are selected for magnetic analysis. The reasons for selecting AISI 4130 and 4340 for the 60,000 and 100,000rpm motors are not entirely clear. Material strength is suggested as the possible motive; however, a 300kW, 100,000rpm machine would almost certainly be considered a high-performance application. The low saturation characteristics of AISI 4130 and 4340 will result in poor energy conversion in an SR topology. The authors ultimately conclude that the 100,000rpm, 300kW machine has low feasibility due to the low efficiency which was estimated to be 40.0% . A high performance application may justify the use of an iron vanadium cobalt such as Hiperco 50A, but again this would likely be cost prohibitive for mass market automotive applications.

A brief analysis was conducted to examine the feasibility of a 300kW, 100,000rpm machine utilizing Hiperco 50A. Hiperco 50A has 1,200MPa yield strength and 2.4 Tesla saturation flux density at a prescribed heat treatment. The high material yield strength allows for a large diameter rotor, and the high saturation flux density allows for greatest

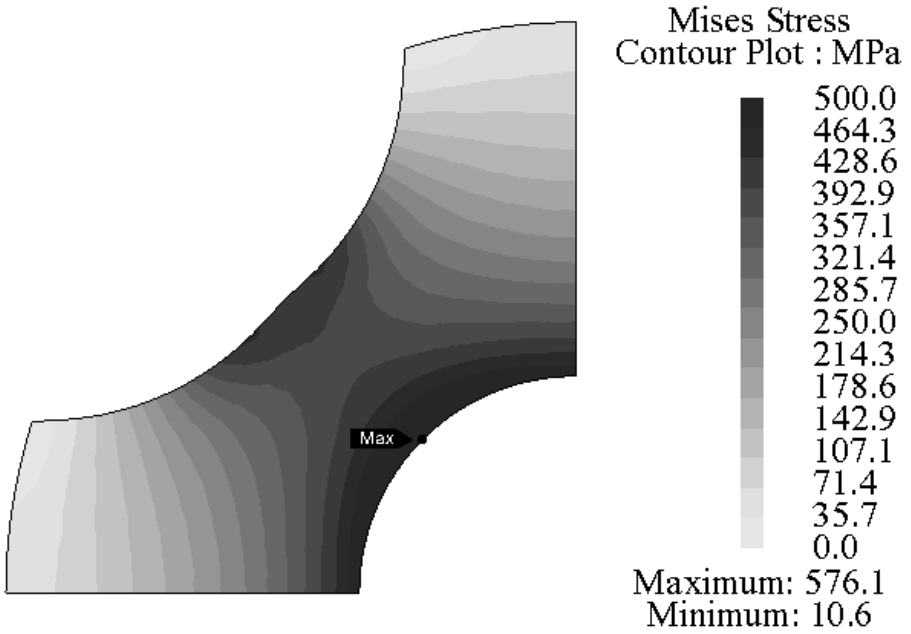

Figure 2.18: Quarter model lamination stress contour of a four pole rotor rotating at 100,000rpm

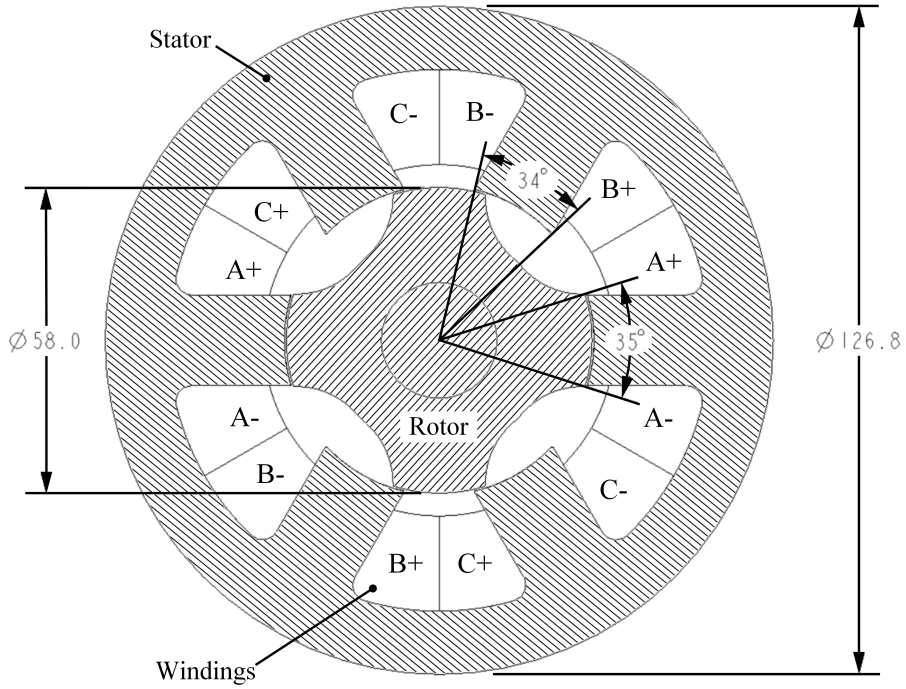

Figure 2.19: Magnetic design of a 100,000rpm, 300kW 6/4 SRM.

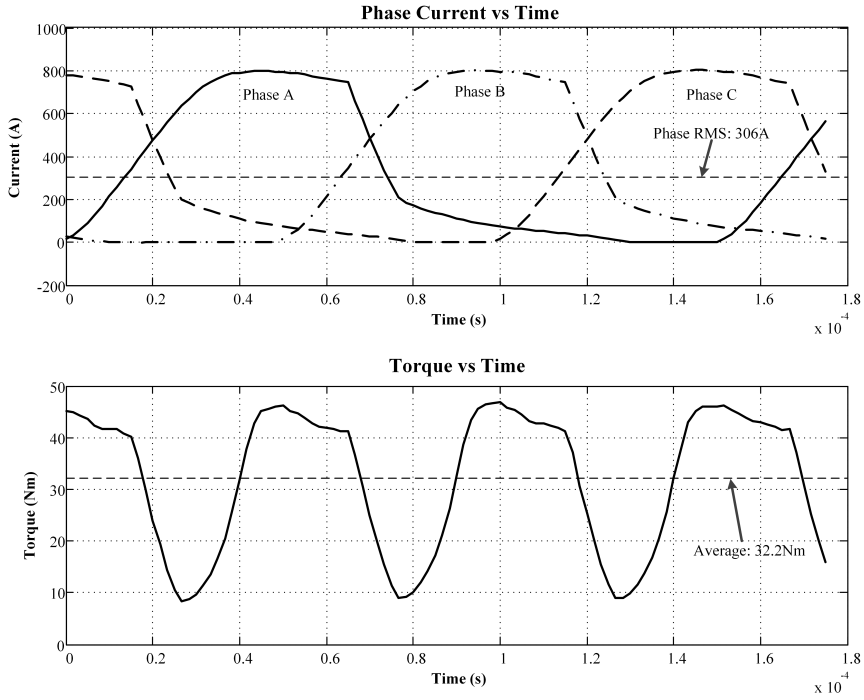

Figure 2.20: Torque and current profiles at 100,000rpm

torque for a given rotor volume and electrical loading, as previously described in Section 2.4. A series of stress analysis varying rotor diameter suggest a maximum permissible rotor outer diameter of 58mm while maintaining a safety factor of two, a typical solution results being shown in Fig. 2.18.

The complete machine magnetic geometry is shown in Fig. 2.19, electromagnetic transient analysis of which shows that a geometry with a 175mm stack length could produce 300kW at 100,000 rpm with appropriate cooling, current and torque results being shown in Fig. 2.20. The mass of the magnetic material reduced to 15kg, a 30% reduction from the proposed design. 12AWG, 6 strands, 7 turns, parallel connected windings, and 60% fill factor were considered in this analysis. Phase current carrying capacity was 370A. The conduction angles shown in Figure 2.20 are -60 to 100 electrical degrees. The rated-speed efficiency is estimated to improve from 40% to the order of 90% through the use of 0.1mm thickness Hiperco 50A.

2.5 Drive Considerations

Power electronics and the associated drive and control are crucial to the operation of switched reluctance machines, the design of which becomes particularly challenging at high speeds and high powers. The characteristics and availability of the switching device must be considered to meet machine performance requirements at both high and low speeds. This section aims to describe how various machines were able to achieve a wide speed and torque range. Here, drive, power electronic switch and control topologies will be discussed for various high speed machines.

2.5.1 Fundamentals of the Asymmetric Bridge Converter

The asymmetric bridge is one of the most common converter topologies for switched reluctance machines, a schematic of which is shown in Fig. 2.21 for a three-phase machine.

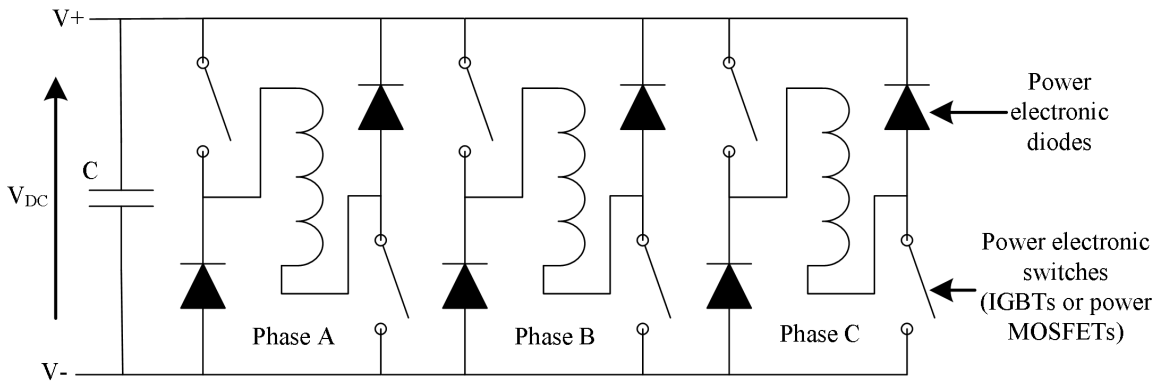

Figure 2.21: Schematic of a three phase asymmetric bridge converter for SRMs.

Fig. 2.22 shows a typical phase current flow in the SRM and drive electronics during one stroke of the SRM. Referring to Fig. 2.22, the drive current flow has three modes, (a) power mode, (b) reverse recovery mode and (c) idle mode.

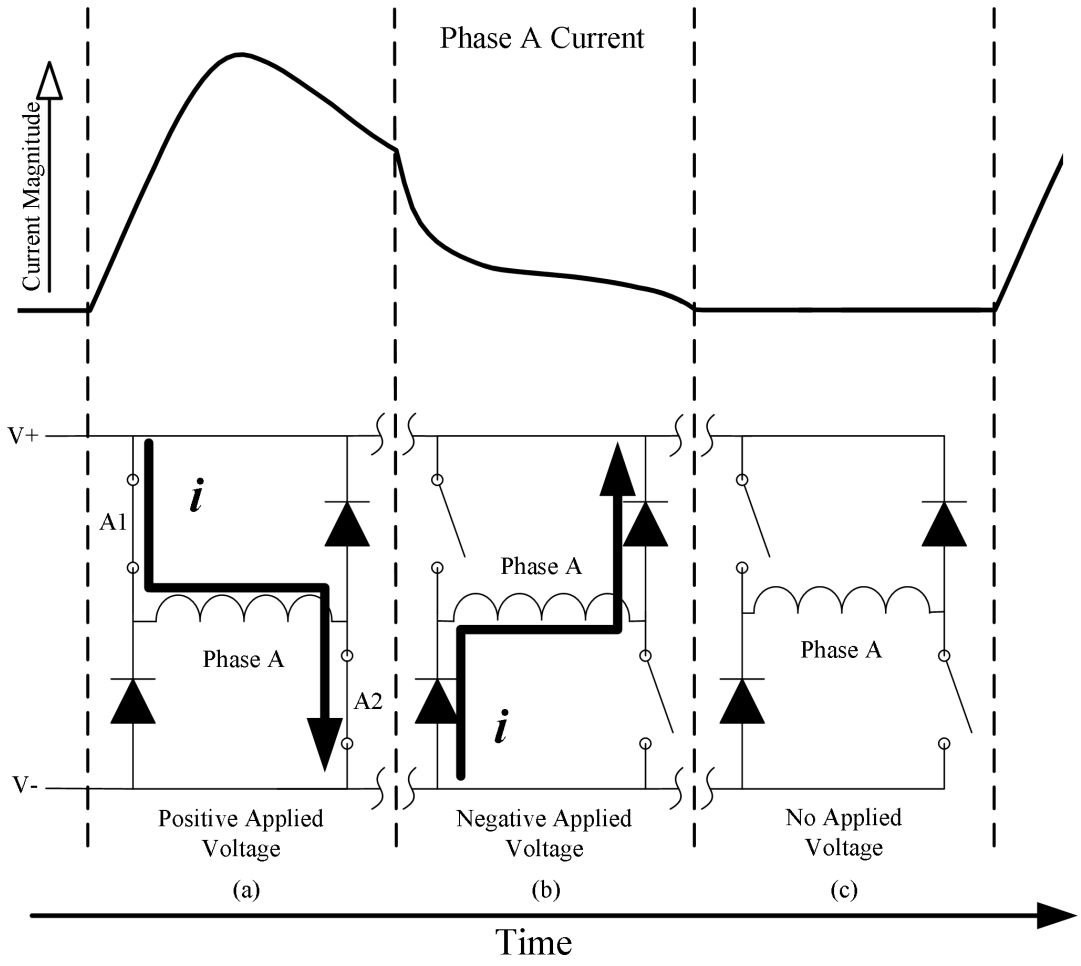

Figure 2.22: Shows machine phase current flow during one stroke of a SRM.

2.5.2 Current Control and Phase Commutation

Phases are commutated according to electrical position which is defined in Fig. 2.23. Electrical period is related to mechanical revolution angle from equation 2.18

$$\theta_m = \frac{360}{N_r} \tag{2.18}$$

$0°/360°$ corresponds to the unaligned position. $180°$ electrical corresponds to the aligned position. Once the motor and controller are characterized in terms of electrical angle, two modes: hysteresis and single pulse are used to control phase current.

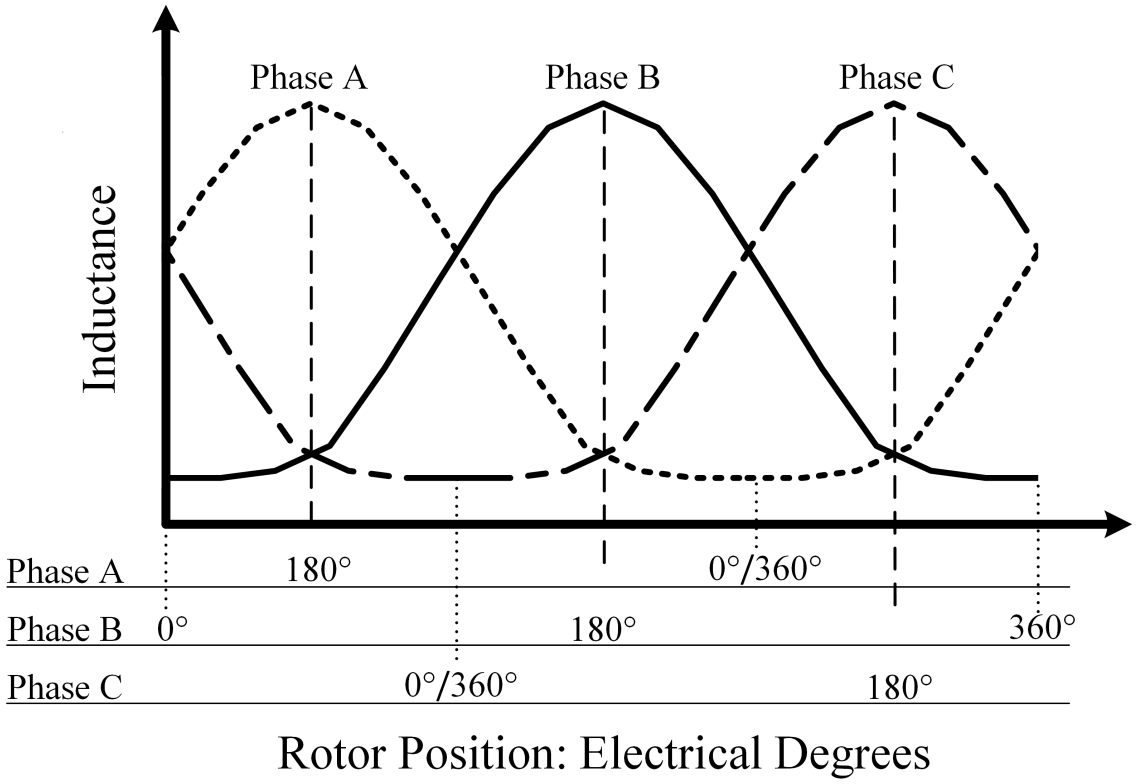

Figure 2.23: Electrical position for each phase of a three-phase inductance profile.

Hysteresis control is used to control current below the base speed as defined in Fig. 2.24. Current sensors are necessary to measure current which is then fed back into the digital signal processor (DSP) or microcontroller. A maximum and minimum threshold is specified and the inverter switches are turned on or off depending on the exceeded threshold. Hysteresis control can be further broken into two additional modes of control: dual or single switch control.

Dual switching is where the upper and lower phase switches turn on and off simultaneously, A1 and A2 in Fig. 2.22a. Dual switching reverses winding polarity resulting in reduction of current and transfer of the winding stored energy to other phases or back to the DC power supply storage capacitor, C in Fig. 2.21.

Single switching is another type of hysteresis control where one switch is left in the on-

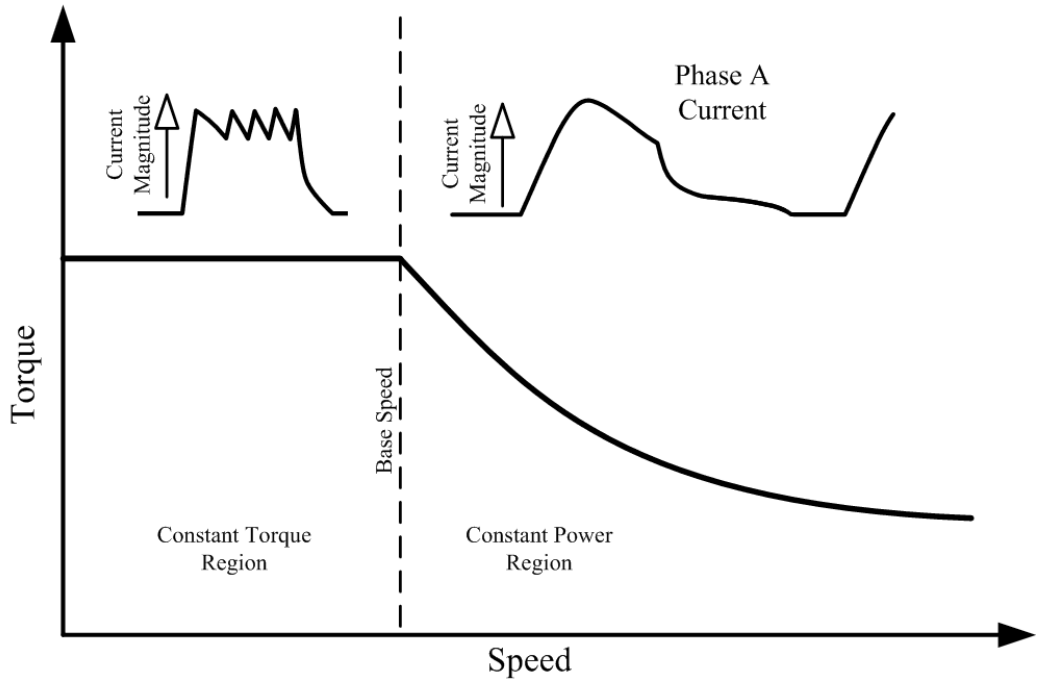

Figure 2.24: A general speed-torque envelope showing hysteresis and single pulse zones.

state and the other switch is modulated. Single switching brings the voltage across a phase to zero, resulting in a lower rate of change of current and lower loss of winding energy in the winding and diode resistance when compared with dual switching. Single switching is sometimes used when reduced switching frequency is desired [100].

As mentioned, hysteresis or pulse-width modulation (PWM) of the asymmetric bridge converter power devices is used to control machine current at zero speed to near base speed. At base speed, the machine voltage drops and effective back-EMF are close to the DC voltage supply (VDC) of the power converter. To achieve speeds above the base speed, the power converter can be operated in single pulse mode, as shown in Fig. 2.24. In this speed region, the main power electronic devices are turned on and off once per stroke. The resulting current waveform is defined by the commutation angles and the rate of change of flux-linkage. As the rate of change of flux-linkage grows beyond the DC link voltage, current stops growing and begins to decline toward zero, as shown in Fig. 2.24 [100].

2.5.3 Asymmetric Bridge Converter Layout and Construction

In industrial applications, power quality, reliability, and system mass become important in both motoring and generating modes. A number of SRM drives have been documented which address these issues. In Table 2.2, details of selected drives are listed for comparison.

In a fuel pump application, Radun [82], investigates a high power density fuel cooled 90kW, 25,000rpm motor drive. The drive topology is mostly discussed in this work; however, some basic machine information is provided for complete system realization. The author compares size, thermal rating, voltage and current capacity for the capacitor chemistries, multilayer ceramic, foil and solid tantalum, aluminum, and polycarbonate film capacitors for a defined ripple current. Ultimately, the multilayer ceramic capacitors were chosen to meet the application power density and performance requirements. The author also investigates MOSFETs, IGBTs, and MOS controlled thyristor switches in this paper. DC-link capacitor sizing, electrical noise susceptibility, and generator stability for high speed, high torque machines is discussed in [101]. Design of a 30kW oil cooled drive for a 48,000rpm, 6/4 IESG motor is presented in [75]. Dual 600V, 300A IGBTs comprise the switches and multilayer ceramic capacitors make up the link. Authors present considerable discussion on military standard compliancy and application environment details. In [71], a 30kW forced-air cooled drive for a 50,000rpm, 6/4 IESG is presented. 600V, 600A IGBTs were selected as the switch of choice. MOS controlled thyristor and IGBT switch topologies are again compared on a 125kW drive in [87]. Dual and single switching is discussed in detail in this paper. References [102] and [86] outline the design and implementation of the fuel cooled MOS controlled thyristor drive for the 250kW integrated starter-generator for gas turbine application. This machine is a 12/8 dual-channel three-phase motor. Two paralleled three-phase motor drives each supply 125kW of power to the machine. The EMI filter for this drive is described in [103]. In

addition to enhancing motor fault tolerance, there are a number of design advantages to the dual-channel motor dual-drive topology. As motor power increases, a general trend is to parallel switching devices, as seen in [82], to increase the current output rating as well as utilize switching devices with higher frequency switching capabilities.

The majority of drives in the listed projects use the asymmetric bridge as the drive topology of choice; however, a split AC converter is used in [59] and a four level multiconverter is researched in [55, 104]. The multilevel converter is particularly interesting in the case of high speed machines, because obtaining acceptable torque quality and efficiency over a wide speed range is a challenging design task. With the multilevel converter, lower-power switches can be selected, which can result in improved switching characteristics. Additionally, because the source voltage is controlled, the required switching frequencies may be lower due to lower rate of change of current then when compared with a standard asymmetric bridge. Enhanced switching frequencies, coupled with lower switching requirements will improve torque quality, but will likely also reduce machine core losses due to the reduced rate of change of current and subsequently the reduced rate of change of magnetic field.

In high-speed, high-power machines, low machine phase inductance can result in hysteresis bands which are hundreds of amps. These large hysteresis bands are necessary to maintain acceptable switching frequencies in the power electronic switches [100]. In these applications, even a small improvement in switching frequency, or a small reduction in rate of change of current can have significant impact on machine performance. The authors of [66] indicate a buck-boost converter on the drive power supply would be of interest in their application. Variable voltage power supplies are a promising method of improving performance of switched reluctance machines, but more thorough research is needed to identify the benefits and challenges of variable voltage power converters for switched reluctance machines.

Table 2.2: Selected drive listing by order of power output

Rated Power (kW)	**Switch Voltage (VDC)**	**Switch Current (A)**	**Number Parallel Switches**	**Electrical Frequency (Hz)**	**Device Type**	**Inverter Topology**	**Cooling**	**Position Sensor**	**Motor Pole Count**	**Motor Winding Config**	**Ref.**
0.63	-	-	-	1333	-	Multilevel	-	Sensorless	4/2	-	[55–58]
1.0				1600		Split AC					[59]
2.0				10000		Asymmetric			6/4		[67]
5.0	600	300	1	6666	IGBT			Hall Effect		2-Series	[68]
30	600	600	1	3333	IGBT		Forced Air	Resolver			[69–74]
32	200	324	3	3100	MOSFET		Liquid				[76, 77]
32	600	300	2	3100	IGBT		Liquid/Oil				[75]
90	500	100	4	1666	IGBT		Liquid/Fuel				[82]
125*	350	500	2	2960	MCT			Sensorless	12/8	4-Parallel	[43, 86–89]

*Dual Channel
-Undefined

2.5.4 Control & Position Determination

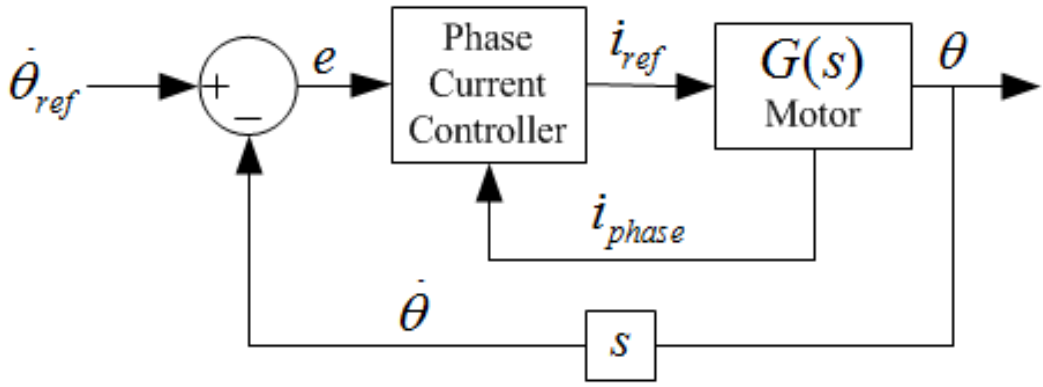

Figure 2.25: Control diagram of a speed controlled motor with position sensor.

Figure 2.25 depicts a general speed control loop for a switched reluctance machine. From the diagram, SRMs need some method of rotor position information in order to apply the gate signals at the proper instant. In high reliability systems, position sensors create additional failure modes which must be considered in the design process. For ultra high speed machines, accurate position sensors simply may not exist and position estimation is required. In [68], Hall effect sensors were used to a degree of success; however, most projects listed in Table 2.2 used high speed resolvers on their machines.

Both encoders and resolvers are comprised of a rotor and stator; however, the operation principle differs. Encoders use an optical sensor which reads markings on the rotor. The markings correspond to a specific position on the rotor. The optical sensor digitizes rotor markings to be interpreted by the controller. Resolvers operate on the principle of magnetic reluctance, and require external circuitry or software to process the output data to usable position information.

Encoders employ optical type sensors and hence have to be sealed for protection against external contaminates. This sealing restricts the operating conditions to lower speed.

Resolvers function on magnetic principles and are largely unaffected by moderate

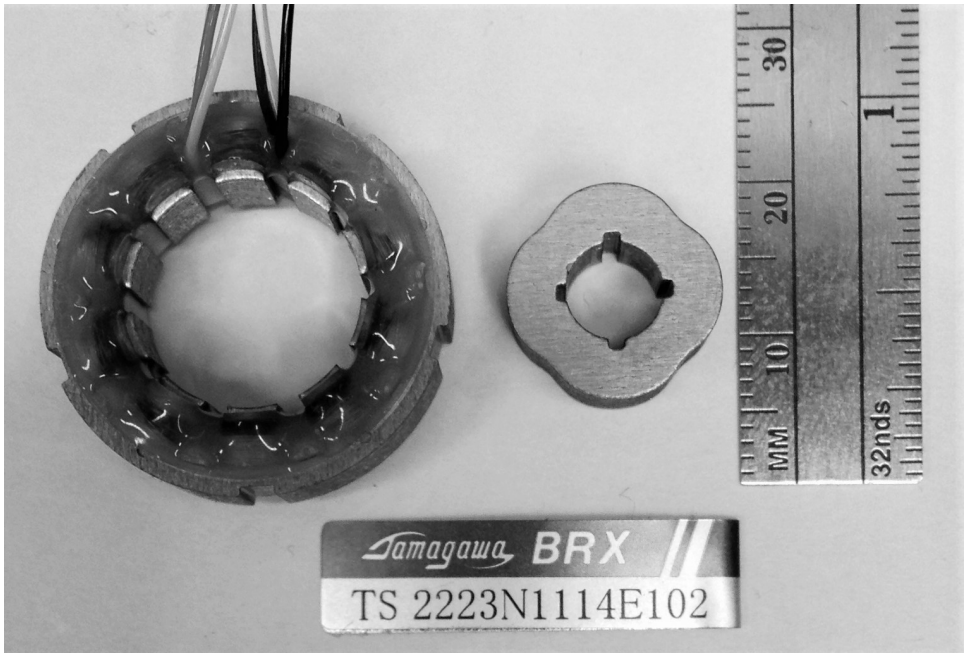

Figure 2.26: Tamagawa Seiki S10 four-pole resolver.

levels of contaminates assuming contaminates are nonmagnetic and cause no electrical interference or corrosion. Resolvers can therefore be unsealed devices which allows their operating speed to be much higher. An example of four pole resolver rated for up to 30,000rpm from Tamagawa Seiki is shown in Fig. 2.26 [105].

2.5.4.1 Sensorless Position Determination

While resolvers are a good solution for position measurement, they remain an added expense to the motor-drive system and additionally, a possible source of failure. Fig. 2.27 depicts a general sensorless speed loop controller which uses voltage, current and a transfer function of the motor to estimate rotor position. Researchers have investigated sensorless methods of determining position in high speed environment.

Lyons et al presents three methods for estimating rotor position which were implemented on a 120Hp (89.5kW) 25,000rpm 270VDC SRM. The first method is a single phase excitation method which uses phase current and voltage to compare estimated

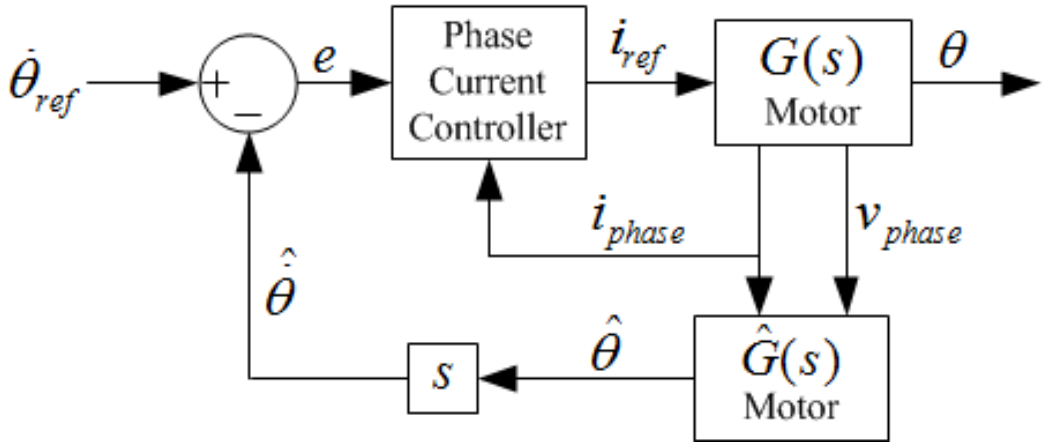

Figure 2.27: Control diagram of a speed controlled motor without a position sensor.

flux linkage with a reference. The second method is a multiphase excitation method which includes mutual coupling effects in flux linkage estimation, then compares the flux linkage estimate to a reference. The final method uses a lumped parameter model which is able to account for magnetic effects including leakage, multi-phase saturation, and mutual coupling.

Jones et al integrates phase voltage and current to get flux linkage in [106]. Kirchoff laws are then used to estimate phase voltage from a single DC Link voltage sensor. This position estimation method is implemented on a 30kW 48,000rpm starter generator motor. The authors show DC Link voltage is able to conform with MIL power quality requirements when loads are added and removed, nor did significant efficiency variation exist between sensorless position estimation and the use of a physical resolver.

2.5.4.2 Control

In most of the machines investigated, the control algorithms were PID based speed-loop controllers in combination with standard hysteresis and single pulse current control methods. Only in [57] was a torque sharing function (TSF) developed for a high speed machine. In this work, the TSF was designed to compensate for the negative phase torque produced at high speeds. Considering the high torque ripple associated with high speed machines at both high and low speeds, torque sharing functions appear to be a promising method of enhancing torque quality in switched reluctance machines.

2.6 Conclusions

Machines which operate above 20,000rpm have been investigated to review the state-of-the-art for high speed switched reluctance machines. The vast majority of machines have a minimal pole count to minimize core losses. A wide range of core materials have been employed from structural type steels, to standard high volume motor grade steels, to ferrite and vanadium cobalt.

Researchers have shown that control over a wide speed and power range is achievable with a standard asymmetric bridge converter using both sensorless and sensor-ed rotor position determination methods. While many researchers have developed successful SRMs, few have validated performance at the rated speed and torque, likely a result of machine development challenges as well as economical barriers inherent to high speed testing apparatus.

Low cost, fault tolerance, and reliability are often cited as reasons for switched reluctance machine implementation. Taking advantage of high reliability and high speed operation is one approach to increase the specific power of machines. High speed operation may also enable high specific power at a reasonable price point, which may increase attractiveness of SRM in mobile applications.

Chapter 3

Rotor-Centric Design Methodology for Determination of Switched Reluctance Machine Power Limit

3.1 Machine Design Methodology

Design methods describe the engineering process taken to transition from specification requirements to final product. Once the specification requirements are known, electric machine design typically begins with analytical sizing equations that are based on geometry, electric and magnetic load estimations, an example of which for SR machines is the work of Krishnan [90]. Once the machine has been sized, traditional practice is to conduct electro-magnetic finite element analysis to perform a more detailed calculation of speed, torque and quantify losses for input to thermal analysis.

Traditional design practice has proven sufficient for many applications; however, they fall short when analyzing machines with aggressive structural loadings. Electro-magnetic evaluation is of little value if the rotor cannot structurally accommodate the rated speed

and load, as with the design example presented in Fig. 1.1(b). Not only will the machine mechanically fail, but significant time will be spent magnetically analyzing a structurally infeasible motor. To prevent this situation, a novel design methodology is proposed in this thesis as illustrated in Fig. 3.1. The focus of this Chapter is the definition of the iterative sequence of structural analyses outlined by the dashed box in Fig. 3.1. At the core of the methodology, a maximum rotor volume is characterized by centrifugal force and rotordynamic analysis after preliminary sizing, yet prior to electro-magnetic analysis.

The rationale for the design flow comes from Eq. 1.1, the general torque equation for electric machines, where it can be seen that rotor volume directly influences developed torque, and rotor diameter is a larger contributer to torque production than machine active axial length. From a simple torque production perspective, maximizing rotor diameter should logically occur prior to analyzing length.

The structurally focused procedure has several benefits:

1. Rotor mechanical integrity is guaranteed early in the design process; particularly beneficial when evaluating machines of an unfamiliar or novel topology.

2. Guaranteed mechanical robustness eliminates design variables, reducing design iterations and engineering time.

3. Rotor diameter is prioritized over length, resulting in pancake style geometry, thought to have large specific density.

4. Early structural evaluation encourages machine optimization on a structural, magnetic, thermal and cost basis.

As seen in Fig. 1.1c, once the rotor structural capability is defined, magnetics can be optimized to fully utilize the structural envelope. Designers then have flexibility to select cooling systems and core material ideally suited to specification requirements.

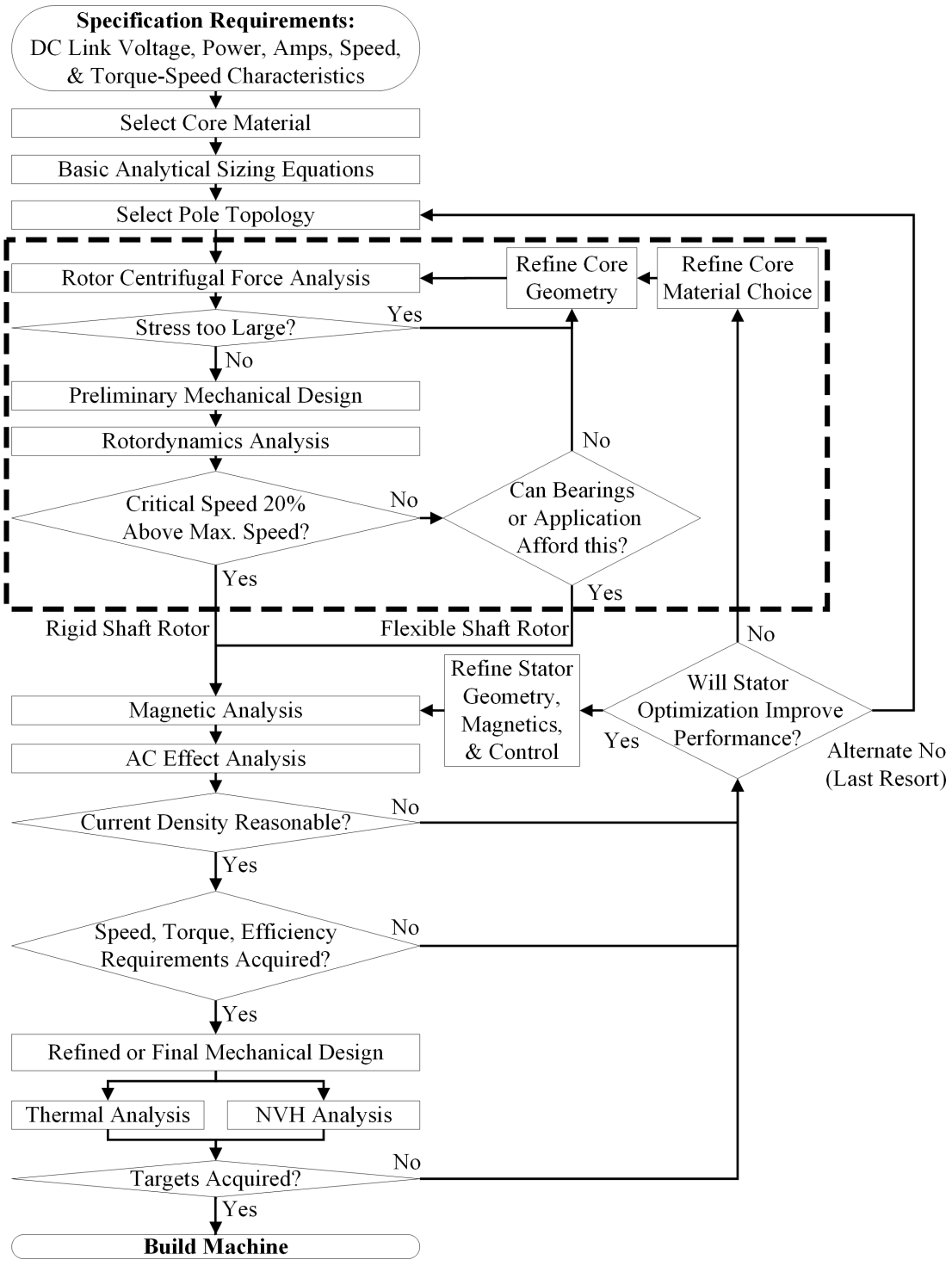

Figure 3.1: Proposed design flow for SRMs with high surface speed. The boxed region identifies the mechanical design procedure described in this chapter.

3.2 Specification Requirements

All machine designs begin with specification requirements. Here, a switched reluctance machine is considered for an automotive traction application.

Lacking rotor excitation, SRMs are generally considered to have lower specific density than permanent magnet or induction machines. This deficiency is traded for extreme reliability, low manufacturing cost and fault tolerance. To improve the specific density of the machine, an important parameter for vehicular design, the approach was taken to pursue a theoretical application where other machine topologies may struggle to perform, or would otherwise be cost prohibitive.

From Eqn. 2.15, increasing rotational velocity enhances specific density. As a result, a 22,000rpm speed rating was chosen for a 150kW traction drive for consideration in a hypothetical application such as a light utility vehicle or a small bus.

To maintain some adherence with industry machine design practices, Class H, 180°C winding temperature was desired for being readily available but also on the high end of thermal classes. Laminations were desired to have low silicon content with thickness between 0.18mm and 0.35mm. Machine mass and efficiency targets were selected based on Department of Energy projections for 1.4kW/Kg and 94% efficiency for 2020. [107]. Since this machine was considered for an ideal new vehicle; no volumetric constraints were applied beyond practical limits.

Torque ripple and noise are known challenges for switched reluctance machines and were not considered as stringent design points for this investigation. Torque ripple and noise are highly dependent not only on machine design, but also drive and control design.

For torque ripple, it was assumed that:

1. the machine transmission would be designed in conjunction with the machine and would be able to accommodate severe torque ripple.

2. the drive and control design would have considerably more influence on torque ripple than the machine itself

Instead, it was elected to assess noise and torque ripple in the theoretical environment, since that information is not known to be well established in published literature.

The complete listing of specifications is found in Table 3.1.

Table 3.1: Specification List

Specification	**Target**	**Unit**
Maximum Rated Speed	22,000	rpm
Maximum Continuous Output Power	150	kW
Maximum Overload Output Power	undefined	kW
Base Speed	undefined	rpm
Minimum Stress Safety Factor	2	n/a
Minimum Critical Speed	1.2*maximum rated speed	rpm
Efficiency	94	%
Specific Power	1.4	kW/kg
Machine Mass	107	kg
Diameter Constraint	None	mm
Length Constraint	None	mm
Voltage	600	VDC
Peak Allowable Phase Current	480	A
Anticipated IGBT switching frequency	5000	Hz
Cooling	Water/Glycol	n/a
Wire Insulation	Class H	n/a
Lamination Material	non-oriented low silicon iron	n/a
Lamination Thickness	between 0.18 and 0.35	mm
Noise	undefined	n/a
Torque Ripple	undefined	n/a

3.3 Maximizing Rotor Diameter

With the machine specifications defined, determining maximum rotor volume begins by maximizing rotor diameter. Pole arc angles, pole number, pole height, taper, and backiron thickness were initially estimated according to Krishnan's preliminary design theory. Sufficient geometry is defined to gather mechanical stress information through centrifugal force analysis. Constrained by material yield strength limit, a rotor geometry that minimizes stress is then critical to maximizing diameter, for which knowledge of underlying physics and factors which influence stress is helpful.

3.3.1 Rotor Stress Theory

Stress mechanics for a simple rotating hollow disk is similar to those seen in pressure vessel design. Centrifugal force is uniformly distributed radially through the entire body of the structure, like pressure in a stationary pressure vessel. The outward load produces two components of stress, radial and hoop stress, σ_r and σ_θ, as shown in Fig. 3.2.

Assuming negligible displacement from axial vibration, stress is greatest at the innermost radius. The radial component of hoop stress, σ_r is zero at the innermost radius; therefore, σ_θ is the only stress component necessary for analytical computation of maximum stress in an ideal rotating cylinder [108].

3.3.2 Centrifugal Force Analysis and Geometric Sensitivity

In the absence of axial vibration displacement, two-dimensional plane-stress finite element analysis can be used to investigate complex rotor geometry. Using Krishnan's design reference, the geometry of a benchmark rotor design was calculated as illustrated in Fig. 3.4 (a) from which the rotor stress distribution was calculated by FEA where the peak stress was found to be 358MPa. To meet the rotational velocity requirement, this stress

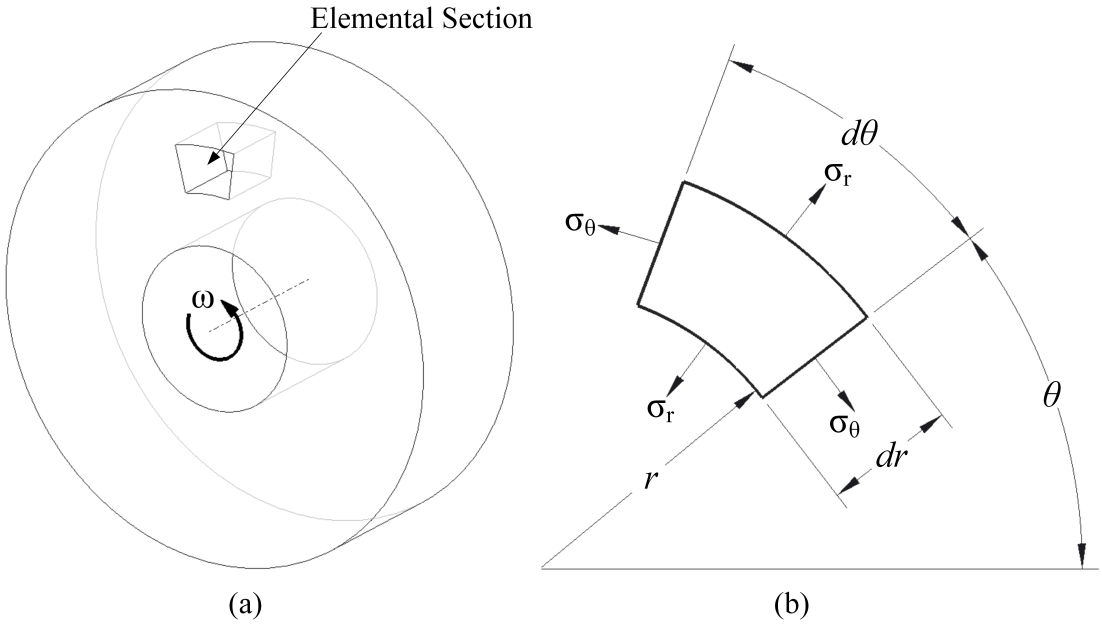

Figure 3.2: (a) Differential element of a rotating disk (b) Stress vectors on a rotating differential element.

value is too high for traditional low silicon steels which generally have yield stress, with a safety factor of 2, between 125 and 220MPa. Design iterations were undertaken to further examine the influence of shaft and backiron geometry influences on stress while maintaining the rotor pole arc angle, the results of which are shown in Fig. 3.4 (b), (c), and (d), where the dimensional parameters described in Table 3.2 are defined in Fig. 3.3.

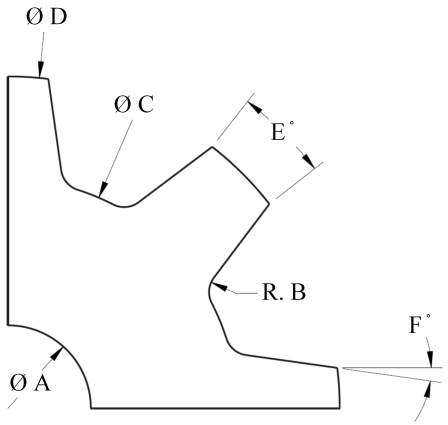

Figure 3.3: Rotor dimension diagram

Table 3.2: Rotor Geometry Definition.

Parameter	Unit	Dim.	Fig. 3.4 (a)	Fig. 3.4 (b)	Fig. 3.4 (c)	Fig. 3.4 (d)
shaft diameter	mm	A	45	55	0	45
tooth root radius	mm	B	5	5	5	5
backiron diameter	mm	C	170	170	170	135
outer diameter	mm	D	220	220	220	220
tooth pole arc	deg	E	14	14	14	14
tooth draft angle	deg	F	3	3	3	3

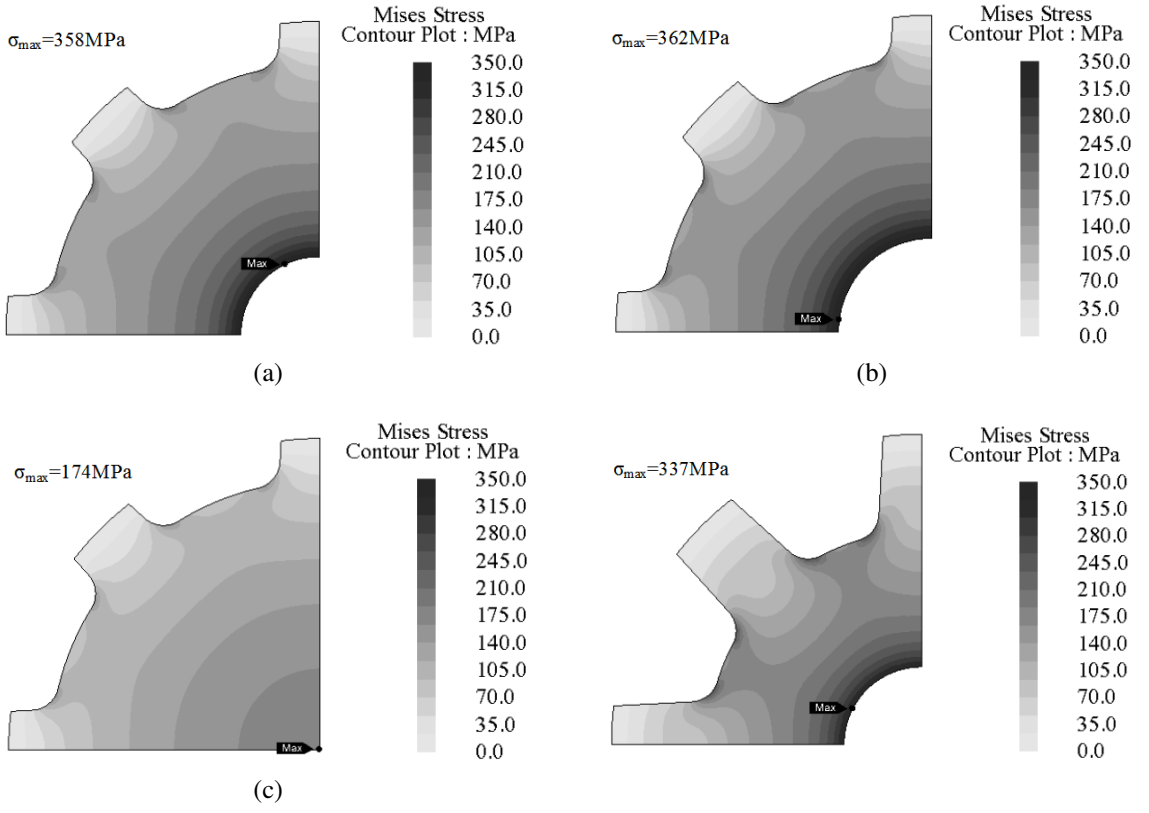

Figure 3.4: Rotor stress contour plots (a) Benchmark rotor geometry (b) Benchmark rotor with increased shaft diameter (c) Benchmark rotor with no shaft (d) Benchmark rotor with reduced back iron thickness.

Several conclusions were drawn from this comparison. First, looking at Figs. 3.4 (a) and (b), a smaller shaft produces lower lamination stress. Second, comparing Figs. 3.4 (a) and (c), the shaft-less lamination design has over 50% less stress than the through-shaft design. The reasoning behind short pole height in the preliminary rotor design, Fig. 3.4 (a), was to reduce windage loss at the expense of reduced saliency. While windage loss is a function of rotor pole height [109], this design choice negatively contributes to lamination stress as seen when comparing Figs. 3.4 (a) and (d), where stress reduces by 21MPa.

The shaft-less design Fig. 3.4 (c) would require careful assembly considerations including balancing and fatigue analysis [81], which was deemed cost prohibitive for the case example. Additionally, the stress reduction seen in Fig. 3.4 (d) was insufficient to reduce stress within the aforementioned yield strength limits for typical low-silicon irons. Before directly addressing mechanical stress with rotor outer diameter reduction, a number of pocketed rotor geometries were simulated to investigate the influence of mass reduction, as illustrated in Fig. 3.5, the geometry of which is defined in Table 3.3, where again, the dimensional parameters are described by Fig. 3.3. From Table 3.3, it is clear that Fig. 3.4 (a) and Fig. 3.5 (a)-(d) have the exact same geometry, differing only by rotor pockets.

Comparing the preliminary design, Fig. 3.4 (a), with the pocketed geometries in Fig. 3.5 (a)-(c), the pockets acted to concentrate stress thus worsening peak stress. However, Fig. 3.5 (d) shows pockets can exist on lamination geometry while having minimal impact on peak stress. The pockets have to be located near the outer periphery of the rotor, where hoop and radial stress is low and effect of stress concentration will be minimal. Still, the geometry in Fig. 3.5 (d) does little to reduce stress. Either a more complex rotor assembly procedure is required, or a smaller rotor diameter is needed to be within the peak stress requirement.

Table 3.3: Pocketed Rotor Geometry Definition.

Parameter	Unit	Dim.	Fig. 3.4 (a)	Fig. 3.5 (a)-(d)
shaft diameter	mm	A	45	45
tooth root radius	mm	B	5	5
backiron diameter	mm	C	170	170
outer diameter	mm	D	220	220
tooth pole arc	deg	E	14	14
tooth draft angle	deg	F	3	3

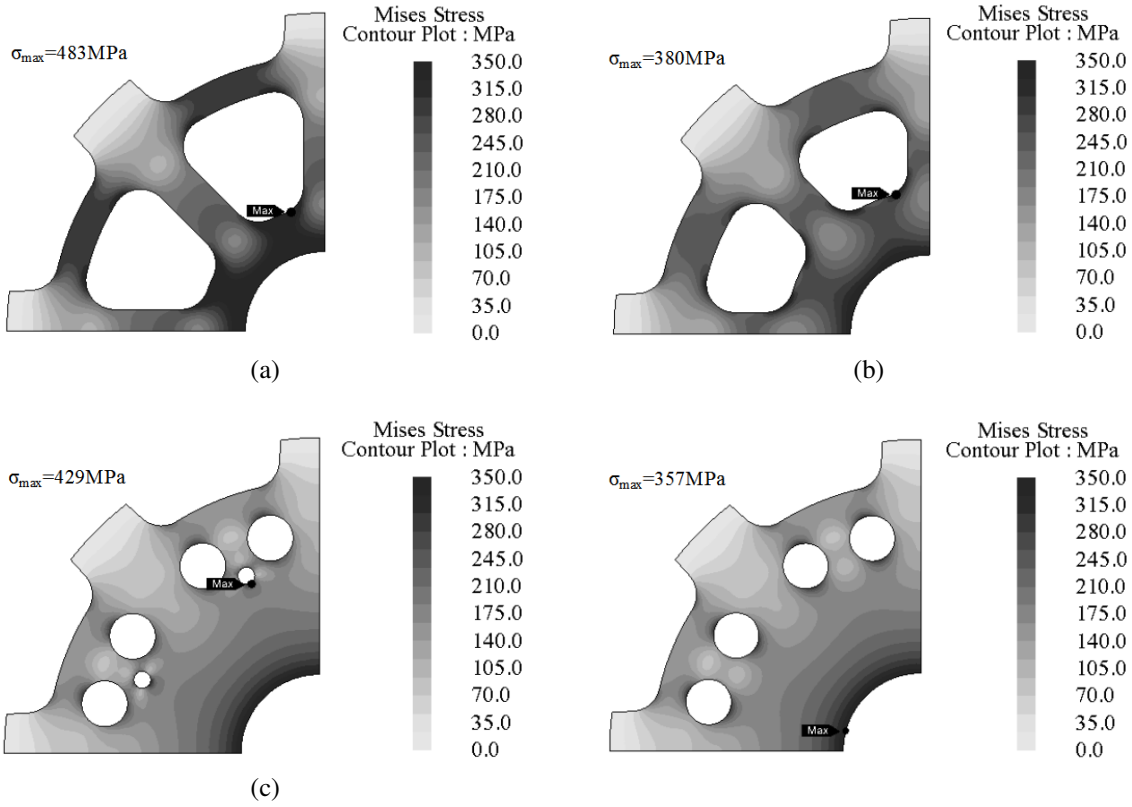

Figure 3.5: Samples of analyzed pocketed rotor geometries.

3.3.3 Key Stress

Keyways and associated keys are common machine elements used to prohibit relative rotation of mated components. Previous analyses, Figs. 3.4 and 3.5, were carried out without keyways, hence an ideal boundary condition showing absolute minimum stress. Even without keyways, centrifugal force analysis made two items clear:

1. Stress is high at the inner diameter of the laminations.

2. Stress was too high for safe operation of the preliminary rotor geometry and all the design variations except the shaft-less rotor which was deemed unaffordable.

In the following simulations, rotor diameter was reduced and keyways were investigated due to their close proximity with natural peak stresses in a rotating system. To investigate the impact of various rotational locking mechanisms on stress distribution, a control case (keyless) and three keyed shaft styles were simulated on the same rotor geometry. Results of the centrifugal analysis are presented in Table 3.4.

Key locking mechanisms create stress concentration which coincides with hoop stress at the inner diameter of the lamination, as shown in Fig. 3.6. Square and round key styles produced stress concentrations unsustainable with the proposed machine material and design method. Double-D type key resulted in the lowest stress, being 54MPa higher than the keyless solution. In all instances, high stress made key type locking mechanisms generally impractical for the case example. The following section will detail an alternative friction fit method of torque transmission which avoids the negative impact of shaft keys.

Table 3.4: Comparison of peak stress of a general rotor with differing key styles at 22,000rpm

Key Style	**Max. Stress (MPa)**
Control Case/No key	299
Square Key	1735
Round Key	802
Double-D Shaft	353

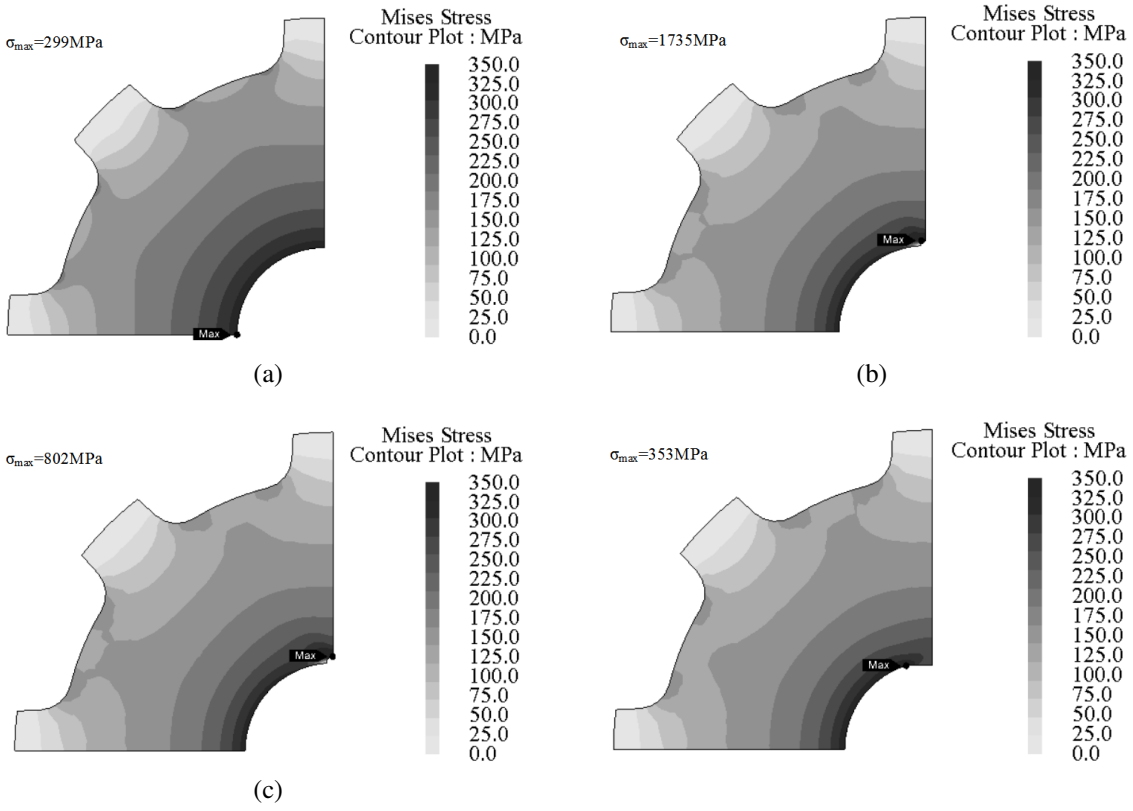

Figure 3.6: Stress distribution of rotational locking mechanisms during rotation. (a) keyless/friction fit benchmark design (b) square key (c) round key (d) double-d (flat)

3.3.4 Rotor End Rings on SRMs

None of the key mechanisms had stress as low as the keyless design. A friction fit which transmits torque to the shaft is clearly the ideal solution; however, the laminations themselves cannot transmit the torque at the risk of over-stressing the laminations, which would cause them to slip on the shaft. Alternative methods of transmitting torque from laminations to the shaft while minimizing mechanical stress are valuable.

3.3.4.1 Rotor Assembly and Torque Transmission

According to Fig. 3.5d, axial holes can be put in the laminations without compromising peak stress. By tolerancing the laminations such that the pressfit breaks free from the shaft at maximum speed, lamination stress will remain approximately constant throughout the entire speed range, mitigating the possibility of fatigue [110]. If the end rings are bolted through the lamination holes, lamination stress is minimized, and higher strength steel can be used for the end rings to transmit torque. Fig. 3.7 shows the basic machine cross-sectional layout of all the components in the assembly. A similar design is seen on an induction machine in [33], where instead of bolts, the end plates are held in place by the induction machine rotor bars. In the induction machine design, beryllium copper end rings are press-fit on the shaft to transmit the torque.

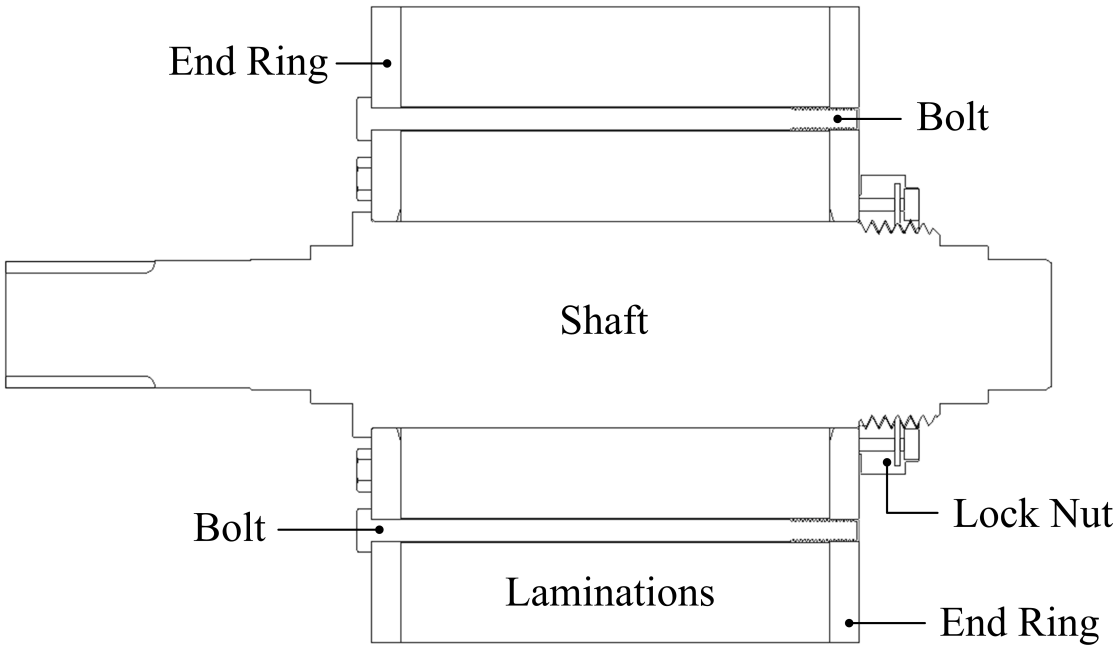

Figure 3.7: Rotor cross-section showing end-ring design which reduces lamination stress.

3.3.4.2 Final Rotor Geometry

Outer diameter for the preliminary rotor design began at 220mm. From Table 3.5 , the outer diameter of the final geometry had to be reduced significantly in order to be within sustainable stress limits. The lamination geometry was updated to fit the end ring mounting requirements and yield strength of Cogent Power NO27 electrical steel [111] with safety factor of 2. Maximum rotor diameter was found to be 170mm, geometry shown in Fig. 3.9a. The location of the bolts which produced lowest stress rise was found to be at the center of the tooth root, concentric with the yoke diameter. The holes are far enough away from the axis of revolution to minimize lamination stress, but also far enough away from the tooth tip that FEA predicts little eddy current generation assuming bolts have minor electrical isolation, which will be discussed in Chapter 4. Fig. 3.9b shows the bolt hole 2.5mm closer to the axis of revolution. The stress increases, because stress concentration from the hole compounds the hoop and radial stresses.

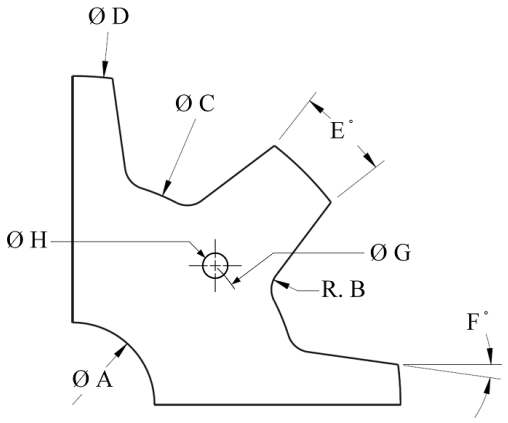

Figure 3.8: Lamination dimensions for the final rotor geometry described in Table 3.5.

Table 3.5: Final Rotor Geometry Comparison

Parameter	Unit	Dim.	Fig. 3.4a	Fig. 3.9a	Fig. 3.9b
shaft diameter	mm	A	45	55	55
tooth root radius	mm	B	5	5	5
backiron diameter	mm	C	170	130	130
outer diameter	mm	D	220	170	170
tooth pole arc	deg	E	14	14	14
tooth draft angle	deg	F	3	3	3
bolt circle diameter	mm	G	n/a	130	125
bolt hole diameter	mm	H	n/a	5	5

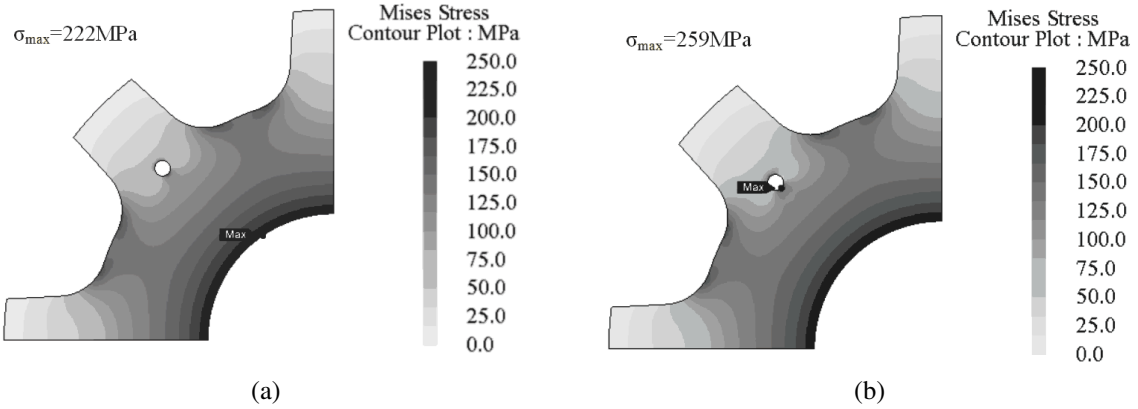

Figure 3.9: Stress concentration for revised rotor with torque transmission holes (a) Hole concentric with backiron diameter (b) Hole 2.5mm inside backiron diameter.

3.3.5 Vibration Considerations for Using Rotor End Rings

Any rotating object is subject to rotationally induced vibrations. The laminations of a rotor will experience both in-plane and axial modes. Axial modes of the laminations are of particular concern. In the centrifugal force simulations shown previously, two-dimensional plane stress is assumed. As the name implies, axial modes can produce large deformation in the axial direction causing significant stress buildup. In this case, peak stress would be on the outer diameter of the rotor laminations, a direct contradiction to the stress theory described in Section 3.3. Applying pressure to the laminations, for example through the use of bolted end plates, can damp these axial vibration modes [112], ensuring a valid plane stress assumption.

3.3.6 Material and Manufacturing Considerations for Using Rotor End Rings

Material selection for end plates is a non-trivial consideration. First and foremost, a material must be selected which has yield strength greater than the laminations themselves, or else a friction fit method of transmitting torque will be unfeasible. Endplates made of soft magnetic material will reduce unaligned inductance, which will decrease torque production capability. Non-magnetic and conductive material, such as aluminum or stainless steel, will be subject to eddy current effects, such as those described in Section 5.3 and by Carstensen [97]. Lastly, the material must have a thermal rating in excess of the maximum rotor operating temperature. In this application, the stator windings are anticipated to have at least a 180°C thermal rating, hence this is used as the worst case soak temperature for the rotor assembly. This eliminates all known plastics and composites such as carbon fiber as potential material choices. Aluminum was eliminated due to low yield strength. Titanium, Copper-Beryllium, and superalloys such as Aermet™

and Inconel are possible options, but were eliminated for not being commensurate with high volume automotive manufacturing practice and cost.

Ultimately, 301 nonmagnetic stainless steel is recommended, which can have up to 965MPa yield strength when fully hardened [113]. End plates should be as thin as possible to minimize rotor inertia. The importance of rotor inertia will be discussed in Section 3.4.2. Making the endplates thin, particularly near the airgap, will also reduce the impact of eddy currents. Care should be taken not to change the magnetic properties of the steel during the manufacturing process or a post processing heat treatment may be necessary to regain nonmagnetic properties.

3.3.7 Aerodynamic Considerations for Using Rotor End Rings

Minimizing windage losses in an electric machine requires that both the rotor and stator be cylindrical and smooth in geometry. Due to the doubly salient nature of switched reluctance machines, achieving a smooth cylindrical rotor and stator surface geometry can be challenging. Often, machine designers will encapsulate a stator with and epoxy or silicon compound in effort to reduce vibration, improve heat transfer and also to create perfectly cylindrical stator geometry. Although this can be a challenging design process for the stator, encapsulating the rotor can be even more challenging due to the additional consideration of centrifugal force induced fatigue loading on the encapsulation material. In permanent magnet machines, where rotor fields and large airgaps can exist, carbon fiber or superalloys such as inconel containment bands are common. In switched reluctance machines, the small airgap inhibits the use of high strength containment bands. Although high-speed containment band concept designs have been presented [44], perhaps the easiest way to reduce windage is through the use of end plates. According to Vrancik, rotor endplates prevent airflow churning between the poles, resulting in lower losses [109].

Vrancik presents three relations to estimate power loss of salient rotors: an idealized model, a model for salient rotors without end plates, and a model with end plates.

For a shrouded rotor, Vrancik uses a simple two step loss calculation relationship. First, ideal cylindrical rotor windage losses are computed. Second, an empirically determined multiplier is applied to the ideal rotor losses. Vrancik expresses uncertainty of the correlation validity with respect to other geometries; however, Kiyota uses the unshrouded relations with reasonable success in [114].

The speed dependent relationship of the windage loss in Fig. 3.10 shows the simplified approximation, in addition to the maximum and minimum possible loss provided by the unshrouded approximation and the ideal cylinder approximation.

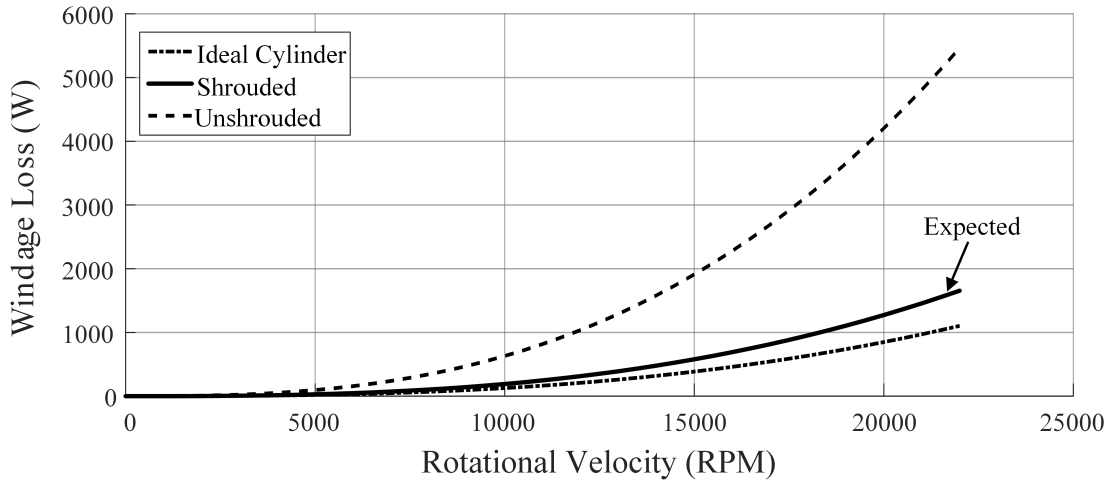

Figure 3.10: Windage loss versus rotational velocity. Maximum (unshrouded) and idealized loss magnitudes are shown in addition to the expected (shrouded) loss generation.

As expected, loss increases as a cubic function with speed. At maximum speed, windage losses could account for as much as 5.5kW for the unshrouded case. For the shrouded case, windage losses are around 1.6kW. Any error in the estimation is expected to be small when compared with the total losses of the machine.

3.4 Maximizing Stack Length

The second and final step in determining maximum rotor volume is analyzing rotordynamics to determine the largest possible stack length. Rotordynamics is the study of vibrations induced by rotation. Dynamic analysis investigates stresses, deflections, forces, and system resonances. Excessive machine dynamics will result in structural failure; therefore, identifying when failure occurs will constrain the rotor design.

3.4.1 The Rotor-Bearing System

When designing a machine, a decision must be made for a rigid or flexible shaft. The difference between rigid and flexible shafts is generally understood to be defined as whether or not the first vibration mode is within the operation range of the motor. Rigid shafts will not experience a resonant mode within their operating range, whereas flexible shafts will experience resonant modes at some point throughout their speed range. Examples of the first three lateral vibration modes are shown in Fig. 3.11.

Shaft type is usually defined in the specification requirements by the bearing best for the application. In general, a rigid shaft design is preferred for machines using rolling element bearings due to their inherent low damping characteristics. Additionally, the rotor balancing process is simplier for rigid shafts. Simple analytical approximations can be used to determine resonant frequency of rigid shafts. Basic FEA models can also be used for rigid shafts, and are strongly recommended for flexible shafts.

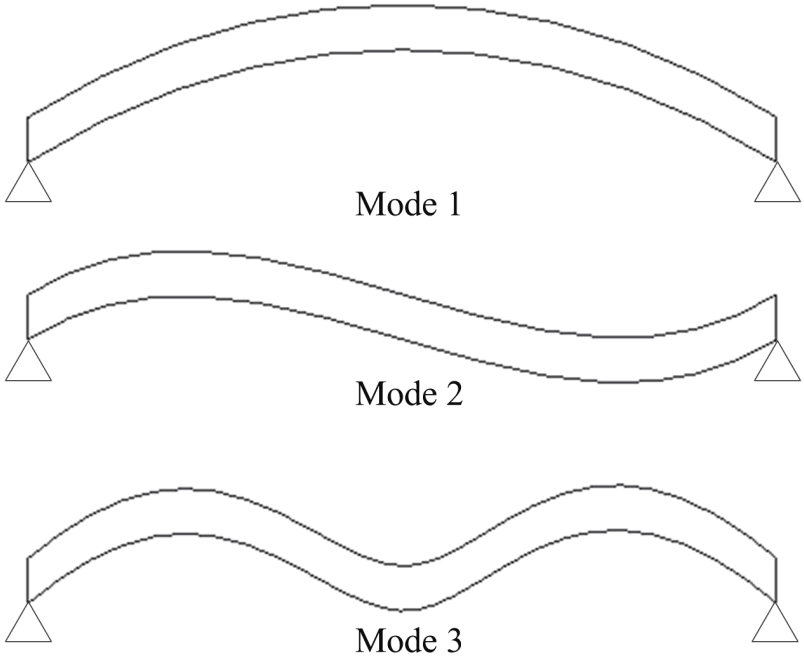

Figure 3.11: Lateral mode shapes of a rotating machine.

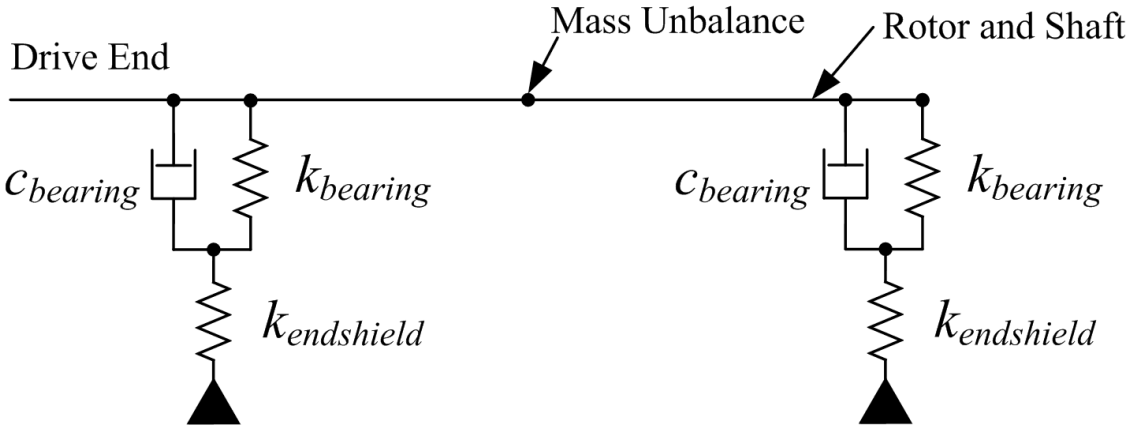

Figure 3.12: Simple rotordynamics diagram showing rotor, bearings and support structure.

3.4.2 Modeling

Mode frequency determination depends on material characteristics, rotor geometry, bearing and support structure stiffness. Flexible shaft simulations, on the other hand, also require knowledge of bearing damping characteristics, and more complex analysis to determine shaft stability. Fig. 3.12 shows a basic rotordynamics model with all the critical structural components. In the case of either a rigid or flexible shaft, thorough analysis requires detailed knowledge of the machine design.

End shield stiffness, $k_{endshield}$, is visualized much like compression springs, where thicker, shorter, or less elastic material makes the spring less susceptible to deformation from an input force. End shield stiffness is determined by Hooke's Law:

$$F = kx \tag{3.1}$$

where F is the force applied, k is the stiffness and x is resulting displacement.

For end shield stiffness, a force is applied to the bearing surface and displacement is estimated either analytically or from FEA. Magnitude of applied force is divided by the resulting displacement to get stiffness. Similarly, shaft stiffness, while not explicitly quantified as a number, exists in rotordynamic models as a function of length, thickness and material elasticity. Lamination contribution to shaft stiffness can be assumed negligible and modeled as added mass and inertia to the shaft for certain rigid shaft systems [115]; however, this assumption may be unreasonable for certain flexible shaft systems [116, 117]. Most efficient rotor stiffness approximation; therefore, requires case-by-case consideration.

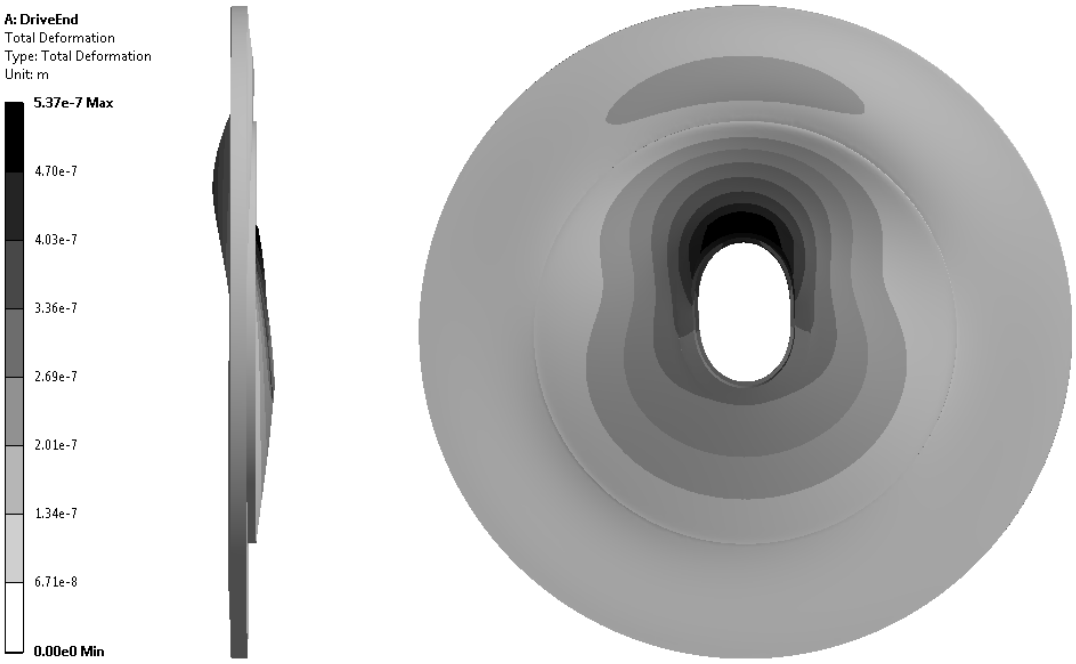

(a)

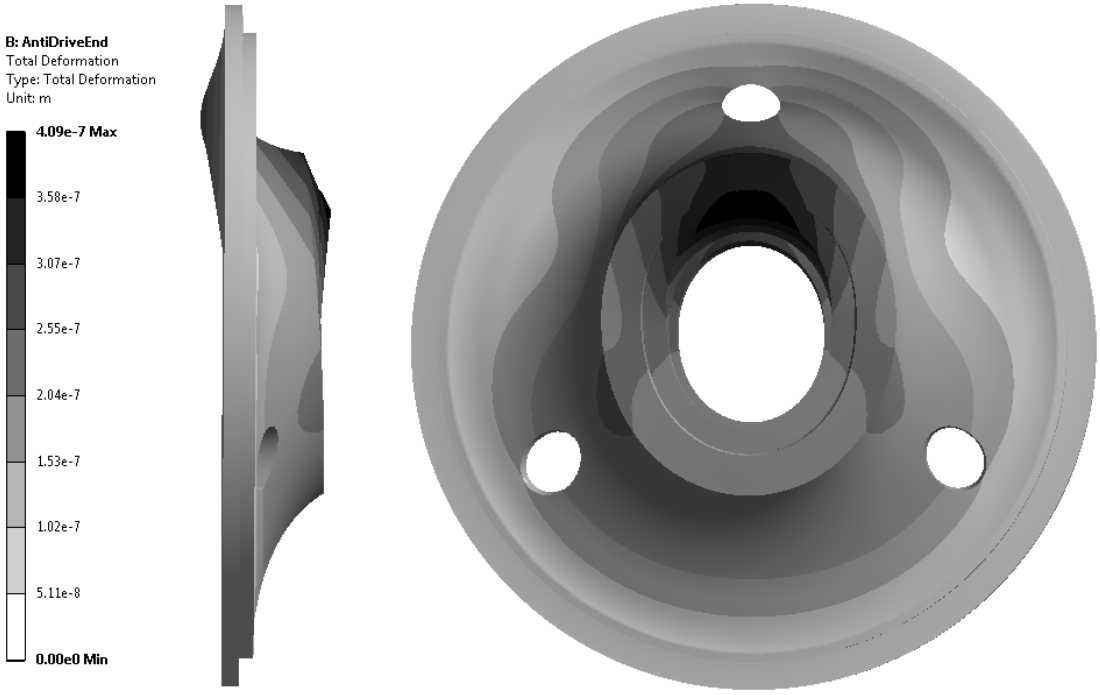

(b)

Figure 3.13: Total deformation for (a) drive-end support (b) anti-drive-end support. Both supports are fixed at the outer periphery with 1000N applied to the bearing seats.

Figure 3.13 shows the deformation results for the end shield stiffness analysis. In the case of the drive end, bearing overhang is small and reaction force is transmitted directly through the peripheral fixation constraint, resulting in small deformation. For the anti-drive end case, bearing overhang is larger. Bearing reaction force creates a moment which increases deformation at the bearing seat. Maximum deformation is used to compute the effective stiffness. The drive end, Fig. 3.13a, is an aluminum structure with a hardened steel bearing sleeve. Here, 1000N of applied force results in $0.54\,\mu\mathrm{m}$ deformation. The anti-drive end, in Fig. 3.13b, is a steel structure and also has a hardened steel bearing sleeve. Here, 1000N of applied force results in $0.41\,\mu\mathrm{m}$ deformation. With a 1000N input bearing force, drive and anti-drive end shield stiffness is $1.85 \times 10^9 \frac{N}{m}$ and $2.4 \times 10^9 \frac{N}{m}$, respectively. If the anti-drive end support was made of aluminum, peak deformation was found to be $0.84\,\mu\mathrm{m}$ with stiffness corresponding to $1.2 \times 10^9 \frac{N}{m}$, which was thought to be too low to meet application requirements without further investigation.

Bearing stiffness and damping, $k_{bearing}$ and $c_{bearing}$ on the other hand, are more complex values to quantify. Bearing parameters are dependent on rotational speed, material properties, bearing fit, bearing type, lubrication, cooling, and a number of other parameters entirely controlled by the designer. A comparative analysis of various mechanical design features and their impact on bearing stiffness is presented in [118]. Determining stiffness requires either an analytical, FEA, or physical test based estimation such as those presented in references [119, 120]. In this case example, angular contact ball bearings and a rigid shaft design will be considered.

To design a rigid shaft rotor with high torque capacity, the shaft, bearings, and housing all require high stiffness designs. Any individual component with low stiffness can result in an undesirably low critical speed. Low critical speed can be overcome by reducing bearing center-to-center distance at the expense of shorter stack length; however, this impacts rotor volume and hence maximum torque production. A few guidelines to

increase system stiffness are:

- Select a bearing with largest possible diameter meeting application rotational velocity requirements with a specific lubrication method.
- When considering bearings of a certain diameter, select one with as many rolling elements as possible. More rolling elements results in greater radial stiffness.
- For angular contact bearings, a smaller contact angle results in higher radial stiffness.
- Use ceramic or hybrid-ceramic bearings where viable for increased radial stiffness, enhanced life expectancy, and lower rotational inertia.
- Usage of multi-row bearings can increase stiffness, but stiffness is not a direct multiple of the number of rows used. Additionally, multirow bearings are more challenging to cool and the losses are greater.
- Minimize rotor mass and inertia as much as possible.
- Make bearing center-to-center distance short as possible.

In this example, bearing stiffness for SKF 7009 CE/HCP4A, a high-precision, hybrid-ceramic, 45mm bearing, was estimated by manufacturer approximation and validated with commercial software at maximum speed. The manufacturer approximation was the most conservative stiffness estimate at $7.5 \times 10^7 \frac{N}{m}$, and was used in the simulation. In this example, bearing damping contribution is assumed to be negligible, so the rotordynamics model simplifies to two stiffnesses, $k_{bearing}$ and $k_{endshield}$, in series.

The mass and inertia properties for the end plates and the rotor geometry selected in Section 3.3.4.2 was calculated for various stack lengths. The shaft length was resized proportionally for each stack length, subsequently modifying bearing center-to-center distance in an iterative rotordynamic analysis.

3.4.3 Results Analysis

Results of rigid-shaft rotordynamics analysis can be described with resonant frequencies from modal analysis; however, forced response analysis more broadly describes both rigid and flexible shaft systems. Forced response analysis can be used to examine any forces on system response. The most common force in rotating systems is from mass unbalance. Rotor unbalance is an important parameter to consider in any system, because it quantifies the balance specification needed for manufacture; impacts bearing lifetime, and influences noise and vibrations. In this iterative study, an ISO 1940/1 compliant G6.3 balance specification was considered for several stack lengths.

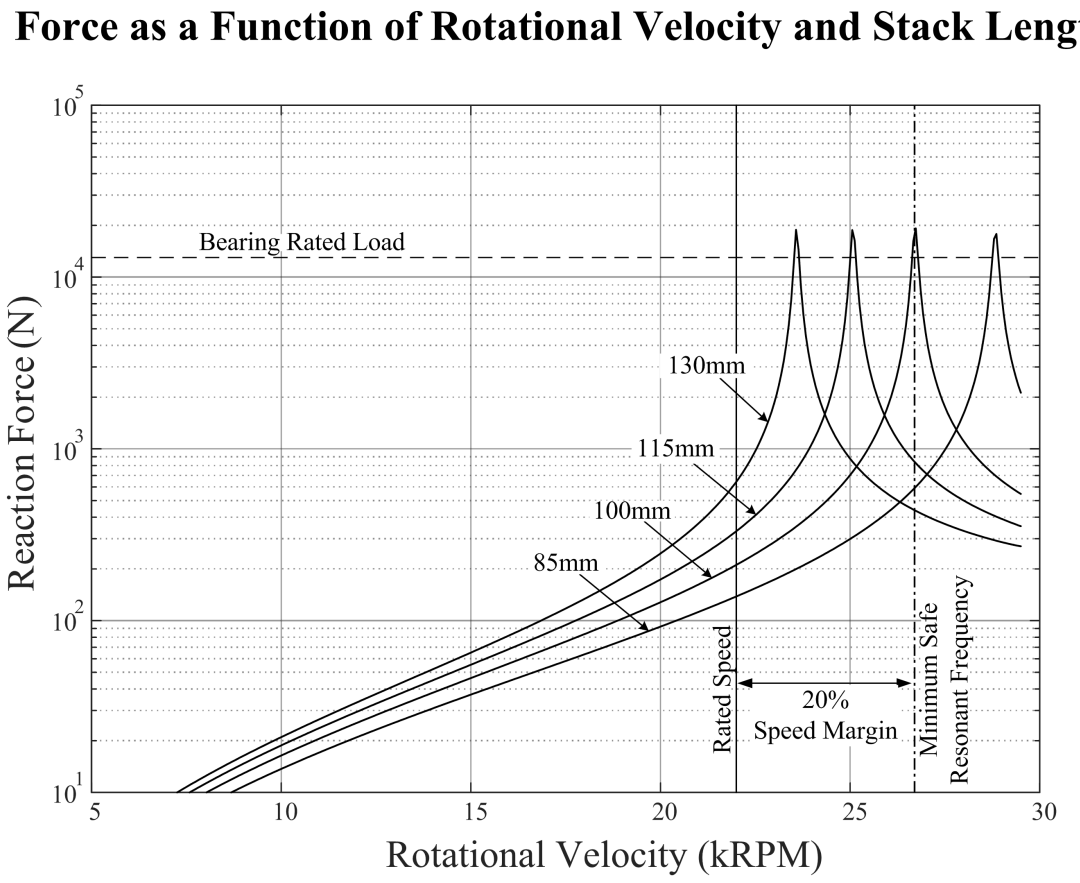

Figure 3.14: Bearing reaction force for a G6.3 rotor balance specification with differing stack lengths at 0.5% structural damping.

Bearing reaction force produced by unbalanced mass is shown in Fig. 3.14. As each rotor approaches resonance, reaction forces encroach on bearing load rating. For rigid shaft rotors, common industry practice is to put the first critical speed 20% above the maximum operating speed of the motor. Peaks of the curves represent resonant frequency, or critical speed, for each depicted stack length. Stack lengths of 130 and 115mm result in critical speeds which fail to meet the rigid shaft speed requirement. The 85mm stack length exceeds the rigid shaft speed requirement; however, when determining maximum rotor envelope, exceeding industry design practice is needlessly conservative. The 100mm stack length meets the rigid shaft speed requirement at the ideal 20% over-speed design margin.

Unless the rotor-bearing system is upgraded to accommodate a flexible shaft type design, the resonate frequency indicates a mechanical limit on stack length. Of course, upgrading to flexible type shaft design comes at a financial and often complexity penalty.

The next phase of the design process is magnetic design using the defined rotor envelope. If after magnetic optimization with the defined rotor envelope and DC link voltage, torque is shown to exceed torque requirements, the designer can optimize winding for higher efficiency, or shorten stack length to reduce machine mass.

3.5 Conclusions

A new design methodology is presented for switched reluctance machines. The design methodology characterizes maximum rotor volume at rated speed, resulting in full utilization of a motor's mechanical performance envelope. Magnetics are later designed and optimized around the rotor envelope, subsequently resulting in maximum possible torque production for a specified speed rating and core material. The proposed design procedure offers several benefits including: guaranteed robust design, fewer design iterations, designs prioritizing diameter over length, in addition to enhanced optimization flexibility.

The method uses two structural mechanisms to govern rotor design: lamination stress, and shaft dynamics. Lamination stress and material strength limits maximum outer diameter of the rotor, while shaft dynamics dictate maximum stack length based on the bearing arrangement and shaft. Analysis of these structural characteristics result in the maximum obtainable rotor volume for a rotor material, design speed, shaft and bearing style. For the case example, a 0.27mm silicon steel with 440MPa yield strength was considered at 22,000rpm. The maximum rotor diameter for the 8 pole rotor was found to be 170mm with a maximum stack length of 100mm.

Chapter 4

Magnetic Design and Loss Minimization in a High-Speed Switched Reluctance Machine

4.1 Machine Magnetics

Preliminary magnetic analysis of a 22,000rpm SRM strongly indicated high power capability using a 0.35mm M-19 grade silicon steel lamination [100]; however, it was concluded in Chapter 3 that significant rotor structural improvements were necessary to meet the performance requirements. Note, 0.35mm M-19 grade is a high quality silicon steel finding acceptance in industrial induction and permanent magnet machines due to increasing pressure for higher efficiency machine-drive systems.

After consideration of mechanical factors in Chapter 3, the rotor geometry has been fixed. The next step in the design process, according to the design procedure in Fig. 4.1, is to design a stator around the rotor and confirm acceptable torque, power, speed and efficiency requirements, as highlighted in the dashed section of Fig. 4.1 (Fig. 3.1 specific

to Chapter 4).

The next step in determining the magnetic performance of the proposed machine is definition of the stator and winding details, pole topology, pole design, number of coil turns and lamination material. Reference [100] suggested low speed control may be problematic for the preliminary design proposed in Chapter 3, so the low speed, base speed and rated speed torque characteristics will be re-evaluated here.

4.1.1 Pole Topology

As previously mentioned in Section 3.2, the magnetic requirements for this research were largely self-imposed, by the consideration for high volume, low cost automotive application. A design was sought that, as much as possible that realized a balanced pole topology, with equal importance assigned to efficiency, reliability, magnetic mass, torque quality, noise and vibration. A low phase count machine, for drive simplicity and self-starting capability was considered, hence design options were restricted to three phase machines. A phase count restriction effectively limits the available pole choices to 6/4 and 12/8 configurations. Of course, the 12/8 combination has higher rotor and stator frequencies than the 6/4 indicating increased core loss. On the other hand, the 12/8 is expected to have improved torque ripple. The 12/8 has parallel pole excitation and will excite a fourth order resonant mode as opposed to a second order resonant mode with the 6/4, suggesting that the 12/8 would offer quieter operation as mentioned in Section 6.4. To exhaust an additional pole configuration, Chapter 6 examines a three-phase 12/10 topology comparing acoustics, vibrations and magnetics with a geometrically similar 12/8. Ultimately a 12/8 machine was selected for later analysis.

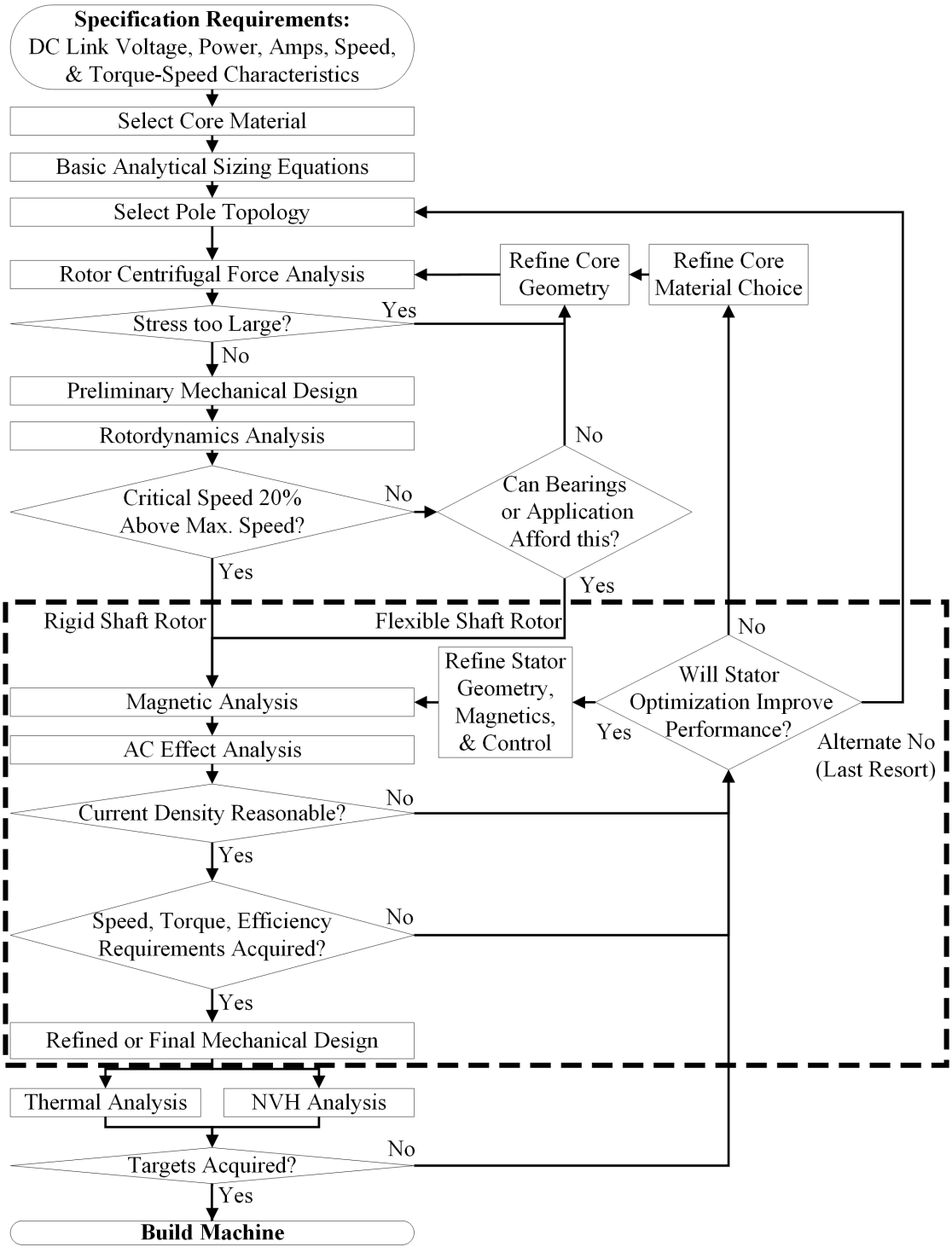

Figure 4.1: Design procedure of Fig. 3.1, highlighted to illustrate the discussions of Chapter 4.

4.1.2 Material Selection

Lamination steel selection is an important design parameter to achieve automotive industry performance and cost requirements. A number of silicon steels were considered such as M-19 from AKSteel [121]; M235-35A, NO18, NO20 and NO27 from Cogent Power were also contenders [122]. To comply with common industry design practices, laminations thinner than 0.18mm and thicker than 0.35mm were not considered. Additionally, exotic electrical materials such as vanadium cobalt or amorphous materials, as used by other researchers of high power machines [43, 82], were not considered for this application.

Summarizing, M19 has good saturation flux density properties, but has low yield strength characteristics; NO27 has a 0.5T lower saturation flux density, but a yield strength approximately 25% higher than M19; NO27 is a non-oriented 0.27mm thickness lamination, whereas M19 is a non-oriented 0.35mm lamination. While M19 is cheaper based on lamination thickness, NO27 is superior in terms of losses and yield strength, which are material characteristics critical to obtaining high power at high frequency. NO27 was ultimately chosen as it offered a balance between yield strength, magnetization properties, and core loss.

4.1.3 Main Magnetic Dimensions

The rotor diameter and length was predefined by the structural analysis discussed in Section 3.3 and 3.4. The rotor should have as small a pole arc angle as possible to reduce rotor mass, inertia, and centrifugal stress, yet not produce discontinuous torque. The pole height, back-iron thickness, and fillet radii were not chosen for specific magnetic reasons, but to minimize mechanical stress as much as possible.

The stator design was more flexible due to fewer mechanical constraints. Here, a larger back-iron dimension than was required magnetically was selected to minimize stator

deflection due to radial forces, a feature that also helped reduce back-iron core losses due to the lower flux densities in this region. The stator pole arcs were chosen to be as small as possible trading average torque with torque ripple, but large enough to mitigate issues with discontinuous torque. The stator pole arcs are slightly smaller than the rotor pole arcs, per analysis provided by Krishnan [90]. The stator outer diameter was fixed at 268mm such that the machine would fit the custom designed wrought aluminum cooling jacket detailed in Section 5.2. A larger diameter would have required a bespoke casting, which was not considered cost conscious for early prototype manufacture. A list of the machine dimensions is provided in Table 4.1.

The parallel connected winding 12/8 machine as depicted in Fig. 4.2 produces two distinct flux paths including (a) short-flux paths and (b) long flux paths for the machine magnetic field as illustrated in Fig. 4.3 which shows example FEA flux field solutions illustrating both scenarios. The short flux path occurs during phase commutation, whereas the long flux path occurs during phase conduction, with both situations being dependent on rotor position.

4.1.4 Winding Turn Selection

With the main stator geometry dimensions defined, the next step in the magnetic analysis is to decide on the number of turns. Assuming that the total conductor cross-sectional area and total Ampere-turns are fixed (for thermal considerations, as discussed later) the number of turns has many implications on machine performance. The first implication of turn selection is location of the base speed on the torque-speed envelope. As seen in Fig. 4.4, a given number of turns, N, results in a constant torque-speed envelope, whereas increasing N-turns results in a reduction of the machine base speed. However, the torque at maximum speed may not be sufficient to satisfy the machine power-speed specification.

Table 4.1: Machine Parameter Definition.

Component	Parameter	Unit	Value
Stator	pole count	#	12
	outer diameter	mm	268
	backiron thickness	mm	20.75
	airgap diameter	mm	171.2
	tooth pole arc	deg	14
	tooth draft angle	deg	0
	tooth root radius	mm	5
	stack length	mm	100
Rotor	pole count	#	8
	outer diameter	mm	170
	backiron thickness	mm	25
	shaft diameter	mm	65
	tooth pole arc	deg	14.3
	tooth draft angle	deg	3
	tooth root radius	mm	14
	stack length	mm	100
Windings	supply voltage	VDC	600
	turns	#	30
	winding connection	parallel	4 coils/phase
Core	lamination material	n/a	NO27
Specification	speed	krpm	22
	torque	Nm	78

Here, some fine tuning of the number of turns and stator current magnitude is required to ensure that the torque at base speed and maximum speed is realizable. For example, high number of turns may satisfy torque at base speed within a reasonable phase current. However, torque at high speed may then not be satisfied due to an excessively high winding impedance at maximum speed, as discussed by Schofield et al [123]. The envelope shape selection is governed by a number of factors, for example industrial servos or traction machine applications. For the industrial servo, a constant torque-speed envelope (N turns as described in Fig. 4.4) is usually required whereas for traction, a high

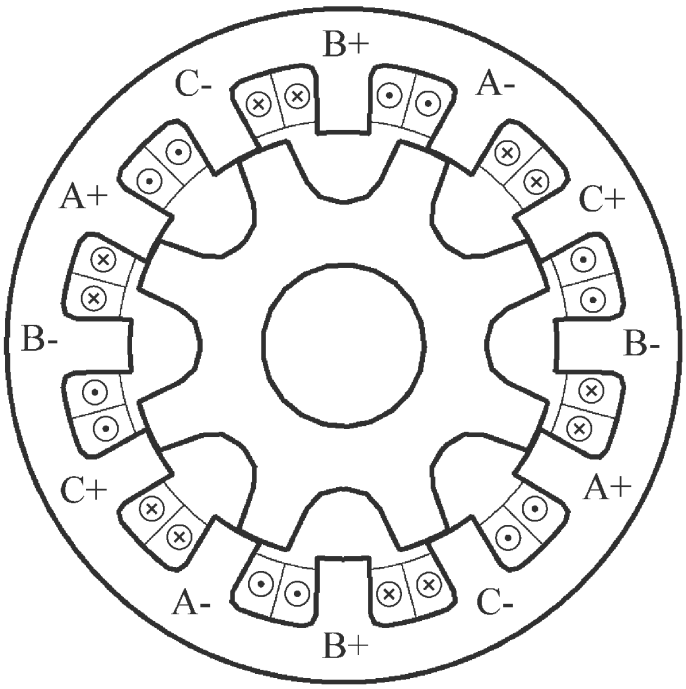

Figure 4.2: Winding diagram for the 12/8 switched reluctance machine.

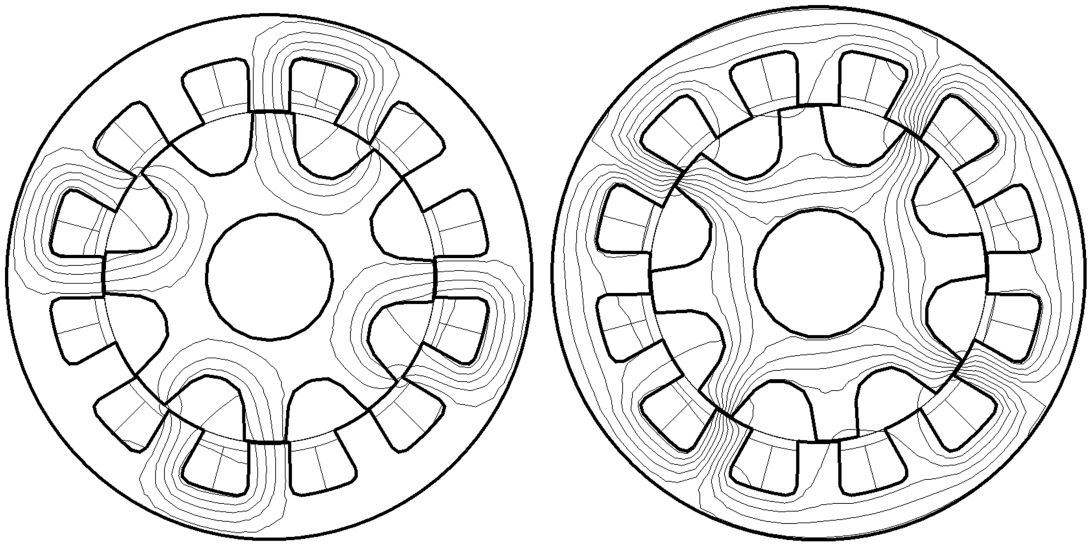

(a) (b)

Figure 4.3: Example FEA field solutions for a 12/8 machine demonstrating (a) the short flux path (b) the long flux path.

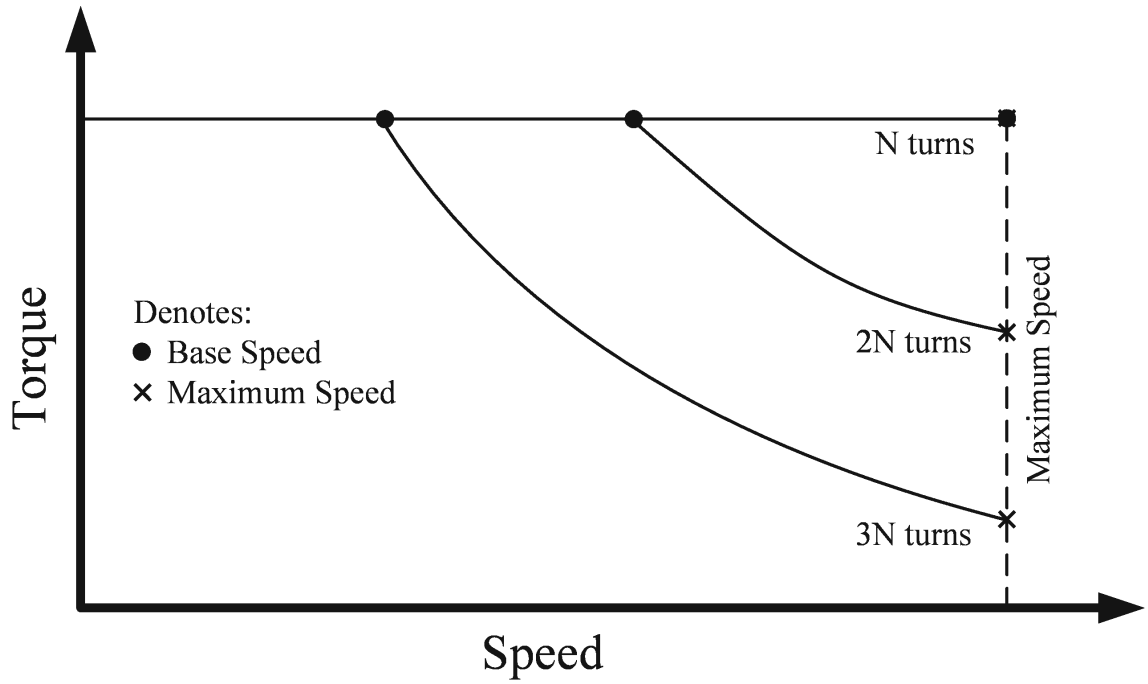

Figure 4.4: Performance impact of turns on a fixed stator geometry.

torque at low speed low torque, power at high speed envelope (2 and 3N turns in Fig. 4.4) is usually required. Generators may need a large constant power region to efficiently deliver the rated DC link voltage and power over a wide speed range [123, 124].

For a winding constrained by fixed slot area, the winding resistance is proportional to the square of the number of turns, while winding joule loss is given by Eqn. 4.1:

$$P_{winding} = m{I_{phase(rms)}}^2 R_{phase} \tag{4.1}$$

where m is the number of phases, $I_{phase(rms)}$ is the phase current and R_{phase} the phase resistance.

Schofield et al [123] discussed the choice of turns number and their approach was taken to iterate around the most suitable number of turns that ensured torque at base and maximum speed while minimizing phase current over the whole speed range. The study used the

FEA model targeting the base and maximum speed specifications, and then checking the intermediate speeds.

The machine power converter DC link voltage is fixed at 600VDC. Parallel connected windings, each of 30 turns, was calculated for the machine's three phase winding. The winding conductors under consideration have a 200°C thermal class with double build insulation.

Single strand rectangular wire was selected to construct the windings turns. Rectangular wire was selected to minimize eddy currents which will be discussed later in Section 4.3.3. The rectangular wire is approximately equivalent in area to 11AWG round wire. The resulting characteristics of machine geometry of Fig. 4.2 are solved via JMAG®, a finite element software tool.

4.1.5 Machine Static Characteristics

The static flux-linkage versus current profile is illustrated in Figure 4.5 showing that the machine enters initial saturation around 100 amps and is heavily saturated at 240 amps. The static flux-linkage and torque verse angle profiles are illustrated in Figs. 4.6 (a) and (b) respectively, with phase current ranging from 20 to 460A and showing a peak torque of around 160Nm at 460A.

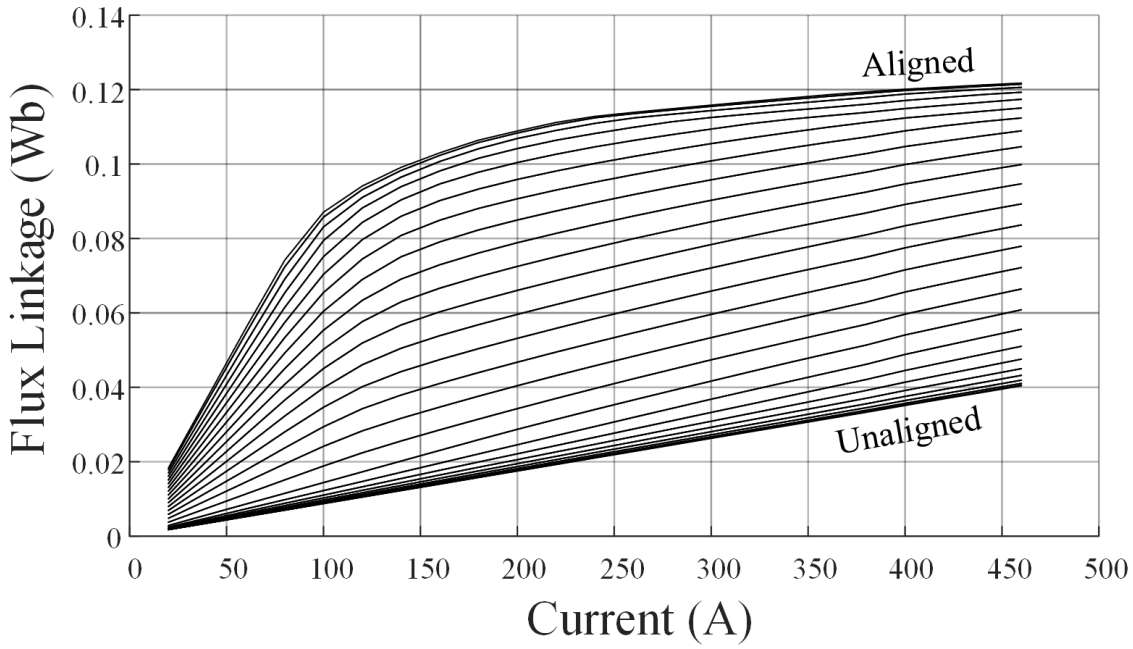

Figure 4.5: Finite element generated flux linkage versus current ($\lambda - i$) characteristic for the 12/8 machine.

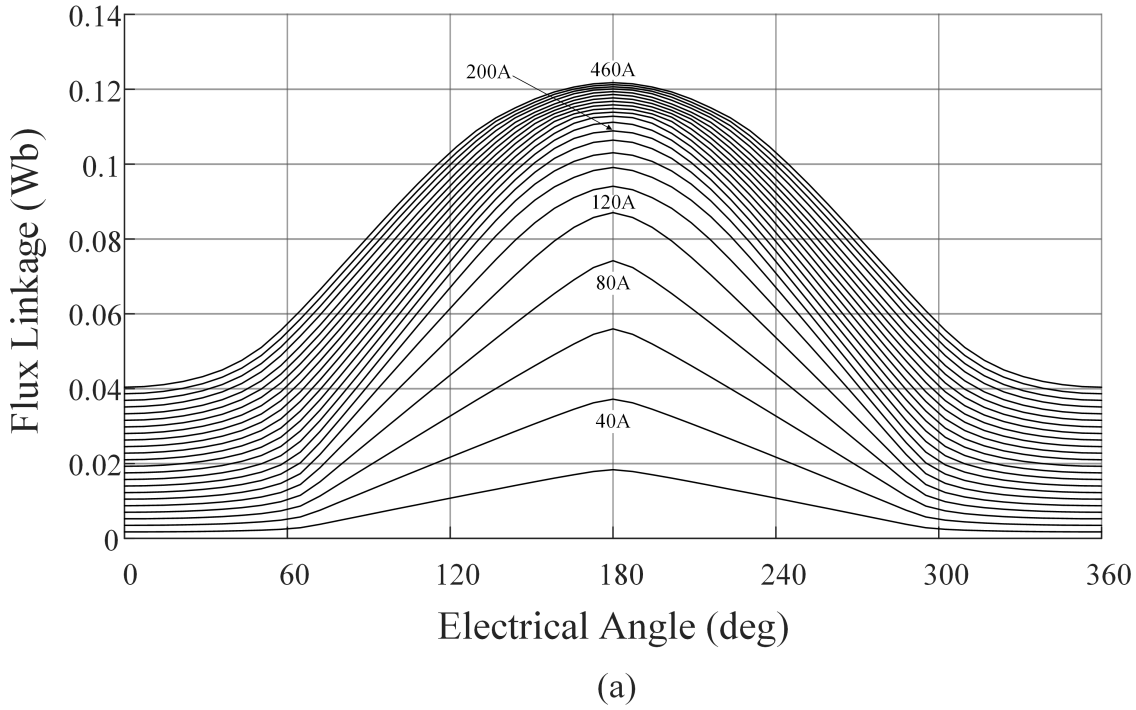

(a)

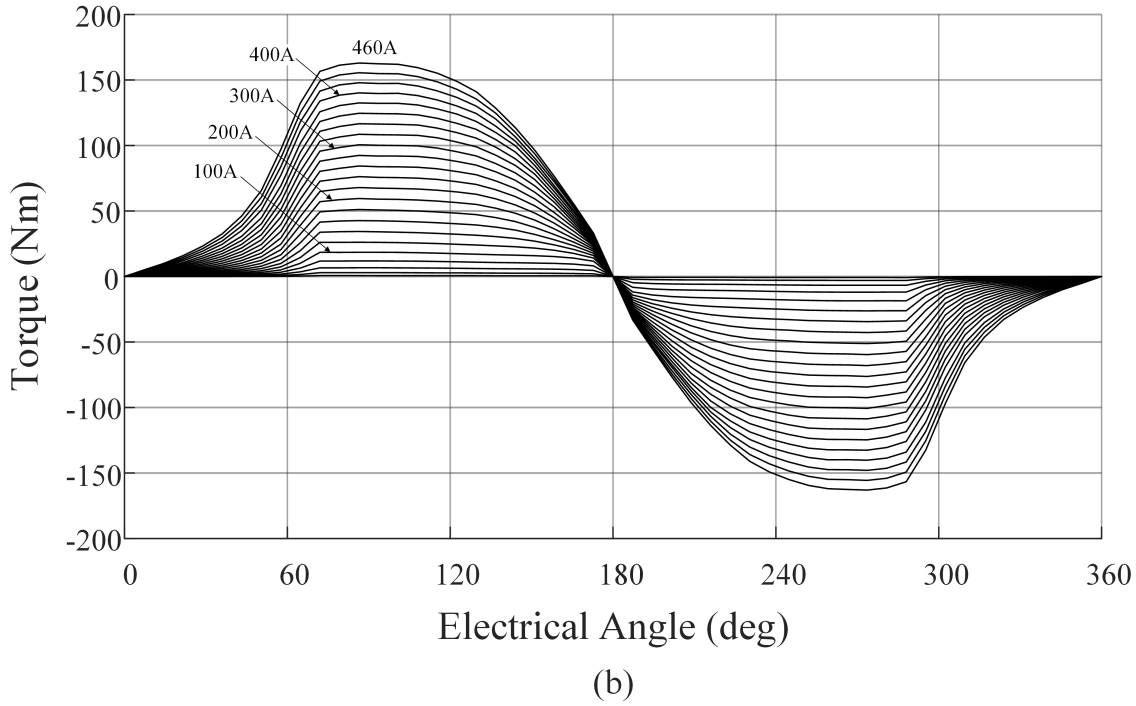

(b)

Figure 4.6: Finite element generated static (a) flux linkage and (b) torque profiles for the 12/8 machine.

4.2 Transient Machine Analysis

To verify machine performance complies with design constraints, transient performance was simulated at maximum rated speed (22,000rpm), low speed (1,000rpm) and base speed (15,000rpm). The procedure to determine optimum conduction angles will be discussed here.

4.2.1 Conduction Angle Optimization

Figure 4.7 defines the basic timing theory of machine phase currents with respect to rotor position, illustrated at three positions, below base speed (a), at an intermediate speed (b) and at maximum speed (c). The current commutation is influenced by two control variables, turn-on and turn-off angles.

For this investigation conduction angles were optimized based on the work of Peng et al [125]. Conduction angles were optimized at two speeds known to be in the constant power region, in this case 17,000 and 22,000rpm. Assuming constant power between the two speeds, the optimization objective function realizes at the respective speeds, torque of 73 and 94.5Nm, while minimizing phase current. The algorithm output turn-on and turn-off angles optimized for Torque per Amp ratio:

$$\frac{\tau_{avg}}{i_{rms}} \tag{4.2}$$

where τ_{avg} is the electro-magnetic torque averaged over an electrical cycle and i_{rms} the corresponding RMS phase current.

Li et al. [100] showed that linear control of the machine is possible over a wide speed range; therefore, for simplicity, a linear correlation was drawn between the resulting conduction angles, represented in Fig. 4.8. Inspection of the linear correlations shows that

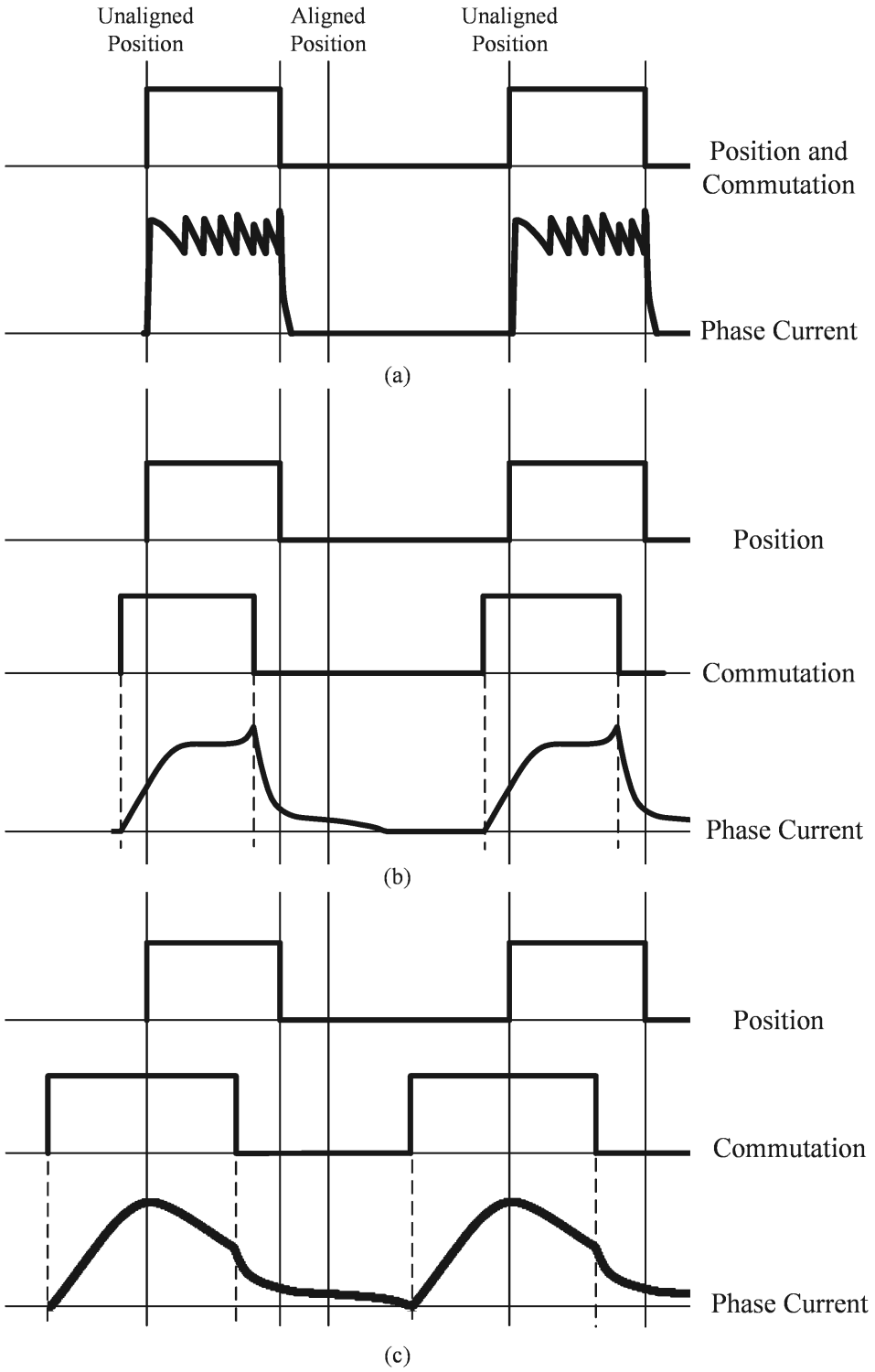

Figure 4.7: Rotor position (angle) and phase current commutation waveforms.

at zero speed, the conduction period is in the order of 90° electrical degrees. Due to the low rotational velocity and correspondingly low rate of change of flux-linkage, current cannot be expected to trail beyond the turn-off angle, as is expected at higher speeds, which will result in dis-continuous torque as discovered by Li et al [100]. As a result, the low speed turn-on angle was shifted to achieve a 120° conduction period. The new correlation is also represented in Fig. 4.8.

Fig. 4.9 has superimposed points representing the turn-on angles for the transient simulations presented in Section 4.2.2. For this simple magnetic performance evaluation, turn-off angles were assumed to be explicitly represented by the speed-dependent turn-off angle expression described in Fig. 4.9 It should be noted that the linearized angles in Fig. 4.9 are used as the control basis for the performance maps shown throughout the remainder of the Chapter.

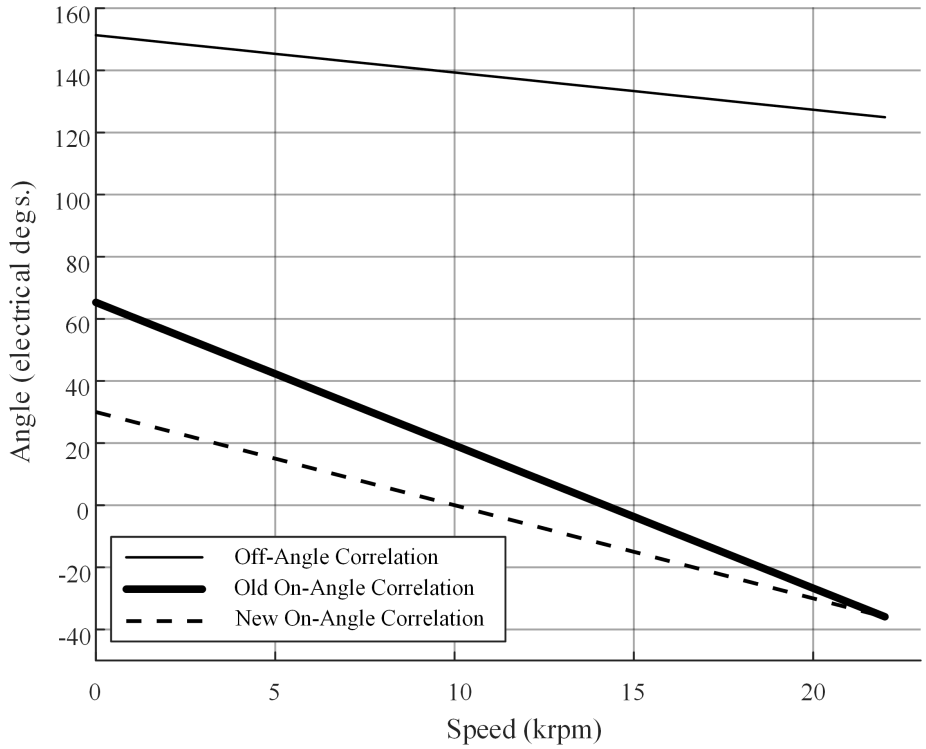

Figure 4.8: Optimized and modified conduction angle correlations as a function of speed.

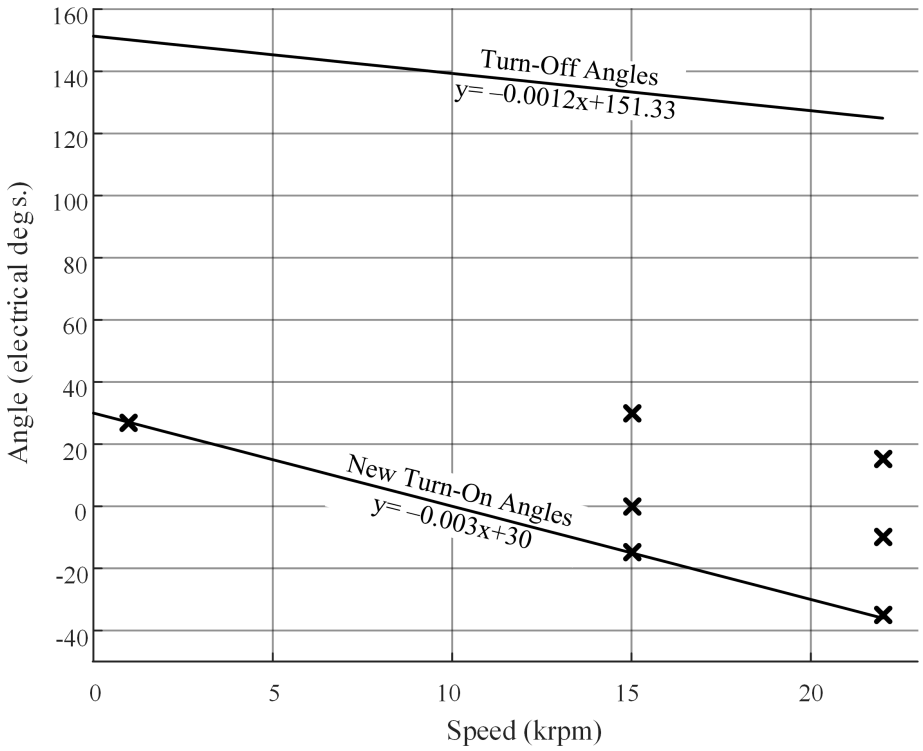

Figure 4.9: Linearized conduction angles as a function of speed.

4.2.2 Transient Simulation Results

Figure 4.10 illustrates transient simulations results for machine torque and current for varying switching angles, below base speed, at 1,000rpm. Here we can see the machine torque pulsations are due to the low frequency switching capability (PWM) of the large power electronic switching devices considered. Torque quality is not ideal, nor is it discontinuous. Figure 4.11 illustrates simulations results for machine torque and phase current for varying switching angles at a speed of 15,000rpm. Figure 4.12 illustrates simulations results for machine torque and phase current for varying switching angles at the maximum speed of 22,000rpm. Here it can be seen that the machine produces 170kW at 22,000rpm. Including efficiency performance degradation via windage and frictional losses, this design will easily yield 150kW at maximum speed.

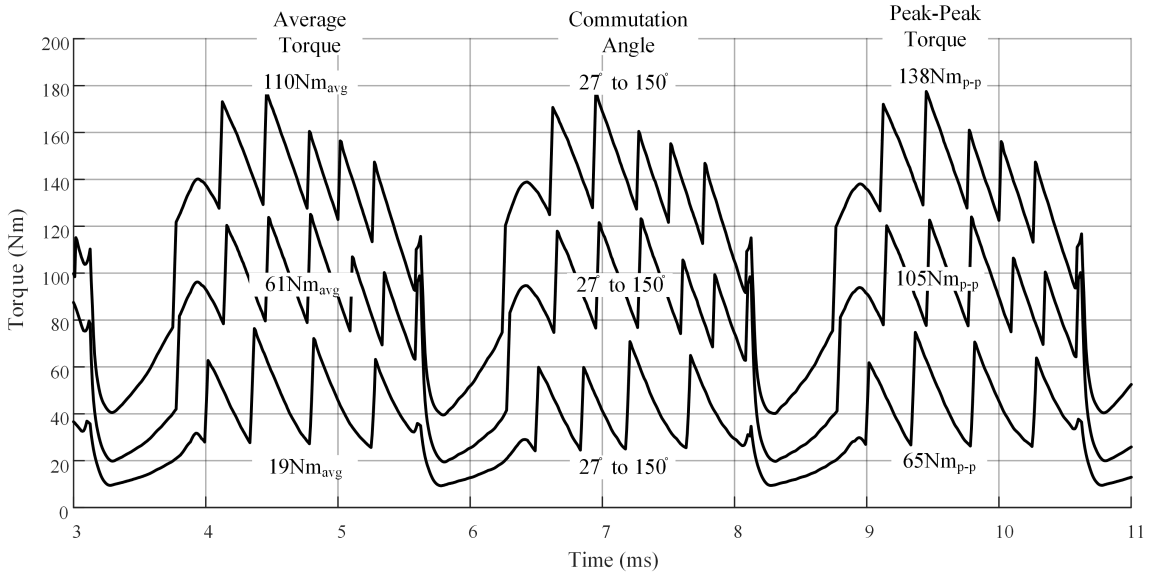

(a)

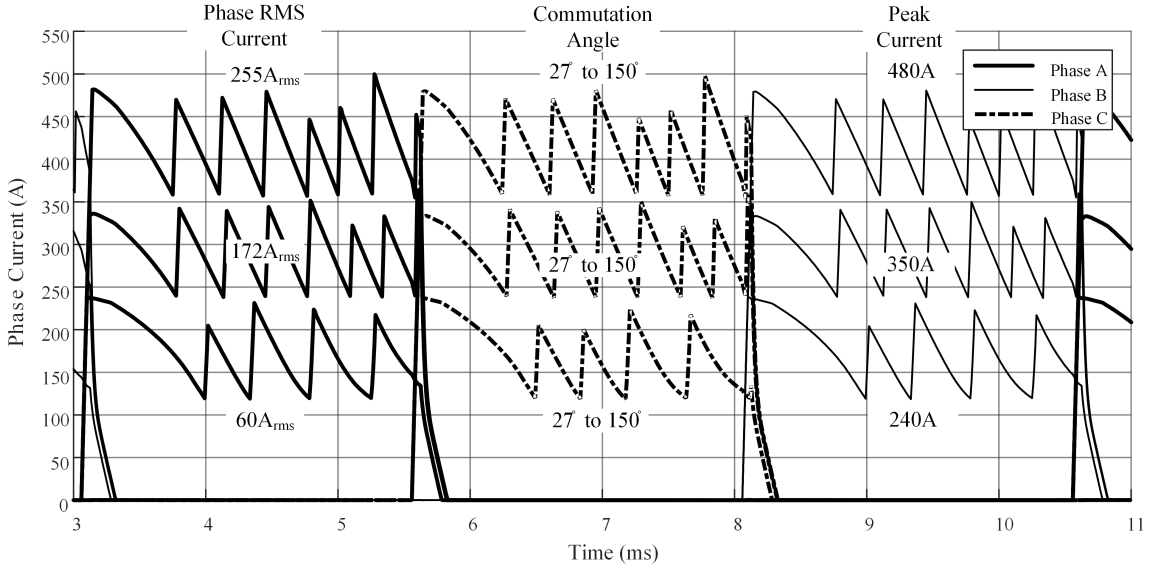

(b)

Figure 4.10: (a) Torque and (b) current at 1,000rpm. Sample frequency is 120kHz.

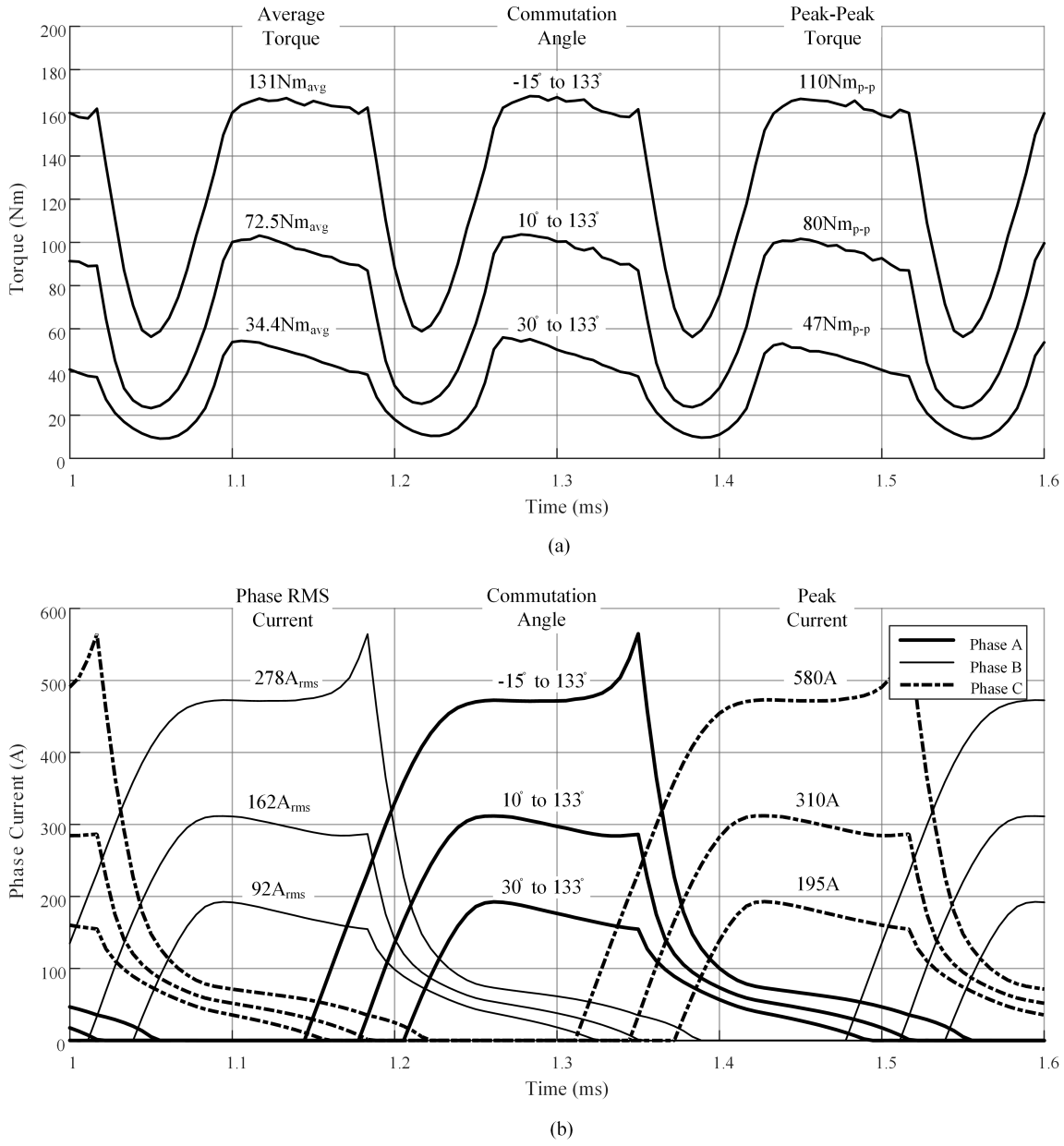

Figure 4.11: (a) Torque and (b) current profiles at 15,000rpm.

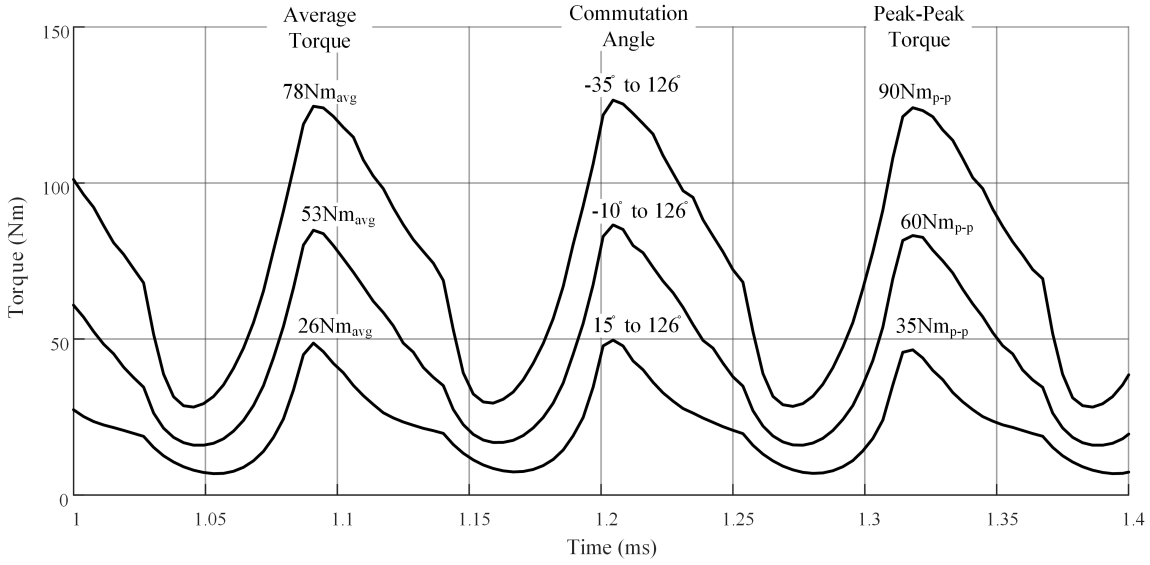

(a)

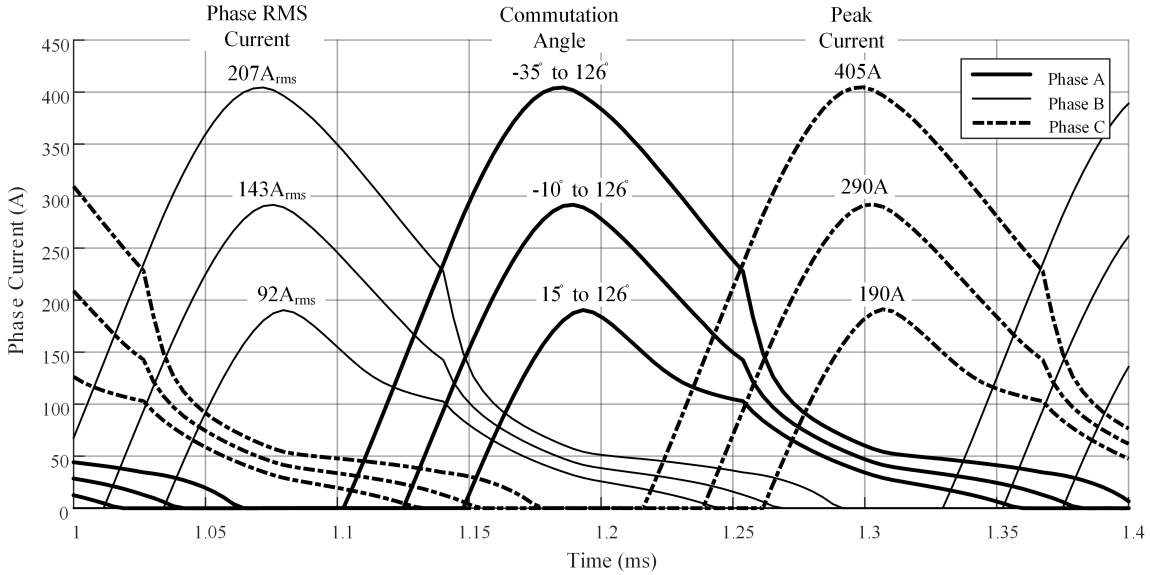

(b)

Figure 4.12: (a) Torque and (b) current profiles at 22,000 rpm.

The performance information determined from the optimization function by Peng [125] showed that the maximum torque meets and potentially exceeds the project requirement of 150kW. The power circuit utilizes an Infineon FF600 phase leg, a 1200V 600A rated device. The power devices have been derated to 480A to minimize risk of overload damage. The optimization function shows this magnetic design can deliver at or above 150kW, while staying within the 480A peak current limit anticipated by the drive hardware. Using the optimizer to find maximum torque, shows the maximum machine torque can reach up to 211kW, if the switching devices are upgraded to the Infineon FF900, A 1200V 900A rated device, which has the same footprint.

If desired, the motor could be optimized for absolute maximum torque to be 150kW at 22,000rpm in one of three ways. First, the number of turns could be increased, which would directly reduce current and hence torque in single pulse mode. Additionally, the base speed will decrease, which will also shift the precise speed and torque at which maximum motor efficiency will occur. Second, is reduce the stack length. Since torque is generally proportional to stack length, a basic proportionality relationship can be used to determine the exact stack length necessary to produce the desired power output

$$\frac{P_{calculated}}{P_{specification}} = \frac{Stack_{calculated}}{Stack_{new}} \tag{4.3}$$

Solving the proportional relationship shows that 150kW can be produced at 71% of the maximized stack length, which in this case was found to be 100mm in Section 3.4. It can be reasonably assumed that with an additional magnetic design iteration with stack length at 71mm, output power would be precisely 150kW, albeit at higher current density.

Lastly, if absolute maximum power is desired to be exactly 150kW as opposed to 211kW, this indicates that a steel with lower yield strength could be used instead of the selected 0.27mm 440MPa steel, and still meet the specification requirements. Of course,

using a steel of lower yield strength requires going through the centrifugal force and rotordynamic optimization procedure again; however, this would likely result in more steel availability which would increase options for reduced cost and enhanced electro-magnetic characteristics.

4.2.3 Excitation Torque Ripple

In Figure 4.13, per unit torque ripple can be seen to range between 1 and 3.5 times the average torque of the machine. At low speed, rate of change of flux-linkage enables current to rise quickly. Machine controllability at low speed is highly dependent on the switching frequency of the power devices. In this case, the power devices selected for the motor drive are large in both current and voltage rating. The expected response for such devices was anticipated to be 5kHz switching frequency or lower. With this expected frequency and at low rotational velocities, current can rise quite rapidly resulting in high current and hence torque ripple. Towards the maximum rated speed, the rate of change of flux-linkage is much greater than the DC link voltage. Here, fully developed single pulse waveforms exist resulting in large torque ripples. Around base speed, the rate of change of flux-linkage is about equal to the DC link voltage. The rate of change of current is slower and more readily controlled by the power devices.

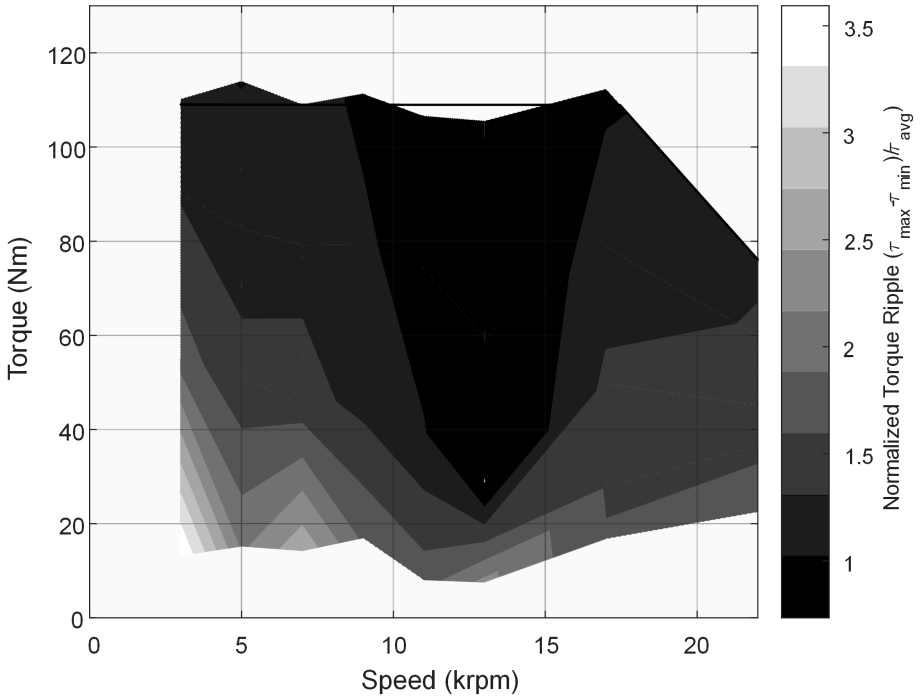

Figure 4.13: Torque ripple map for the presented conduction angles.

4.3 Magnetic Loss Analysis

As surface speed and hence electrical frequency of a machine increases, a number of loss effects become significant such as eddy currents in both the rotor and stator soft magnetic cores and the winding conductors, in addition to windage and frictional losses. In order to make accurate thermal performance conclusions, the magnitude and distribution of these losses must be well understood. In this section, windage loss, iron and winding loss maps, and loss distribution details of the proposed SRM will be investigated.

4.3.1 Effect of Bolts on the Magnetic Flux Distribution

In Chapter 3, bolts are shown to go through the rotor laminations in effort to help minimize mechanical stress on the laminations. These bolts are magnetically permeable and electrically conductive and are exposed to the oscillating magnetic field in the machine. In order for this mechanical design to be effective, the magnetic impact of induced eddy currents circulating in the bolts has to be small. A number of simulations were carried out to show that the effect of the bolts was minimal. The simulations were done in FEA, using methods similar to induction machine analysis, i.e. the bolts were modeled as a squirrel cage like structure.

Table 4.2: Loss comparison of mechanical fasteners: electrically isolated bolts versus unisolated, or connected bolts.

	Iron Losses (W)			**Bolt Joule Loss (W)**	
	Iron Bolts Connected	Iron Bolts Isolated	Air Bolts	Induced Losses Connected	Induced Losses Isolated
Stator	3070	2872	2870	0	0
Rotor	1886	1554	1574	2.5	0
Total	4956	4426	4444	2.5	0

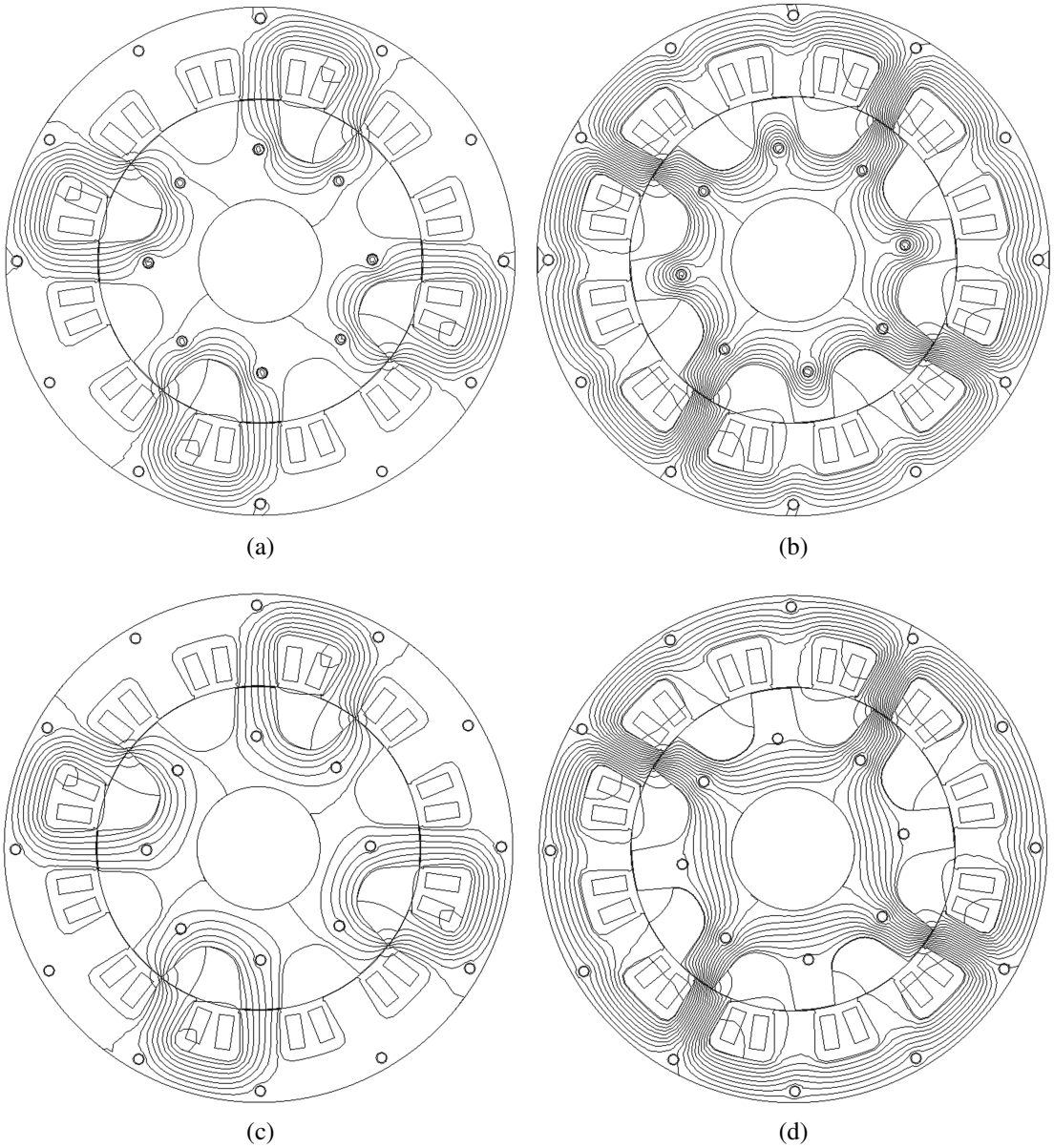

Figure 4.14: Flux lines with bolts electrically connected like a squirrel cage (a) short flux path (b) long flux path. Flux lines with electrically isolated bolt heads are shown in (c) short flux path (d) long flux path.

Figure 4.14 illustrates the flux distributions around the isolated and non-isolated bolts modeled as squirrel cage bars. Currents and resulting magnetic fields are created in the bolt regions, whereas for the case with isolated bolts, Fig. 4.14c and 4.14d, the main machine flux paths are unaffected by the bolts. Note, the stator bolts are similarly modeled, as can be inferred from Fig. 4.14.

The electrically isolated flux distribution yields almost exactly the same simulation results as when the conductivity and permeability of the bolts are set to the properties of air. This conclusion is corroborated by the loss analysis results presented in Table 4.2. Here, the losses from the isolated bolts and the control case match. The un-isolated bolts result in an additional 500W to the stator and rotor core losses due to the changed flux paths and the flux concentrations, as observed from Fig. 4.14.

4.3.2 Iron Losses

Iron loss is a function of hysteresis, eddy current, and residual losses. A number of researchers have attempted to develop analytical methods for loss computation based on non-sinusoidal flux distributions [127–129]; however, a commercial FEA based approach was taken in this work. Here, JMAG electromagnetic simulation software was used. JMAG uses a modified version of the Steinmetz equation to compute iron losses [130].

Iron loss for the rotor and stator are shown in Figures 4.15 and 4.16. The effect of frequency and flux density can be seen in the contours, as the losses increase with speed and load torque.

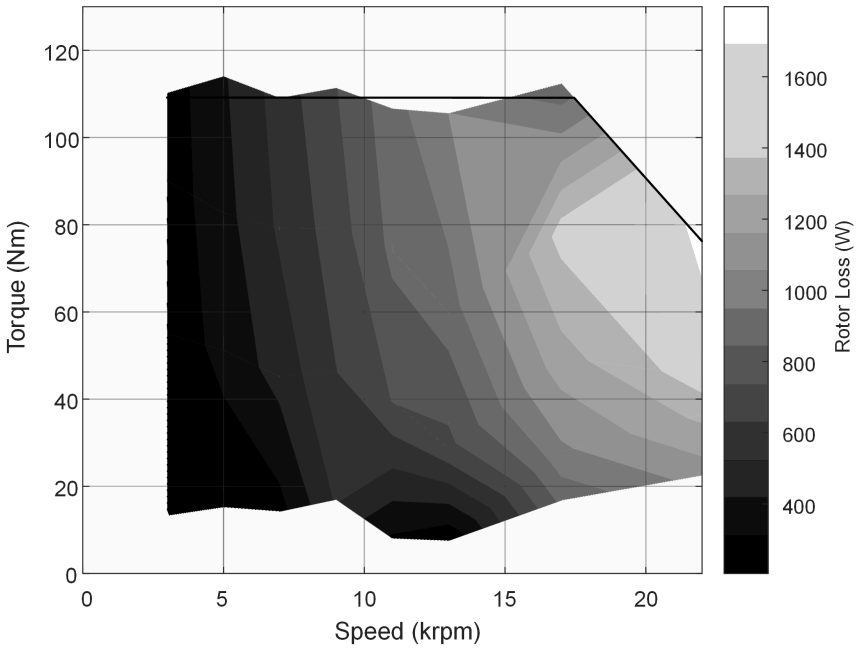

Figure 4.15: Speed and load dependent rotor iron loss.

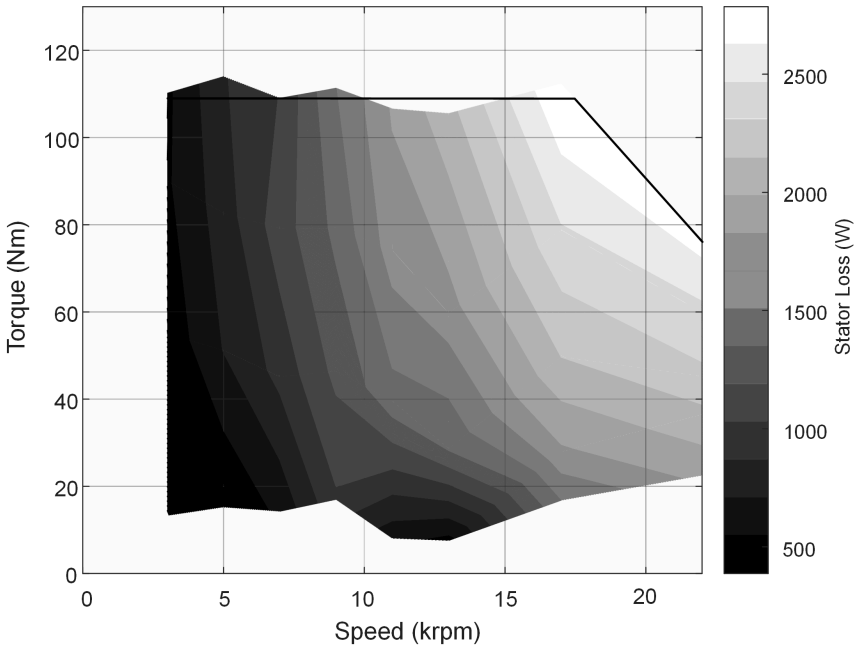

Figure 4.16: Speed and load dependent stator iron loss.

Coupled thermal and magnetic analysis was not available; therefore, knowledge of the iron loss distribution is critical for accurate thermal modeling. The loss distribution at maximum speed and power is shown in Fig. 4.18. In Table 4.3, a breakdown of the losses is presented. The losses are considered as lumped into three areas, namely the teeth, the teeth tips, and the backiron, illustrated in Fig. 4.17. Table 4.3 lists three parameters to characterize the loss density which is the percentage loss of the rotor or stator. An example interpretation of Table 4.3 is as follows, "Area D", represents the total area for the rotor teeth. For this machine, the rotor teeth account for 40% of the total rotor area, and yet 50% of the total rotor losses occur on the teeth. The rotor tooth loss density is therefore an estimated 1.25 times an ideally uniform loss distribution. According to Table 4.3, core loss at the airgap is 3-5 times greater than any other region on the core. This number does not included windage friction losses, which would further increase airgap loss density.

Table 4.3: Iron loss distribution for the rotor and stator

	Stator				**Rotor**			
	area	% loss	% area	$\frac{\%loss}{\%area}$	area	% loss	% area	$\frac{\%loss}{\%area}$
Backiron	A	65%	70%	0.93	D	50%	60%	0.83
Tooth	B	35%	30%	1.17	C	50%	40%	1.25
Tooth Tip	F	5%	1.5%	3.33	E	10%	1.7%	5.88

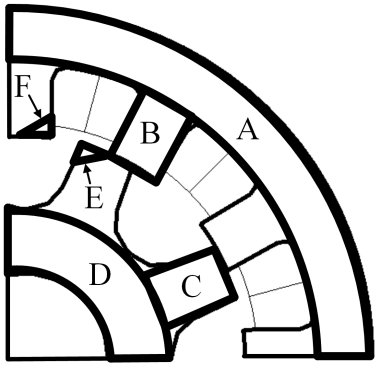

Figure 4.17: Regions described in Table 4.3 used to describe loss density.

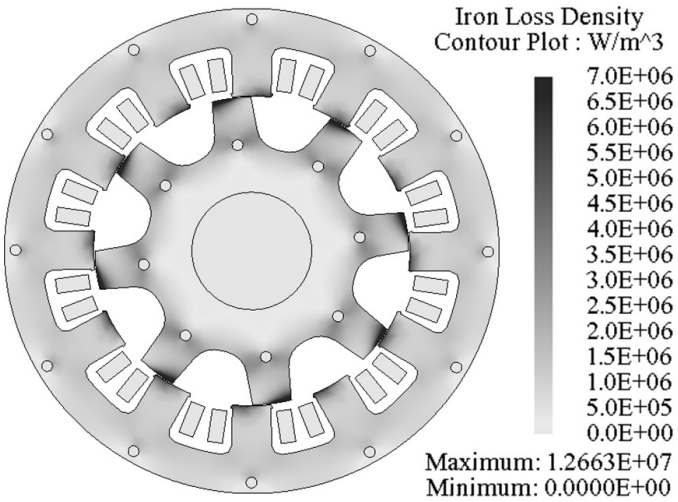

Figure 4.18: Time averaged iron loss distribution at 22,000rpm and 150kW.

4.3.3 Winding Losses

High frequency machines dictate the analysis of eddy currents losses in the conductors of machine windings. Ferreira and Richter [88] accepted some high frequency loss since they used liquid cooled hollow conductors as windings.

In work by Carstensen [97], winding losses in switched reluctance machines can be significantly reduced by using thin, high aspect ratio (i.e. length to width) rectangular conductors. According to Carstensen, windings of high density rectangular conductors deep in the stator slot reduces AC resistance and hence improves current density distribution reducing localized heating. This general conclusion is supported in work presented by Zhang in [126].

Ferreira and Richter's hollow conductor design, while thermally effective, maximizes conductor exposure to stray fluxes increasing eddy currents and local losses. Not only does this result in lower machine efficiency, but a larger auxiliary cooling components such as pump and radiator would be necessary in a traction application, further reducing overall system efficiency due to the included auxiliary component losses.

One downside to rectangular windings is that coil manufacturing is more challenging. On the other hand, switched reluctance machines can take full advantage of externally formed windings that are then slipped over the stator teeth. In this chapter, high aspect ratio rectangular conductors were sourced and simulated. While externally formed round conductors are still easier to manufacture than rectangular, rectangular conductors show potential for significant reduction in AC resistance [97].

Figure 4.19 shows the rotor position at the instant the winding loss density is greatest at the maximum speed of 22,000rpm and load of 150kW load. The rectangular conductor geometry is 0.04x.204 inches equating to 5.264mm^2; approximately equivalent in area to a 10AWG round conductor. In this simulation, winding losses show a reduction on the

order of +50% compared to round conductors, a result of AC resistance minimization. The RMS current was approximately 42 amps. Assuming no AC influences, and homogeneous current distribution, the DC current density is approximately $8\frac{A}{mm^2}$ Investigating the impact of AC resistance, the total loss for the rectangular conductors is 3.4kW averaged over one period. The time averaged current density in the most dense conductor is around $20 - 23\frac{A}{mm^2}$, with peak instantaneous loss density is around $190\frac{A}{mm^2}$. High density packing factor provides plenty of space for slot liquid cooling to help cool localized losses.

Since computing AC losses is computationally expensive, DC resistive loss computations were used to create a winding loss map. The losses of the eddy current analysis were used to find an equivalent DC winding resistance with which to run quicker simulations. These simulation results are represented in the winding loss map in Figure 4.20.

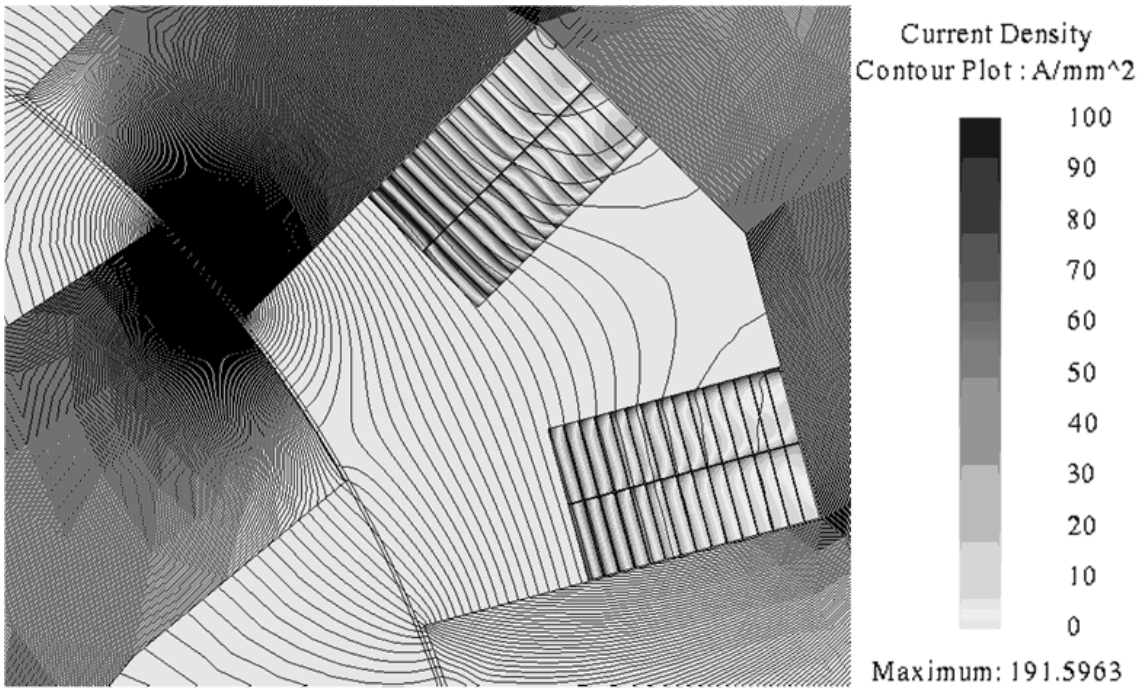

Figure 4.19: Lines of equal magnetic vector potential (Flux lines) and current density plot showing current density distribution inside the SRM winding.

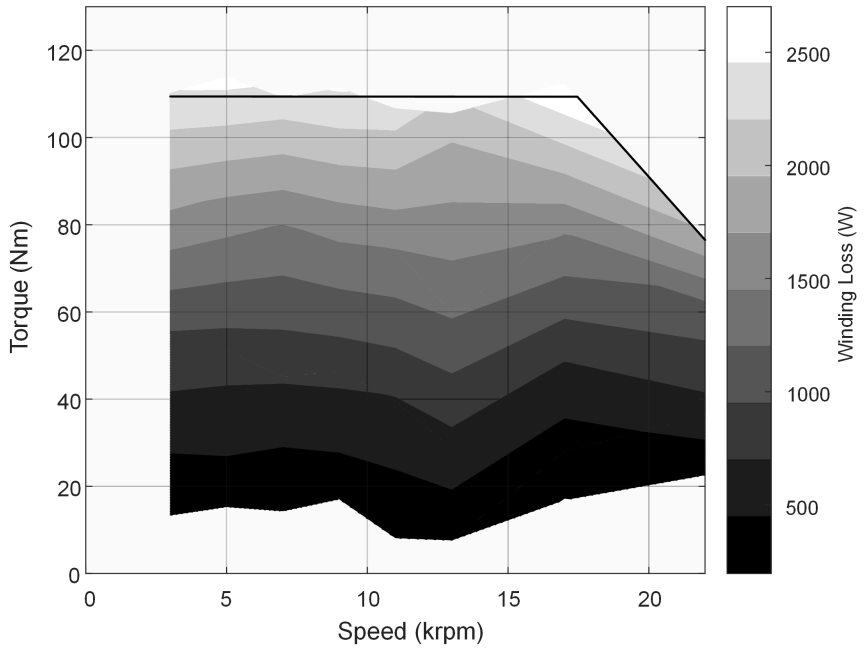

Figure 4.20: DC winding loss distribution as a function of speed and torque

4.4 Magnetic Efficiency Map

Summarizing the transient results, losses from Figs. 4.15, 4.16, and 4.20 were used to create the efficiency map in Figure 4.21. Maximum magnetic efficiency is in excess of 96%. Base speed is in the range of 15-17,000rpm. With the considered IGBTs, maximum torque is approximately 110Nm.

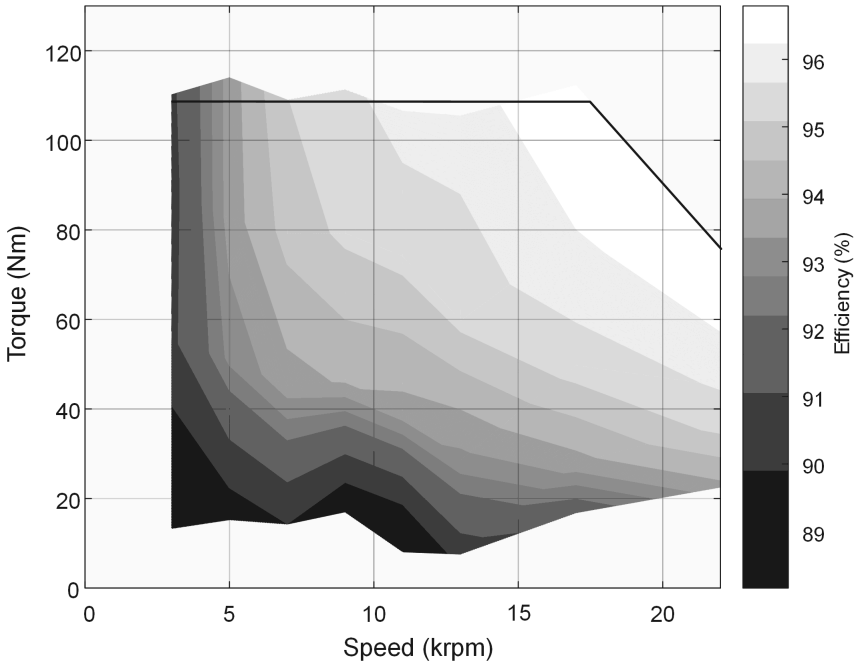

Figure 4.21: Magnetic efficiency map for the proposed conduction angles.

4.5 Conclusions

In this chapter a stator was developed around the rotor which was established from analysis in Chapter 3. A simple conduction angle control strategy was considered such that a comprehensive magnetic analysis was performed on the machine design. It was found that parasitic losses are created in the rotor with the bolted assembly method presented. Electrically isolating the bolts reduces losses by 500W, approximately equivalent to having no bolts at all.

Current and torque waveforms at startup and rated speed are shown and are within conductor current carrying capacity. Base speed was found to be around 15,000rpm. The motor is magnetically and structurally capable of reaching 211kW at 22,000rpm. Machine efficiency is found to be best in single pulse mode, reaching an estimated 97% magnetic efficiency between 16,000 and 22,000rpm. Losses and loss distribution were also considered in both the core and the windings. An eddy current analysis was performed on the windings. Current density was found to be high, between 8 and an estimated $23\frac{A}{mm^2}$, which by industry rules of thumb, necessitates liquid cooling. Core loss and torque ripple was determined over the entire torque-speed envelope. Core loss distribution at 22,000rpm and 150kW load was also investigated for use in thermal analysis. Loss density was found to be non-uniform and highly concentrated near the airgap in the windings, rotor and stator core.

The contributions of this chapter are as follows:

- First, it was shown that this SRM is controllable with linearized conduction angles at startup, low speed, base speed and in the single pulse region. Existing literature was not entirely clear if this was possible for this motor using a primitive drive design and controller. Certainly, a more advanced drive design which offered higher switching frequency or multiple voltage states and a controller utilizing nonlinear conduction

angles could be developed; however, this makes initial implementation of a machine such as this much more challenging and was not considered in the scope of this work.

- The second contribution is with respect to the intended automotive application. Existing literature focuses on the machine performance at the rated speed and torque. In the auto industry where drive cycle analysis is extensively conducted, rated speed and torque performance is insufficient. Consequently, speed, torque, torque ripple, efficiency, losses and loss distribution information across the entire operating envelope has been collected and presented. This information can be used as a baseline not only to estimate vehicle performance and energy consumption over a drive cycle, but also temperature profiles, and driveline torsional dynamics.

While machine parameters such as torque ripple and efficiency can undoubtedly be improved with further drive and control refinement, Chapter 4 represents what a basic linearized conduction angle control algorithm would perform like, and serves as a reference for how future improvements might be made to such a motor and drive system.

Chapter 5

Maximizing Thermal Effectiveness and Minimizing Parasitic Loss in a Liquid Cooled Switched Reluctance Machine

5.1 Effective System-Level Cooling

It has been discussed in previous Chapters that improving energy conversion efficiency is a key motivator for future powertrain designs, as influenced by the following items, for which an understanding of all loss elements is a fundamental requirement:

1. Reducing powertrain mass
2. Designing high efficiency powertrain architectures
3. Designing high efficiency powertrain components
4. Reducing parasitic loads
5. Reducing auxiliary loads

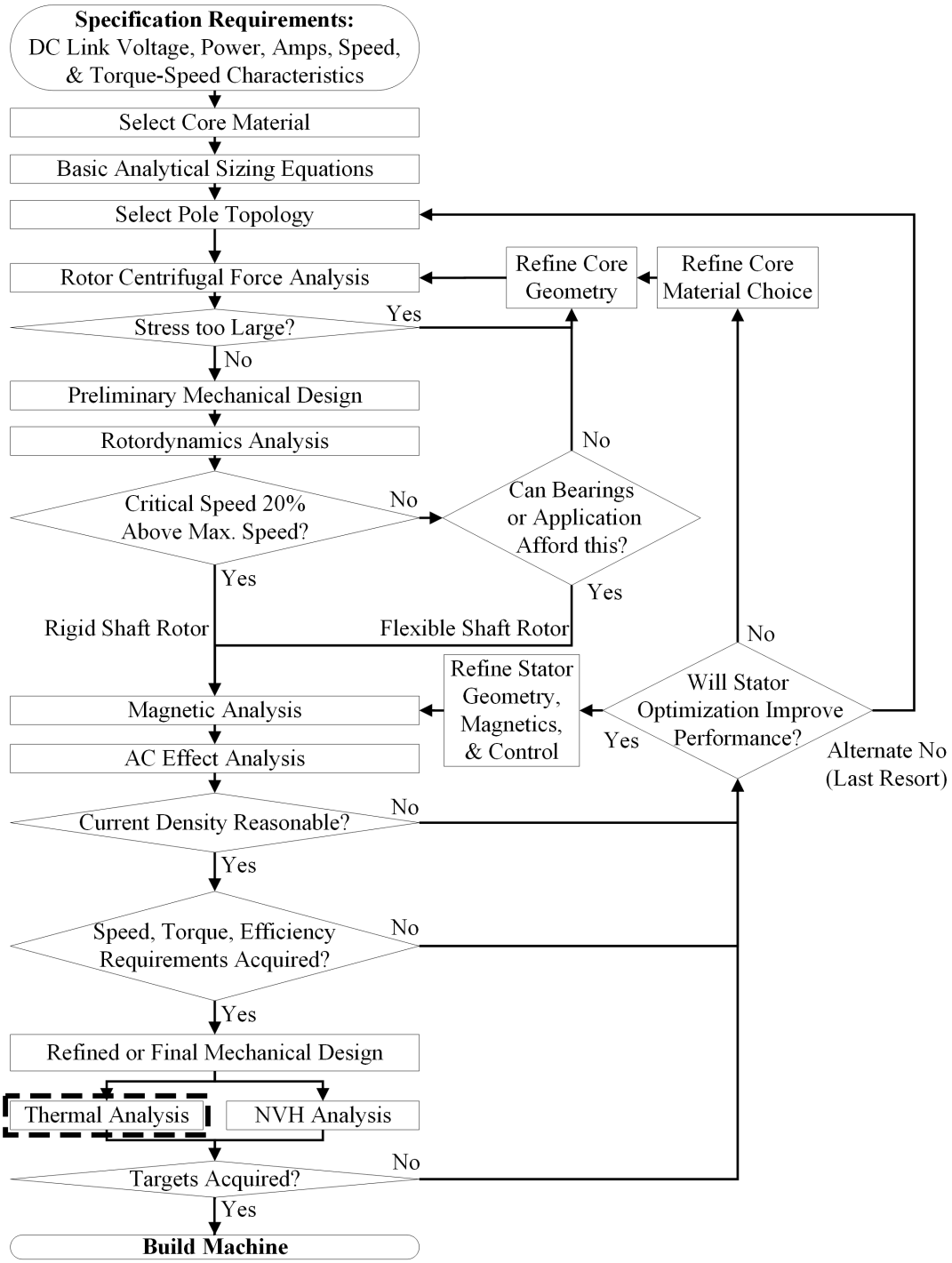

Figure 5.1: Proposed design flow for SRMs with high surface speed. The boxed region identifies the thermal design procedure applied to this machine

Due to the conflicting nature of the design items, a strategy is presented in this Chapter that addresses all options while maintaining the context of the design flow in Figure 5.1. First, an advanced prototype machine design is considered which aims to address design items 1-3, i.e. the 22,000rpm, 150kW switched reluctance machine (SRM) described previously in Chapter 3 and 4. The motor is a 22,000RPM 150kW switched reluctance machine. High rotational velocity was considered to directly address powertrain mass as highlighted by design item 1, but also to identify challenges and solutions associated with items 2 and 3.

While high speed operation can be an effective solution to reduce machine mass, high speed operation does not come without compromises. One such compromise being the necessity for more aggressive cooling systems. Thermal challenges are important to identify and address due to their broad implications which affect both motor and powertrain system design. From a machine design perspective, thermal management impacts on reliability, winding resistivity and hence machine size and short time overload capability. Efficiency is also impacted if parasitic loads, or losses, are created by an increasingly complicated thermal management system. One example of a parasitic load, powertrain design item 4, would be a canned pump motor such as those presented by Laudensack et al [29]. Often implemented to stop corrosion, electrically conductive 'cans' generate eddy current losses due to exposure to harmonic magnetic fields. For powertrain system designers, heat generation influences the size of auxiliary components, powertrain design item 5, such as pumps, radiators and fans, as depicted by the vehicle cooling schematic of Fig. 5.2

This Chapter addresses the thermal systems necessary for the described power plant, while minimizing parasitic loads and auxiliary support systems which would exist in an automotive environment. To achieve these goals, a cooling jacket is presented in Section 5.2. Due to the small airgap nature of SRM's, canned-stator oil-submerged cooling

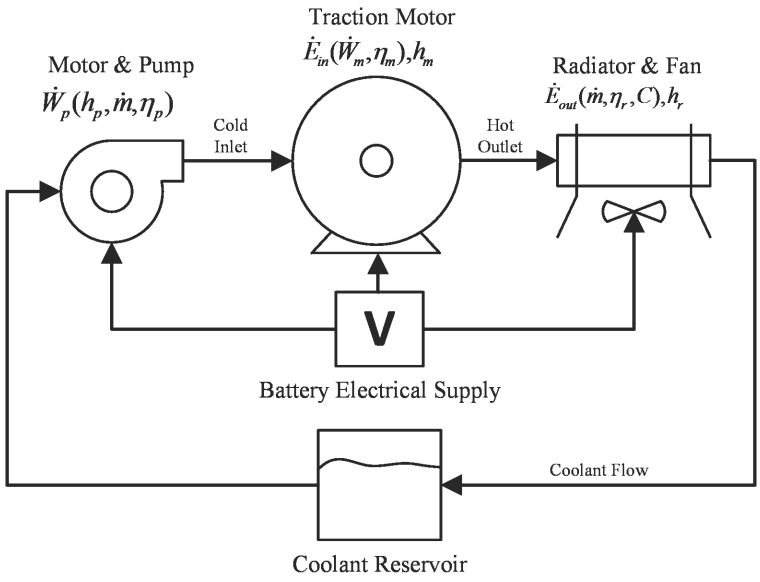

Figure 5.2: Electrified vehicle propulsion with liquid cooling system.

designs such as the permanent magnet (PM) rotor design presented by Xu et al. [131] are difficult to implement for SRM's due to the much higher magnetic field variations at the rotor surface and the additional airgap required to accommodate such a can. This additional airgap is not as significant for PM rotor technologies since the reduced rotor field due to the increased magnetic airgap can be countered by an increase of the PM length in the direction of the magnetization. For the SRM, an increase in airgap radial length is directly related to increased stator MMF, i.e. winding current. While potentially very effective, direct oil cooled systems were also not considered due to concern regarding the large rotor peripheral speed and uncertainty around insulation degradation resulting from thermal shock, erosion and coolant contamination. Consequently, two liquid-cooled parasitic loss-less systems which address winding energy generation are presented in Section 5.3, while Section 5.4 concludes the study via the discussion of novel potting materials investigated to maximize heat transfer from the stator windings to the peripheral cooling systems.

5.2 Cooling Jacket

A cooling jacket is a liquid cooled housing for the stator core. For this application, helical and axial type flow cavities of aluminum construction were considered for the cooling jacket. A dual-flute counterflow cooling jacket was ultimately selected due to high thermal efficiency, low pressure drop and uniform temperature distribution.

Fig. 5.3a shows the steady state temperature gradient at 5 gallons per minute (19lpm) per inlet. Thermal analysis results show that temperature is uniformly distributed across the inner periphery where the core is located. There is little temperature variation between the inlet and outlet ports. Fig. 5.3b shows the flow ports and flow velocity, which maintained a mostly constant 2.2m/s. No flow reversal or flow separation was discovered beyond the inlet and outlets, which is critical for maintaining uniform temperature distribution as well as minimizing coolant pump size. Fig. 5.3c is a half scale model of the cooling chamber prototyped to examine the various manufacturing methods.

Manufacturing the dual-flute geometry is straightforward with 5-axis CNC milling machines. However, a rather laborious multi-step manufacturing process is required for the 300mm diameter jacket. Fig. 5.4 describes the manufacturing details for the cooling jacket. A seamless extruded aluminum tube is welded to the outside of the machined jacket along with inlet and outlet ports. Final machining operations are needed along the inside of the jacket to remove any thermal deformation from the welding process, as well as create necessary fastening features, such as bolt holes, shoulders, etc.

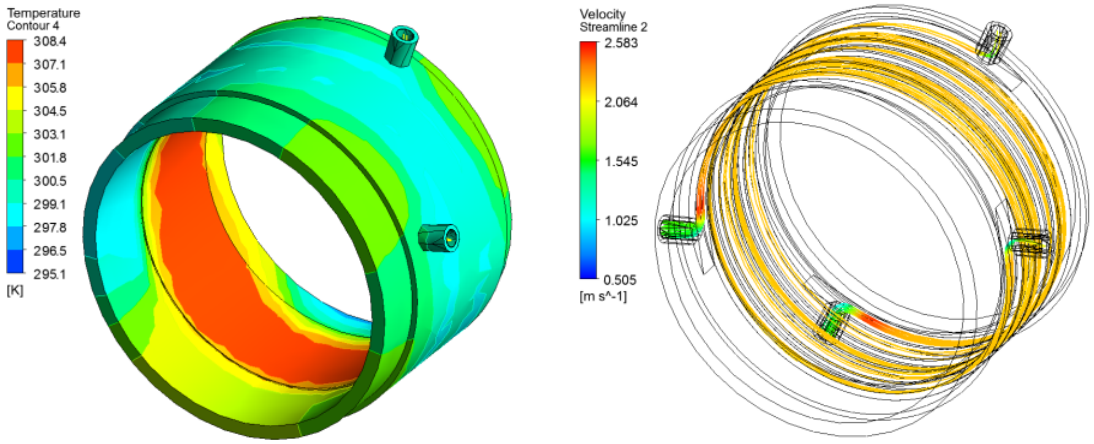

(a) (b)

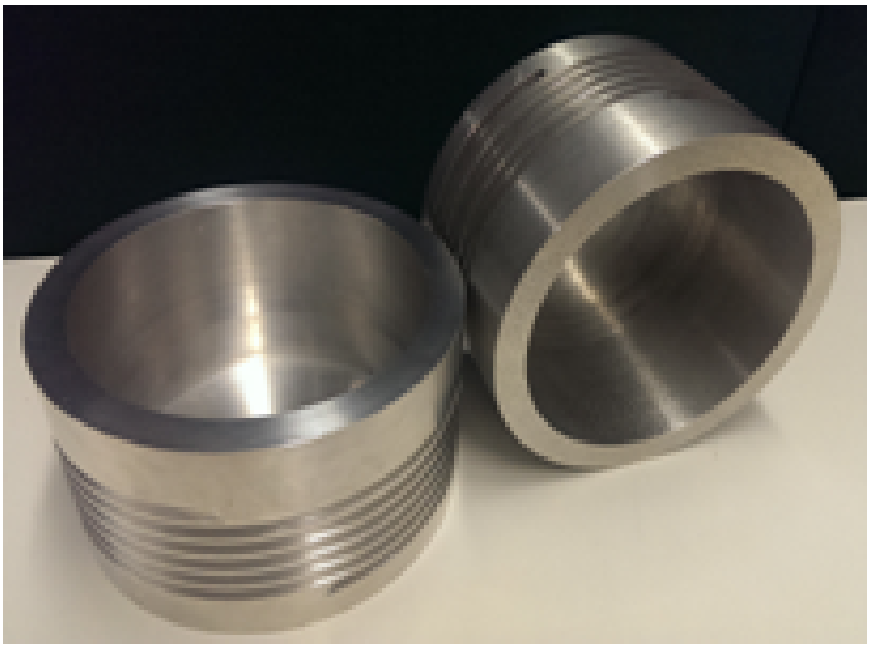

(c)

Figure 5.3: (a) Temperature distribution of the dual flute cooling jacket under constant heat load (b) streamline flow velocity distribution inside cooling channels (c) 1/2 scale test manufacture of dual flute geometry.

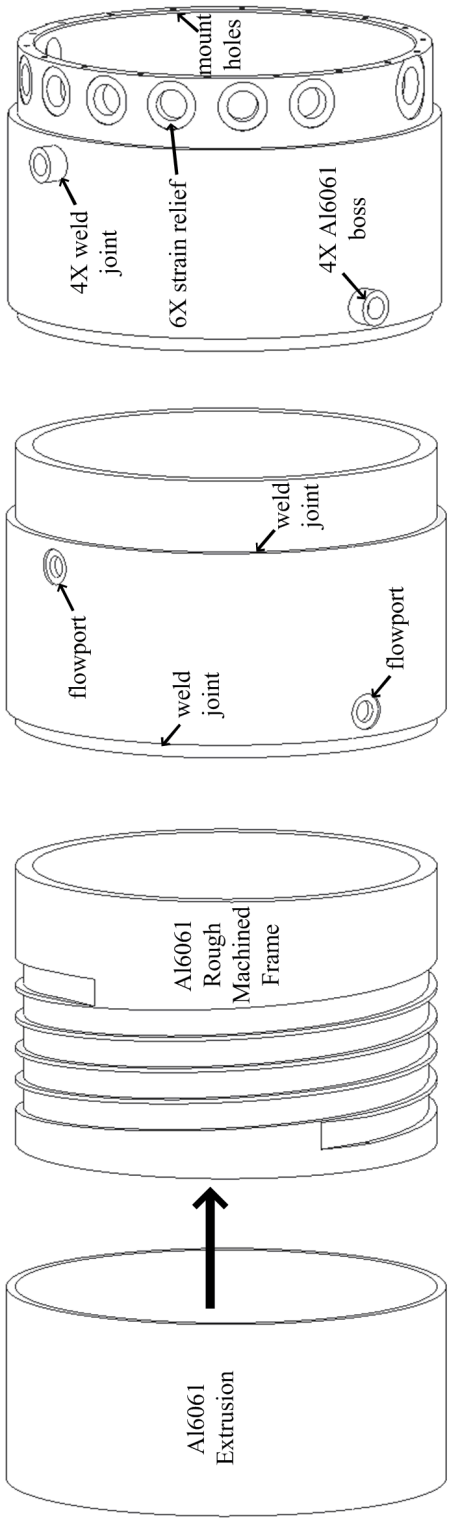

Step 1: Shrink fit extrusion onto machined frame

Step 2: Weld joints of extrusion and frame

Step 3: Spotface and drill flowports on jacket

Step 4: Weld bosses to jacket

Step 5: Finish machine jacket

Figure 5.4: Dual flute cooling jacket manufacturing procedure.

5.3 Polymer Channels for Inter-Slot Cooling

From the studies of Chapter 3 it was concluded that to realize an electro-magnetic design with mechanically feasible volumetric constraints, operation at high electric loading would be required, as discussed in Chapter 4. Thus, to address the resulting high loss density in the soft magnetic core and stator windings, inter-slot liquid cooling tubes were considered. The stator winding produce alternating current (AC) effects with a fundamental frequency of up to 3.6kHz. At such frequencies and saturation levels characteristic of switched reluctance machines at high magnetic loading, these alternating currents would induce high frequency eddy currents in any conducting or permeable materials within the slot including the windings themselves. Such inductions would come from stator slot leakage, fringing fluxes between the rotor and stator; and proximity to conductors including the windings. Some researchers have attempted to put tubes in the stator slot for cooling; however, material is unspecified and authors allude to loss optimization procedures [1]. Ferreira et al. [88], use hollow tubular winding conductors for cooling, a common practice with large (500MW) turbo-generators, but more difficult on smaller machine sections. In this case, the tubular conductors increase conductor height and are thus exposed to stray flux, increasing winding losses. In both situations, the thermal management system adds some parasitic loss to the machine which can be particularly severe in high frequency environments and ultimately has to be managed.

The impact of eddy currents on metallic tubes in a stator slot were simulated and shown in Fig. 5.5, where the vectors represent current magnitude. The metallic tubes are assumed to be copper. From Fig. 5.5, current vectors are greatest in the cooling tubes, not the windings. Simulations show that the copper cooling tubes are estimated to add approximately an additional 4kW to the total machine losses. Assuming that the tubes are made of stainless steel, approximately 1.5kW of additional loss is added, roughly 1% of

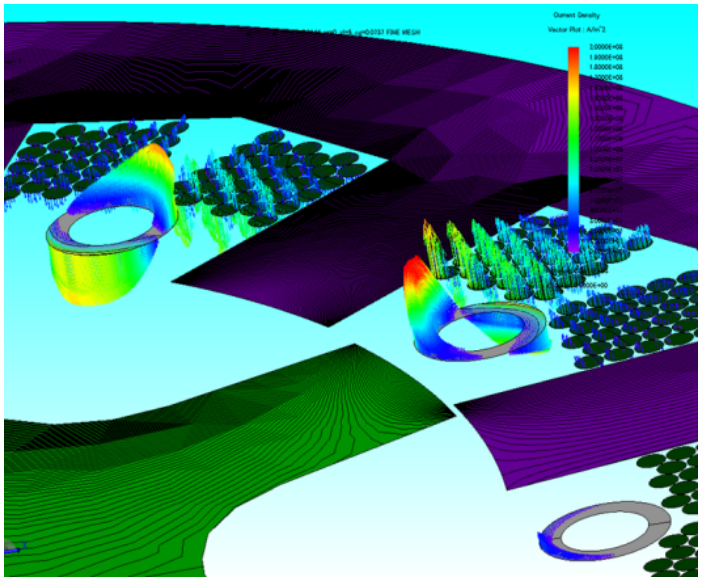

Figure 5.5: Current distribution in a stator slot exposed to strong magnetic fields from leakage and fringe flux. Long red vectors represent high current, whereas short blue or purple vectors represent small current.

the machine's total expected power. Loss variation is simply due to material conductivity as the stainless steel tubes are assumed to be non-magnetic. Table 5.1 lists a number of suitable tube materials and their electrical conductivities, highlighting that copper allows the highest currents and stainless steel the least. Teflon, a polymer with extremely low conductivity, would have the lowest (effectively zero) eddy currents, and hence loss distribution.

Table 5.1: Common Materials and their Electrical Conductivity

Material	**Electrical Conductivity (S/m)**	Ref.
Copper	5.96×10^{7}	[132]
Stainless Steel	1.4×10^{6}	[133]
Air	7.83×10^{-15}	[134]
Teflon (polymer)	$<10^{-16}$	[135]

For the presented high frequency motor application, a commercial polymer material was selected as a candidate for cooling channel construction. CoolPoly E5101 is a Polyphenylene Sulfide composite that has an experimentally verified thermal conductivity between 2-2.7 W/m·K in the working temperature range of the machine considered, i.e. 25°C to 180°C. A small electrical conductivity allows this composite to be placed in an area with high strength alternating magnetic fields without reducing its thermal benefit, while modest, is substantial in comparison to Teflon.

5.3.1 Slot Cooling

Eddy current generation strongly influences slot component orientation. Cooling tubes wedged between the conductors in the slot may at first seem highly thermally effective; however, Zhang and Carstensen [97, 126] suggest that highly compact windings located deep in the stator slot, i.e. near the backiron, minimizes eddy current generation in the

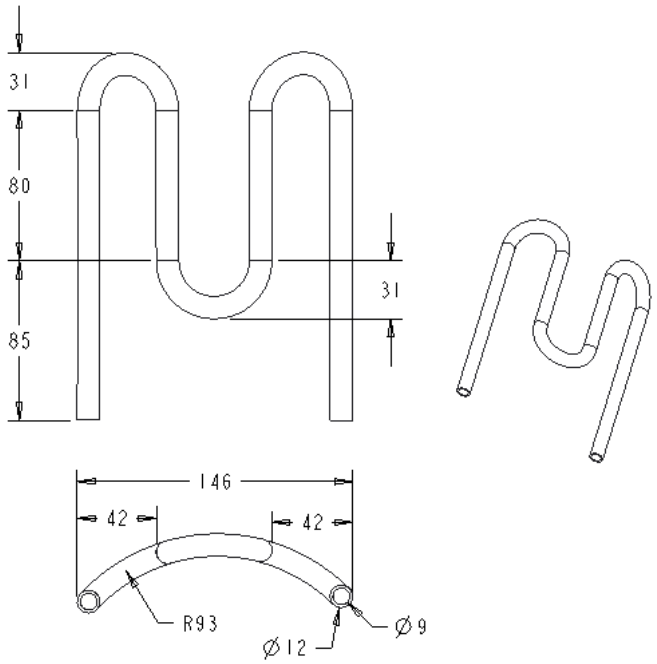

Figure 5.6: Slot cooling tube geometry created by lost-core injection molding processes.

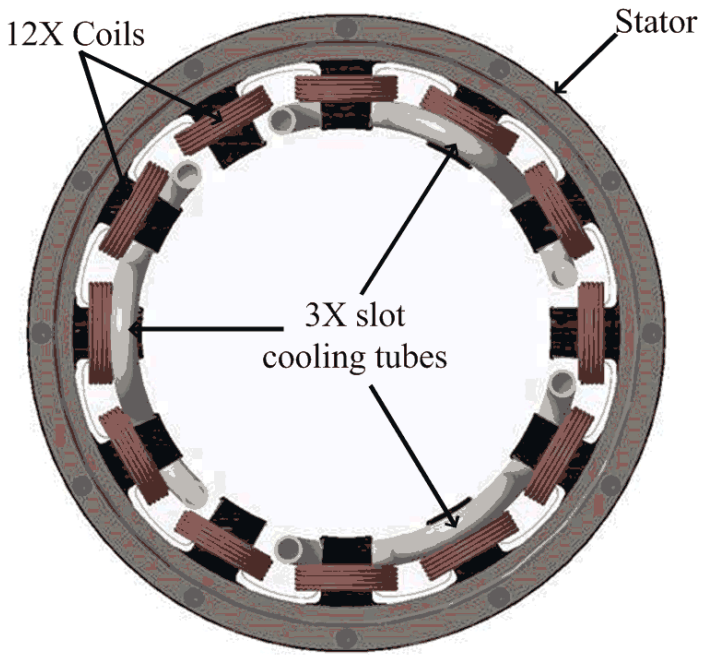

Figure 5.7: Slot cooling tubes oriented around the stator and coils.

windings. Including cooling tubes between the stator conductors will force them closer to the airgap; therefore, increasing winding losses, hence cooling tubes placed near the airgap appears to be the best solution. Benefits therefore, of cooling close to the airgap include:

Being able to compact the windings deep in the slot, targeting all points of peak loss generation in the machine, for example, stray and leakage flux tends to concentrate winding eddy currents towards conductors nearest the airgap.

Additionally, switched reluctance machines naturally saturate at the teeth tips; therefore, iron loss densities are greatest on rotor and stator teeth tip regions.

Finally, windage losses manifest at the airgap, which according to the findings in Section 3.3.7, is non-trivial for the considered machine.

The stator and windings went through several design iterations until sufficient space existed in the stator slot to package axial cooling channels. A representation of the tube geometry is depicted in Fig. 5.6 and the assembled stator and cooling tubes in Fig. 5.7.

5.3.2 End Turn Cooling

Winding end-turn regions have been documented as high temperature regions is all electric machines due in part to the fact that there is not much air motion around the end windings, and there are no thermal conduction paths [136]. A fan like structure could be implemented on the rotor to promote air movement and increase heat transfer coefficient around the stator winding end turns; however, in the case of a high-speed motor, fan blades will be noisy. Liquid cooling is quieter, available, and will more appropriately suit the electrical loading requirements. Due to the close proximity with the windings, material requirements are similar to those necessary for stator slot cooling; however, differing geometry is required. End turn cooling channels can be injection molded into a ring shape, as illustrated in Fig. 5.8. Rings are placed touching the end windings and sandwiched the stator as indicated in Fig. 5.9.

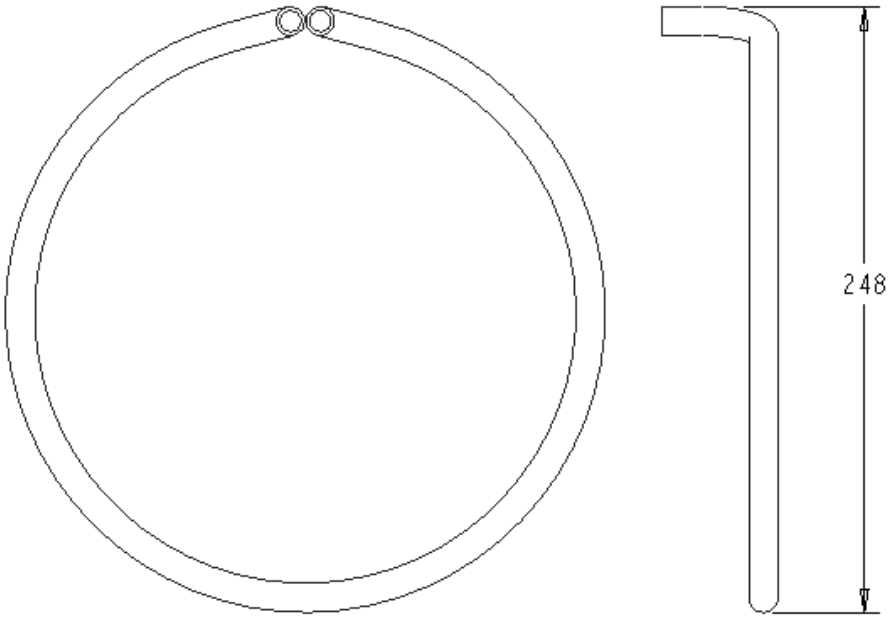

Figure 5.8: End turn cooling tube geometry created with lost-core mold injection technology.

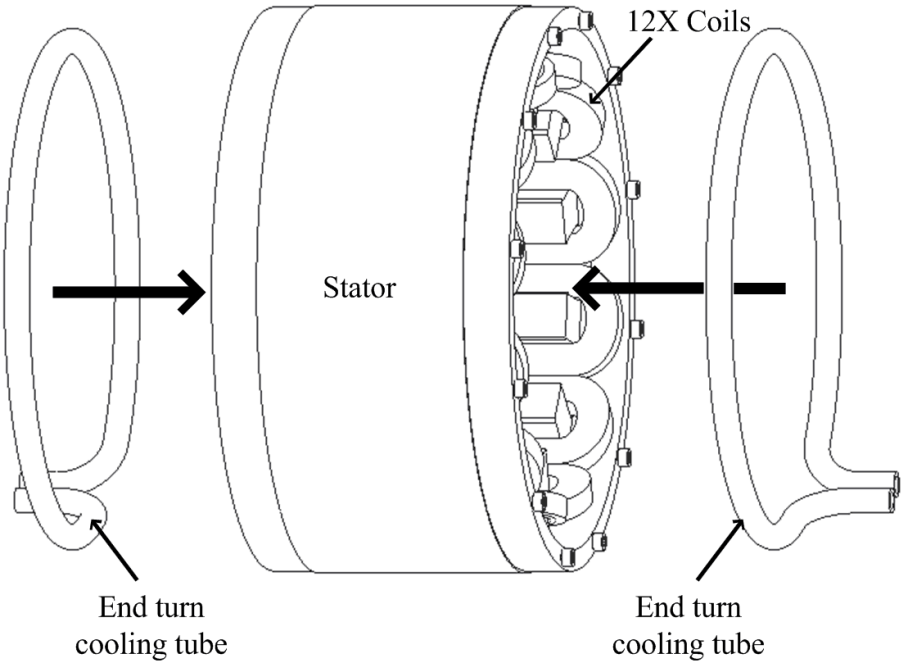

Figure 5.9: Assembly of end turn cooling tubes.

5.4 Potting Compound Development

Windings surrounded by air are limited in the number of conduction pathways for heat. Air is thermally insulating as mentioned in Table 5.1, which means potting coils with even traditional thermoplastics, having a thermal conductivity of 0.1 to 0.3 W/m·K, provides an additional thermal pathway that would not otherwise be attainable [137]. Both the active winding length and end windings can benefit from potting or encapsulation with thermally conductive polymers. Filling the stator slots or the space between the housing and end-windings creates thermal pathways to additional heat dissipation mechanisms. The material properties required for a potting compound include not only high thermal conductivity, but also properties to avoid the entrapment of air during the winding impregnation process. Nategh et al. found that a more liquid polymer (prior to setting) would allow for an easier implementation [138]. Using a commercial off the shelf induction motor, Li et al. tested

the output performance using SPEED® software. They chose Lord SC-320 as one of their encapsulation compounds, which has a thermal conductivity reported on its data sheet of 3.2 W/m·K. The end-turns were modeled as being encapsulated in epoxy between the coil and housing. This encapsulation provides a thermal path to the housing, which is important for motors with cooling jackets, and also a thermal path for internal cooling via air convection. No filler was added to the Lord SC-320 in this study [139]. Adding filler to a polymer can increase the thermal conductivity of the resultant composite; however, there is a limit of the volume percent that can be added before the composite no longer can be potted.

5.4.1 Doping

Doping of the polymer compound by two differing base epoxy compounds was analyzed:

1. Resoltech HTG 200, an oxirane functional group epoxy with amine hardener
2. Elan Cast P300, a polyester resin.

Resoltech was selected for low viscosity, while Elan Cast was selected for high thermal conductivity characteristics.

The thermal and mechanical properties of a polymer can be drastically altered by mixing in various amounts of thermally conductive fillers, while maintaining low electrical conductivity. Three fillers have been identified for their thermal properties:

1. Surface Enhanced Flake Graphite
2. Hexagonal Boron Nitride
3. Aluminum Nitride

Scanning Electron Microscope (SEM) images of these fillers can be seen in figures 5.10a, 5.10b and 5.10c respectively. The high surface area of these fillers allows for better

increased thermal properties over the bulk material and good adhesion to the matrix compound.

In order to effectively remove thermal energy from the machine windings, a material must be developed to create a thermal circuit between the axial cooling channels to the windings. This cooling will be packaged within the machine stator slots, resulting in a very close proximity to the windings and thus offering a very high cooling potential. Due to the unique application of slot cooling, materials development was selected as a mechanism to produce an implementable and highly thermally conductive composite for which few commercially available alternatives exist.

Since many machine components are temperature sensitive, a low temperature implementation process, such as vacuum assisted resin infusion, is necessary. A polymer epoxy filled with a ceramic conductive filler has been chosen as the material of choice for this application due to its favorable electromagnetic, mechanical and thermal properties, as well as its ability to be vacuum infused into the machine stator. To determine the thermal properties of the polymer composites and determine feasibility of vacuum infusion, many different test samples have been created, tested and analyzed in [140].

In addition, the thermal expansion coefficient of several composite filler percentages has been analyzed to highlight any major longevity concerns. Rhebergen et al. [140] investigated Elancast under a number of filler concentrations of aluminum nitride and hexagonal boron nitride and validated the contribution of axial cooling to the performance of an SRM. This thesis continues that work, investigating the difference in choosing a polymer matrix with high initial thermal conductivity, but high viscosity (Elancast) versus a matrix with low initial thermal conductivity, but low viscosity (Resoltech). Viscosity was of major concern, not only because a lower viscosity aided in the vacuum infusion process, but also because a lower viscosity base polymer also would allow for a greater filler addition. The more filler is added, the more viscous the composite becomes. In addition,

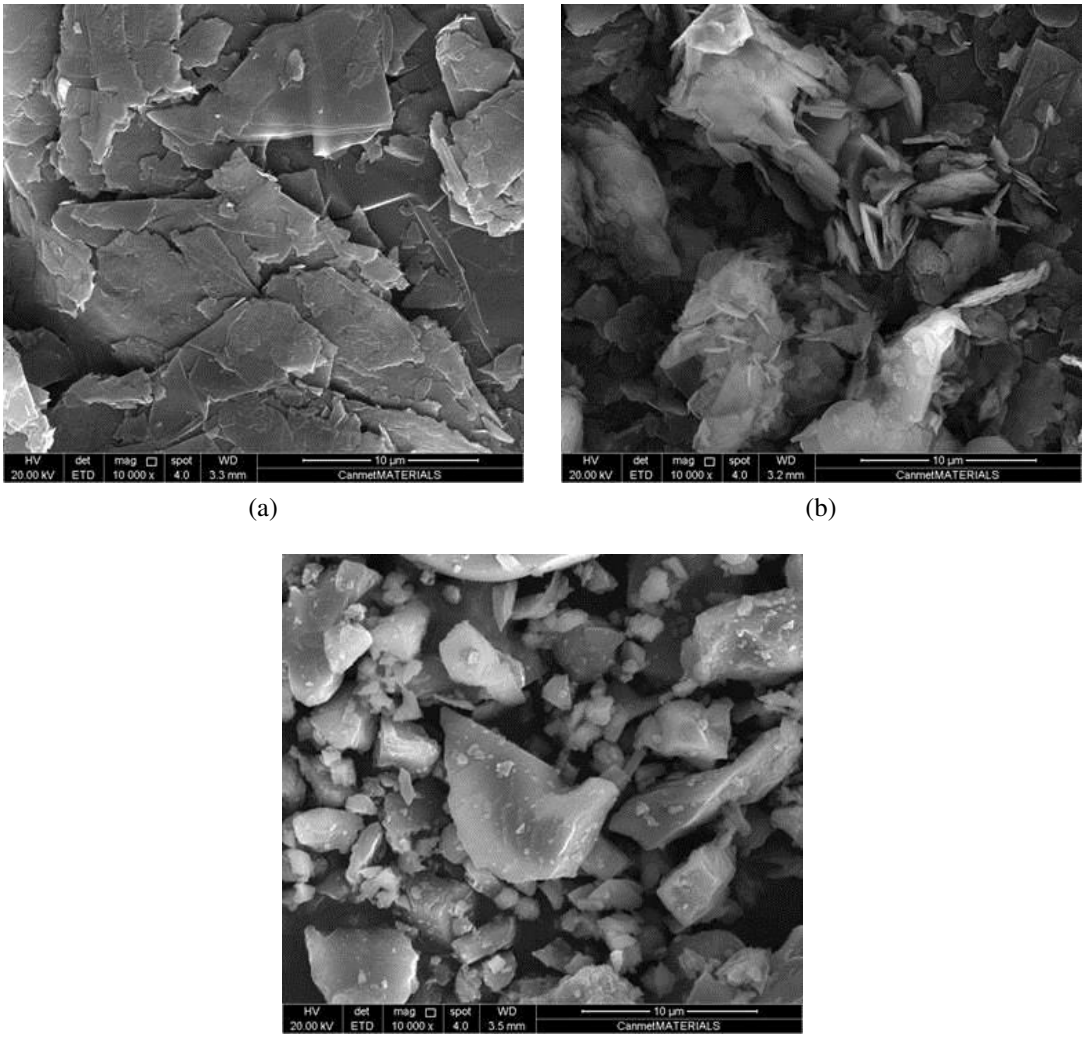

(a) (b)

(c)

Figure 5.10: SEM images of (a) Surface Enhanced Flake Graphite (b) Hexagonal Boron Nitride (c) Aluminum Nitride, all at 10µmscale

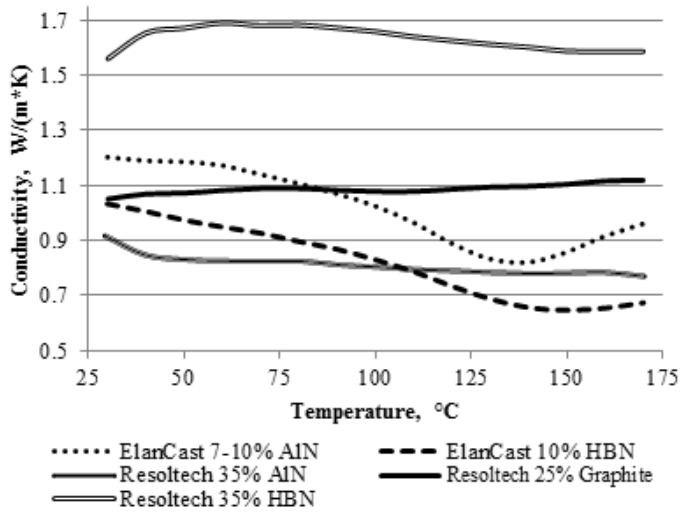

Figure 5.11: Thermal conductivity of considered materials over the expected operational temperature range.

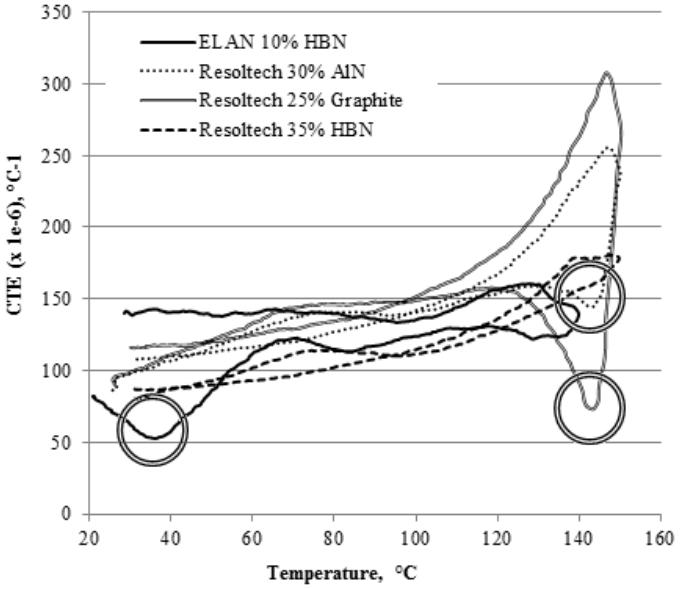

Figure 5.12: Coefficient of thermal expansion of considered materials for a heating and cooling cycle. Circles denote areas of suspected glass transition.

the wetting of the filler particle by the polymer matrix decreases with filler percentage. For the epoxy Resoltech HTG 200 which has a viscosity of 0.375 Pa·s, it was we found that a filler percentage of 35% Hexagonal Boron Nitride (HBN) was attainable while still remaining easily vacuum infusible. This allowed for a maximum thermal conductivity, in the temperature range from room temperature to 180°C, of 1.7 W/m·K. Resoltech HTG 200 was roughly thirteen times less viscous than Elan Cast P300 and was able to accommodate higher concentrations with ease. The results of this comparison study is presented in Fig. 5.11.

There are mechanical considerations when infusing a polymer composite in an enclosed space like the stator slot, for example thermal expansion is not constant with temperature. As a polymer is heated it can undergo a glass transition that changes the mechanical properties of the polymer greatly. Since the area within a stator slot is limited, an expanding polymer composite may have mechanical stresses applied by surrounding components; which as metals would not experience as great a thermal expansion. It is important to note when a polymer goes through the glass transition so as to determine if it will begin to behave differently under these stresses. As can be seen in Fig. 5.12, there is a dip in the coefficient of thermal expansion (CTE) that is characteristic of a glass transition in three of the four composites analyzed. At 150°C Resoltech HTG 200 with 35% HBN appears not to enter glass transition.

5.5 Thermal Evaluation

With a thermal management strategy in place, Rheberhegen et. al [141] took the loss distributions derived in Chapter 4 and input them into a thermo fluid simulator concluding that the machine should operate under the design conditions, i.e. the winding insulation thermal rating, 180°C.

5.6 Conclusions

A cooling jacket and two targeted winding cooling systems have been presented with respect to the target 22,000rpm 150kW SRM. Manufacturing and thermal details of an aluminum double-helix counterflow cooling jacket have been presented. Lost-core injection molded polymer cooling tubes inserted around the windings of the high frequency machine has been considered. The polymer material has high electrical resistivity and hence is insensitive to high frequency magnetic fields, contributing effectively zero eddy current losses to the motor, yet has thermal conductivity measured in the order of 2-2.7W/m·K. In order to improve heat removal of the non-electrically conductive cooling devices, two commercial encapsulates and three doping materials were investigated. Of the doped epoxies tested, Resoltech with 35% Hexagonal Boron Nitride presented the greatest enhancement of thermal conductivity, nor did the compound exhibit signs of glass transition in the temperature range tested. Thermal simulation of the described thermal management system suggests acceptable performance at rated speed and torque.

Chapter 6

Noise and Electromagnetic Comparison of a Three-Phase 12/8 and 12/10 SRM Design

6.1 Introduction to the 12/10 Machine Topology

In this Chapter, the three-phase 12/8 magnetic topology designed in Chapters 3 and 4 is evaluated in accordance with the design procedure described in Fig. 6.1, while also comparing it with a non-segmented, three-phase 12/10 design. While higher pole count often implies higher losses, the 12/10 functions entirely on short flux paths. Thus, the 12/10 core loss implications are not immediately clear when compared with a 12/8 configuration. Pole count also impacts on inductance and saliency, parameters which govern all aspects of performance. To better understand the non-segmented, three-phase 12/10, a comparative SRM study was performed maintaining major dimensions and magnetic materials between the 12/8 and 12/10 topologies. The influence of pole count on losses, torque quality, noise and vibration were compared under defined load conditions.

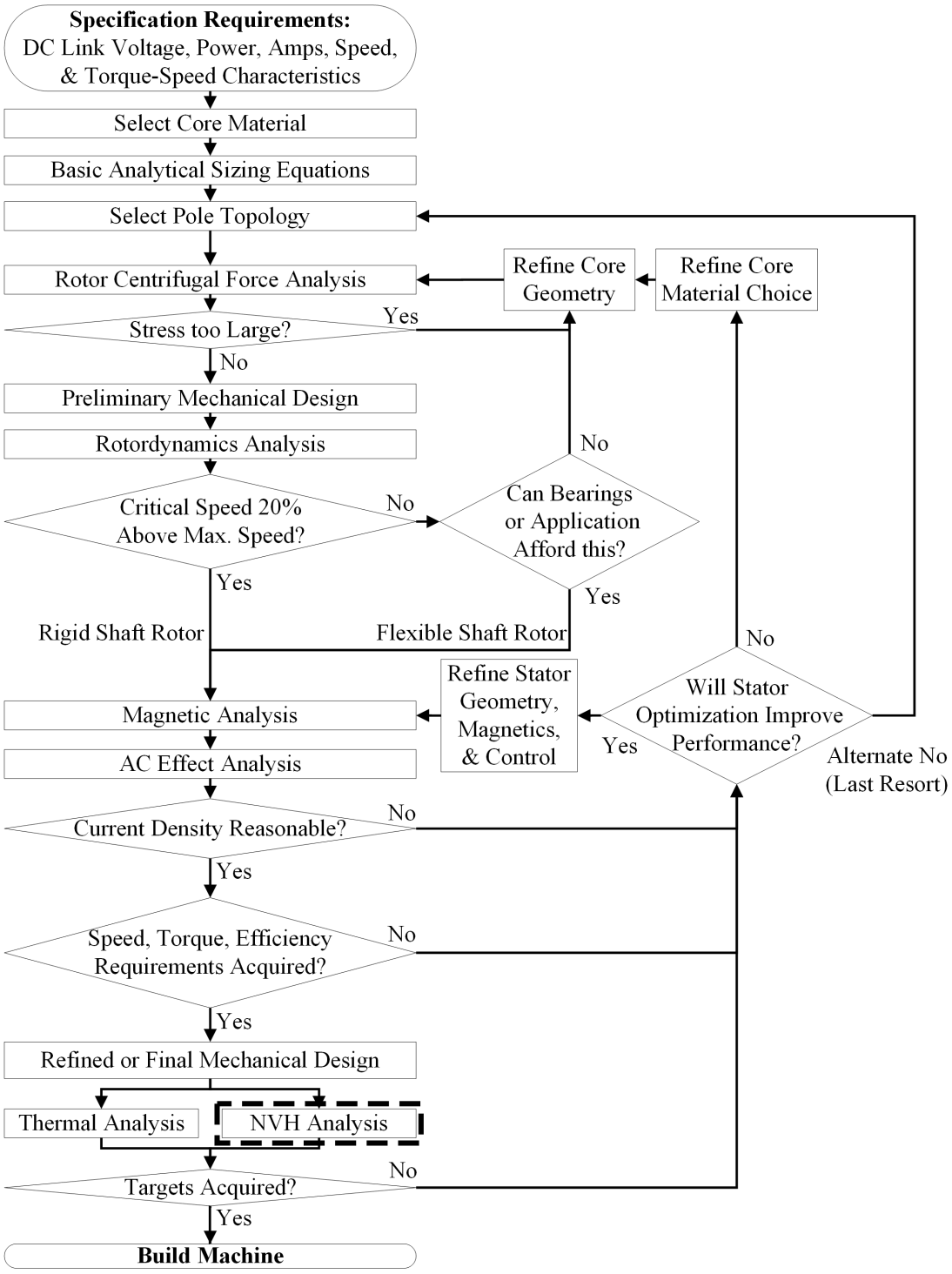

Figure 6.1: Proposed design flow for SRMs with high surface speed. The boxed region shows the where noise and vibration analysis is applied in the design procedure.

Despite being a strong machine contender in terms of specific power, noise and torque ripple remain challenges inhibiting adoption in many industries. High speed SRMs in particular have unusually poor torque ripple as mentioned in Chapter 2 and control innovations are limited in the single pulse region [100]. If control-based improvements to torque ripple and noise are limited, remaining options for enhancing traditional SRM performance typically involve magnetic geometry modification beginning with pole selection.

Three-phase 12/10's are not as widely researched as 12/8's, but have been investigated in literature [142–144]. Three-phase 12/10's, as opposed to six-phase, are of research interest, because power electronics are often a physically large and non-negligible expense.

Several researchers have developed three-phase 12/10 machines as segmented rotors [145–148]. Segmented SRMs compromise simplicity and hence the reliability benefits inherent of non-segmented machines; therefore, non-segmented 12/10's still have potential merit against 12/8 in aggressive environments. None of the publications to date directly compare non-segmented three-phase 12/8 and 12/10 machines, so this research intends to address this deficiency.

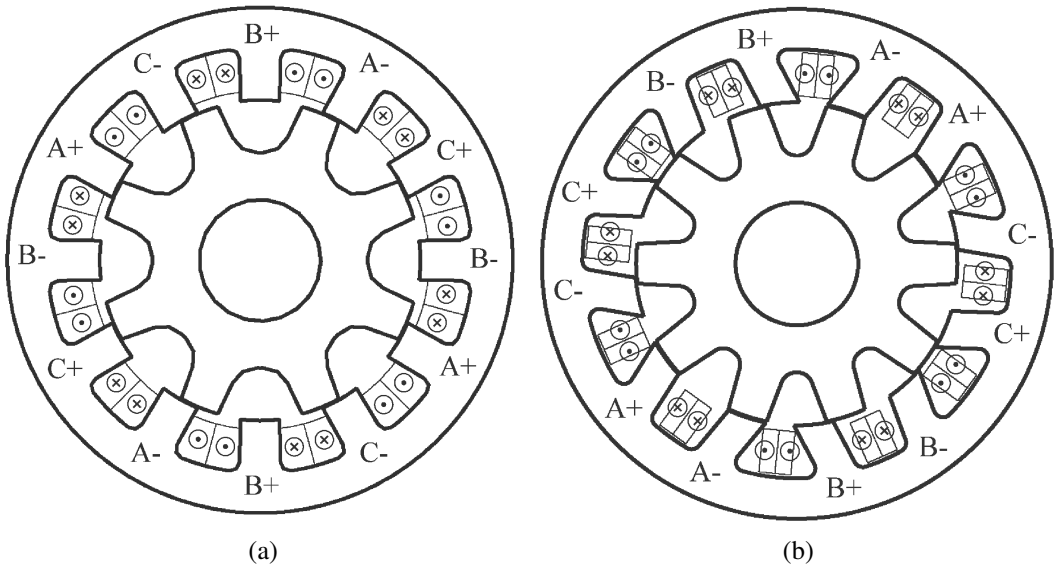

Figure 6.2: Winding directions for three-phase (a) 12/8 (b) 12/10.

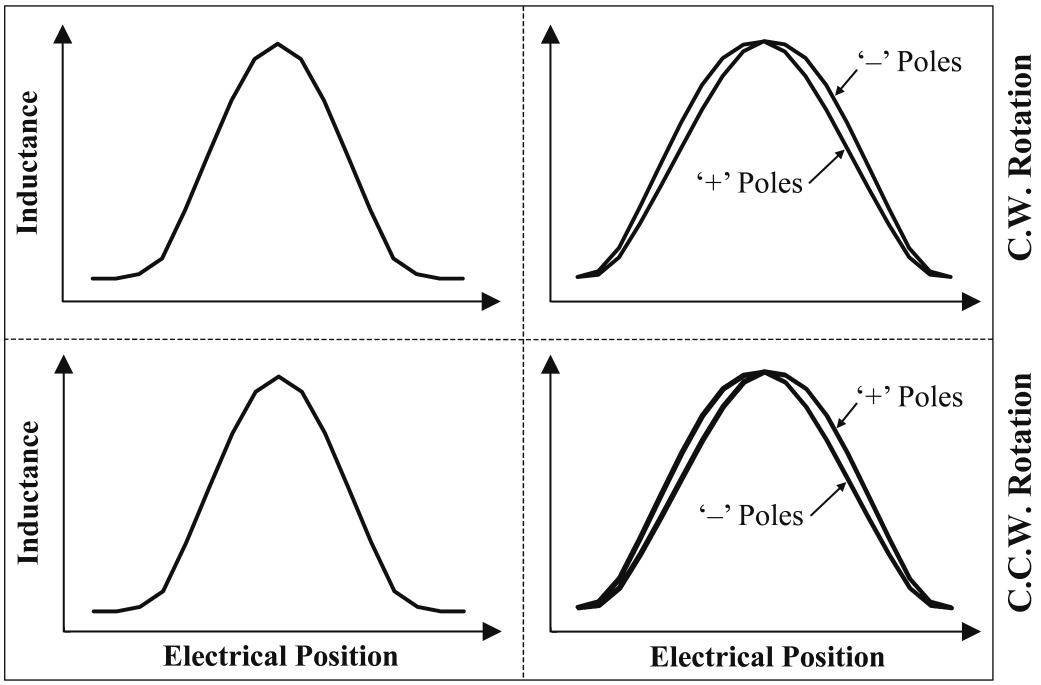

Figure 6.3: Phase inductance comparison of 12/8 and 12/10 SRMs with clockwise (C.W.) and counterclockwise (C.C.W.) rotation.

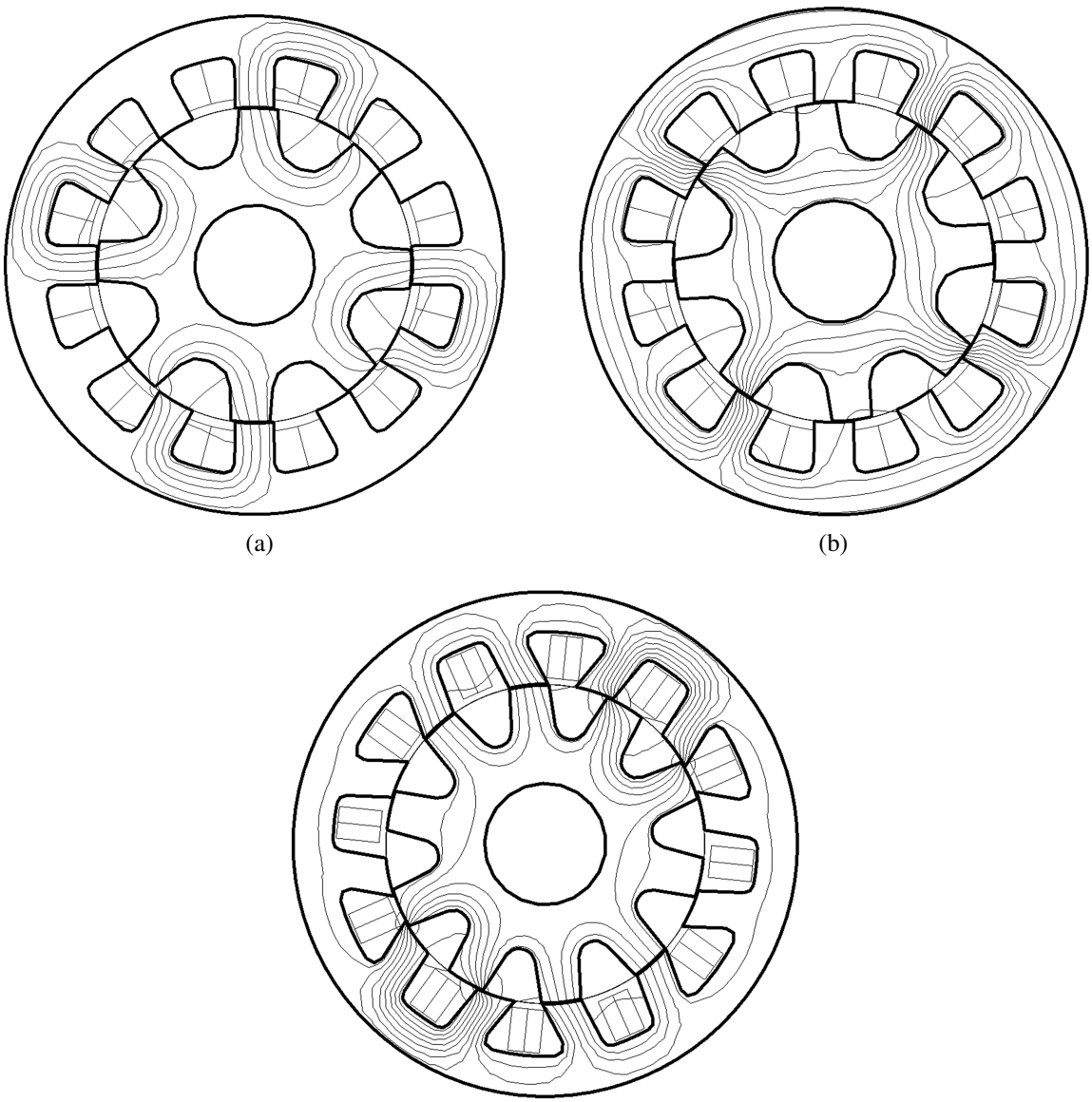

Figure 6.4: (a) Short flux path of three phase 12/8 (b) Long flux path of three phase 12/8 (c) Three phase 12/10 flux paths.

Differences between magnetic geometry and winding configuration for the two machine topologies is presented in Fig. 6.2. Here, plus (+) and minus (−) denote coil winding direction, where the 12/8 phase windings are equally spaced by 90° mechanical, while the 12/10 phase windings have adjacent poles with pole-pairs spaced by 180°

mechanical. The 12/10 also requires irregularly spaced stator poles which do not project radially through the axis of rotation as described by Bao et al [142]. Irregular spacing is necessary to ensure rotor and stator pole alignment; however, the design presents challenges due to corresponding inductance profile irregularities, as illustrated by the stylized phase inductance profiles for both 12/8 and 12/10 designs are shown in Fig. 6.3. Unlike the 12/8, individual poles of the 12/10 design lack symmetry about the aligned position. Instead, plus $(+)$ and minus $(-)$ pole inductances are mirror reflections about the ideal aligned position, Fig. 6.3.

Despite design challenges presented by inductance profile irregularity and winding difficulties resulting from pole geometry (as can be observed from Fig. 6.4, the 12/10 remains an interesting design to compare with that of the 12/8 for two primary reasons.

First, short flux paths are inherent in the 12/10 as shown in Fig. 6.4c. Figs. 6.4a and 6.4b show the short and long flux paths options respectively, for the 12/8 machine. Short flux paths exist during phase commutation sequences, whereas the long flux paths exist during conduction periods. For 12/10 topologies, Fig. 6.4c, all flux paths have short length, resulting from adjacently located pole-pairs. In terms of core loss, the 12/10 has higher excitation frequency, yet shorter flux path lengths than the 12/8, suggesting loss reduction could result despite increased frequency.

Second, peak current in the 12/10 is not expected to be as large as in the 12/8 due to increased electrical frequency. Lower peak current may be an economical trade-off for increased frequency if torque ripple, noise or vibration are reduced.

Section 6.2 will discuss the basis for comparison of the 12/8 and 12/10 topologies. Electromagnetic performance results will be presented in Section 6.3, while noise and vibration results will be presented in Section 6.4.

6.2 Comparison Description

In order to present accurate benchmarking of the two topologies, the machines must be, as much as possible, geometrically and magnetically congruent. A complete listing of parameters for both machines is shown in Table 6.1. All simulation parameters remained

Table 6.1: Machine Parameter Definition.

Component	Parameter	Unit	12/8	12/10
Stator	pole count	#	12	12
	outer diameter	mm	270	270
	backiron thickness	mm	21.4	21.4
	airgap diameter	mm	171.2	171.2
	tooth pole arc	deg	14	14
	tooth draft angle	deg	0	0
	tooth root radius	mm	5	5
	stack length	mm	100	100
Rotor	pole count	#	8	10
	outer diameter	mm	170	170
	backiron thickness	mm	25	25
	shaft diameter	mm	65	65
	tooth pole arc	deg	14.3	14.3
	tooth draft angle	deg	3	3
	tooth root radius	mm	14	8
	stack length	mm	100	100
Windings	supply voltage	V	600	600
	turns	#	13	13
	winding connection	*s , *p	2p 2s	2p 2s
	turn-on angle	elec deg	-19.2	-97.5
	turn-off angle	elec deg	133.6	81.5
	conduction period	mech deg	19.1	17.1
Core	lamination material	n/a	NO27	NO27
Jacket	thickness	mm	10	10
	material	n/a	Al6061	Al6061
Specification	speed	krpm	22	22
	torque	Nm	78	78

*p=parallel connected; *s=series connected

the same between the two machine topologies except rotor pole count and hence power electronic conduction angles. The 12/10 stator poles must be shifted, or angled, in order to align with rotor poles as previously discussed. 12/10 stator poles can be more 'straight' as in the case of Miller [143], but this results in unequal available slot area, so an angled geometry was adopted such as the 12/10 presented by Khor et al. [144] and the 2-phase 4/5 presented by Tanujaya et al [149]. Regardless the exact stator tooth geometry, stator pole arc angles were kept constant between the 12/8 and 12/10 machines.

Conduction angles have a large influence on machine performance; therefore, additional constraints were applied to retain magnetic similarity. First, machines were optimized to produce 78Nm of torque as close to continuous conduction mode as possible. Secondly, RMS phase current must be similar for equitable winding Joule loss. These two constraints were applied to mitigate the possibility of, for example, comparing a torque ripple optimized machine with an efficiency optimized machine. As a result of equivalent pole turn count, coil resistance, and differing inductance between topologies, continuous conduction for the 12/8 would produce more torque than 78Nm, so the widest conduction angle that yielded 78Nm was selected.

Inductance profile irregularity of the 12/10 also presented difficulty in transient machine analysis. For parallel connected phase windings, the inductance results in unbalanced current sharing between $(+)$ and $(-)$ poles as defined in Fig. 6.2. One pole per pole-pair would endure more current then the other depending on rotation direction. The relationship between rotation direction and inductance versus rotor angle is illustrated in Fig. 6.3. For series connected windings, current is forced to be distributed equally amongst coils; however, flux generation is not equivalent between poles. For this magnetic comparison, two-series, two-parallel pole connections were considered for both the 12/8 and 12/10 geometries in order to maintain uniform winding current distribution. Results of the described comparison conditions will be presented in the following sections.

6.3 Magnetic Performance Comparison

In this section simulation results investigating losses, current and torque are analyzed for comparable 12/8 and 12/10 magnetic geometries. Current and torque profiles for the 12/8 and 12/10 SRM designs are compared in Fig. 6.5 at 22,000rpm. Here, the torque and current waveforms are shown to be similar in shape and magnitude. While the 12/10 is nearly in continuous conduction, the 12/8 current waveform has small current deadzone in order to meet the conduction angle constraints described previously in Section 6.2.

Quantified details of torque, current and losses are listed in Table 6.2. Here, RMS phase current is shown to differ by 1.0%, despite 9% maximum current variation. As a result, average torque differs by 0.5%, yet the 12/10 had 7% lower torque ripple, where torque ripple is defined here as:

$$\frac{|\tau_{max} - \tau_{min}|}{\tau_{avg}} \tag{6.1}$$

The 12/10 demonstrated roughly 15% lower losses in the stator and 12% higher losses in the rotor than the 12/8. In total, the 12/10 has reduced core loss by 200W or 4% of total core loss.

Under other comparison conditions, perhaps differences between machines would be more pronounced, but for this investigative study, differences in core loss and torque ripple are minor, i.e. a 200W loss reduction is effectively negligible in a machine of this rating. Torque ripple reduction of 6Nm is also a modest improvement on a machine with 85Nm torque ripple. Noise and vibration behavior will be presented in the next section to further evaluate variations in machine designs

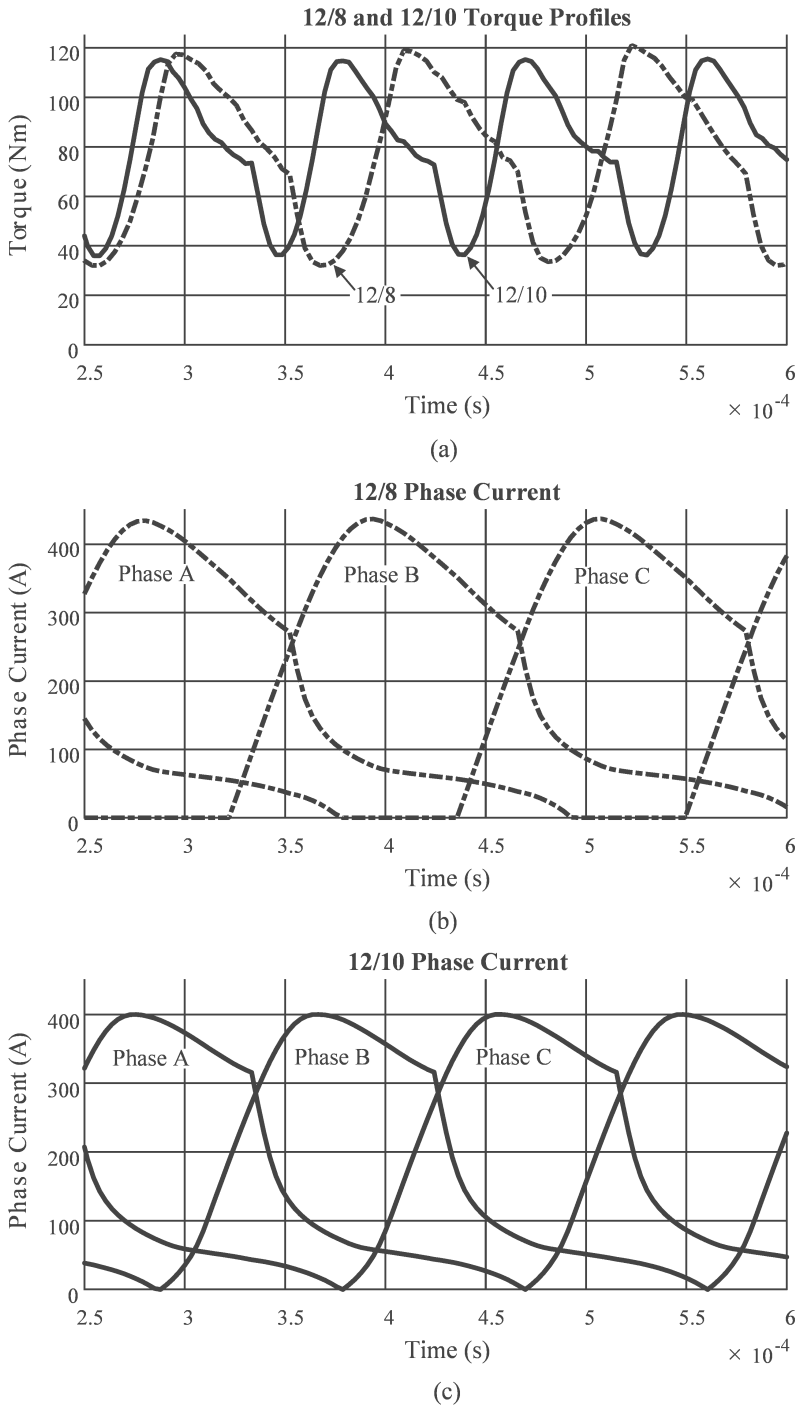

Figure 6.5: (a) Torque profiles for the 12/8 and 12/10 SRMs; (b) 12/8 phase currents; (c) 12/10 phase currents

Table 6.2: Simulated Results of 12/8 and 12/10 at 22kRPM.

Performance Metric	Unit	Type	12/8	12/10	Variation
Flux frequency	Hz	stator	2933	3666	+25.0%
		rotor	4400	4400	+0.0%
Stator iron loss	W	eddy	2917	2479	-15.0%
		hysteresis	383	335	-12.5%
		total	3300	2814	-14.7%
Rotor iron loss	W	eddy	1823	2088	+14.5%
		hysteresis	331	333	+0.6%
		total	2154	2421	+12.4%
Total iron loss	W	eddy	4740	4567	-3.8%
		hysteresis	714	668	-6.4%
		total	5454	5235	-4.0%
Phase current	A	peak	440	400	-9.1%
		rms	225	227	+1.0%
Winding loss	W	average	1054	1053	-0.1%
Torque	Nm	peak	120	115	-4.2%
		ripple	85	79	-7.1%
		average	78.1	78.5	+0.5%

6.4 Noise and Vibration Performance Comparison

In this section the 12/8 and 12/10 machine designs are compared with a common housing to illustrate differences in vibrations, resonating modes, sound power and magnetic forces at the design top speed of 22,000rpm. The frame considered in this analysis is an ideal aluminum cylinder with 10mm wall thickness. As with the magnetic analysis in the previous section, noise and vibration comparisons between 12/8 and 12/10 machines show interesting differences. As previously discussed, the 12/10 has lower peak current and lower torque ripple, which would intuitively suggest the possibility for reduced noise and vibration.

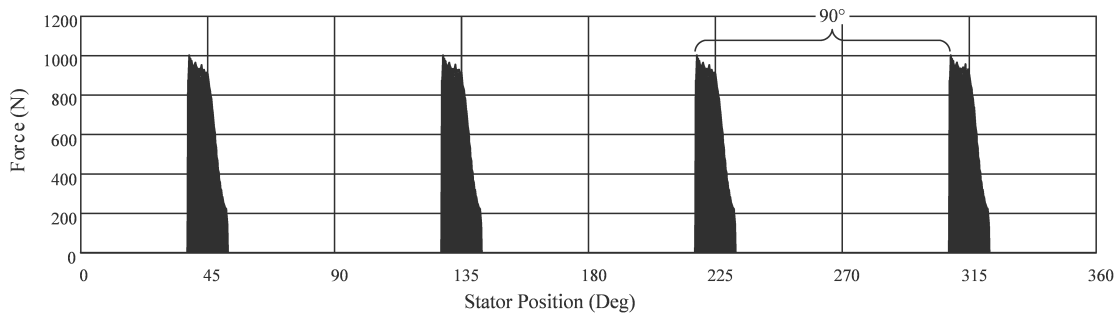

(a)

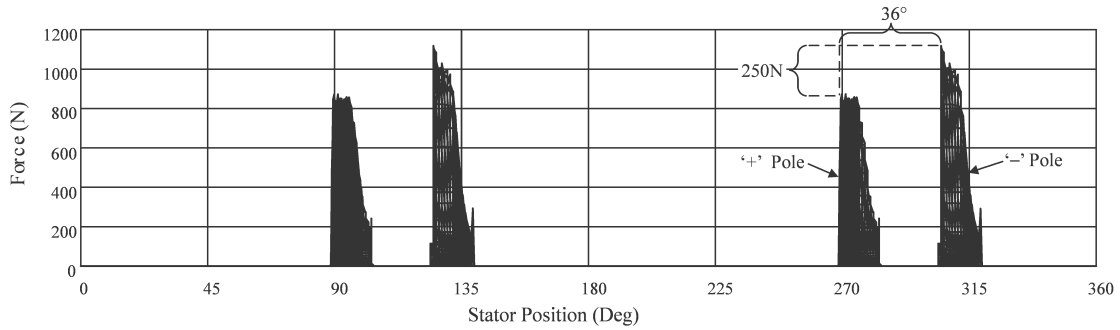

(b)

Figure 6.6: Airgap radial force distribution over a stroke calculated by electromagnetic finite element analysis (a) 12/8 and (b) 12/10.

Force distribution was first analyzed to better understand noise characteristics of the two machines. Fig. 6.6 shows absolute force distribution at the machine airgap due to excitation of a single phase over one electrical cycle. In Figure 6.6, the x-axis represents a fixed physical angular location at the stator airgap. Comparing Figures 6.6a and 6.6b, several conclusions can be drawn. First, inductance asymmetry influences force magnitude. Due to the series and parallel winding connections, current is the same in all four coils; however, flux differs between pole-pair coils. Differing flux results in differing radial forces. Here, $(+)$ and $(-)$ poles differ in peak force generation by 250N, or approximately 25%. Second, despite the 12/10 machine being electromagnetically designed for lower phase current and lower torque ripple than the 12/8, peak absolute radial force remains greatest in the 12/10 design by approximately 100N or 10%. Finally, 12/8 poles are evenly spaced (90°) apart,

whereas 12/10 pole pairs are concentrated 36° apart with 180° spacing between pole pairs. From a mechanical vibration perspective, 12/10 pole-pairs act as one large pole. From force analysis alone, 36° pole-pair spacing and peak forces greater than those on the 12/8, suggests 12/10 stator deformation will be more significant than the 12/8.

Forced response of the machine topologies was next conducted. The machine housings were rigidly constrained with a face-mounted type condition and 2% structural damping was assumed. Sound power was determined at a single point 300mm away from the center of the cores. Deflection and acceleration was measured at the stator tooth tips. Sound power, deflection and acceleration response are presented in Fig. 6.7, where the 12/10 tooth displacement reaches maximum $13\,\mu\mathrm{m}$ at 2,200Hz. Also apparent from Fig. 6.7 are the dominate mode frequencies. The 12/10 excites two modes at 22,000rpm; the second and fourth order modes at 2,200 and 6,100Hz, respectively. The 12/8 excites a single fourth order mode at 6,100Hz. Resonant mode shapes for both machines are presented in Fig. 6.8. Peak sound power also corresponds with the resonant modes. The 12/10 is expected to produce 124dB and 120dB at the second and fourth modes, respectively. The 12/8 produces 114dB at the fourth mode.

Due to the large rotational velocity under consideration, electrical frequency of the 12/10 passes the first resonant mode of the stator and frame. Electrical frequency and the second order mode would be coincident near 13,200rpm or 2,200Hz, where the greatest excited response would also be expected. Since the 12/8 excites a high order mode, beyond the electrical frequency, and because the 12/8 is less noisy than the 12/10 according to the sound power plot in Fig. 6.7, the 12/8 seems likely to provide lower sound production than the 12/10 over a rather wide operating region.

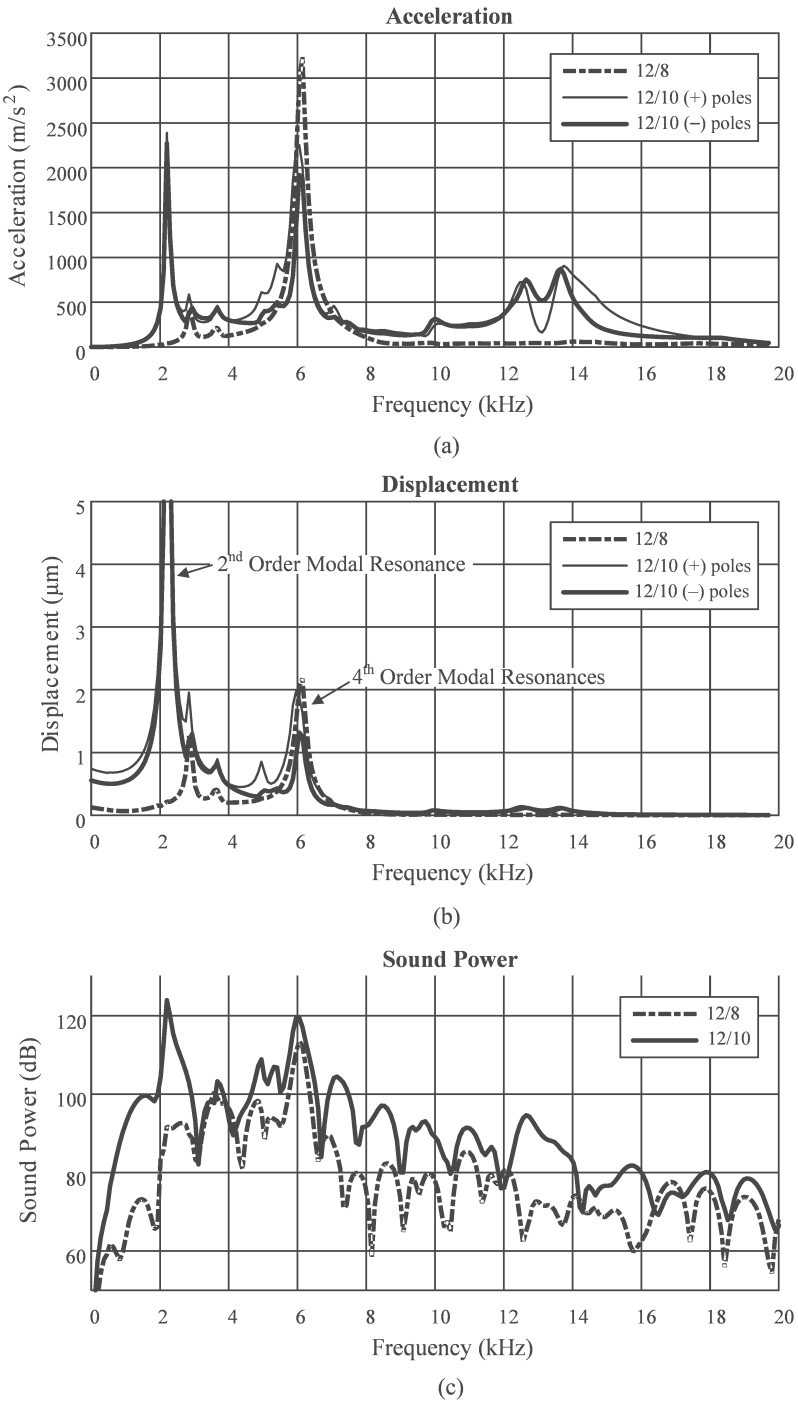

Figure 6.7: Tooth acceleration, displacement and resulting sound power for 12/8 and 12/10 SRMs.

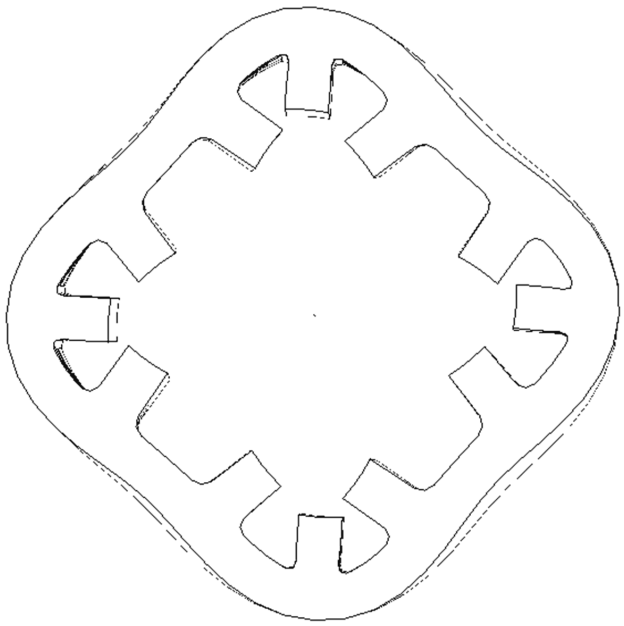

(a)

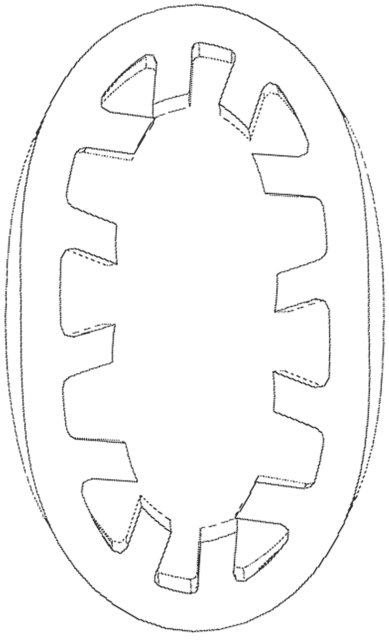

(b)

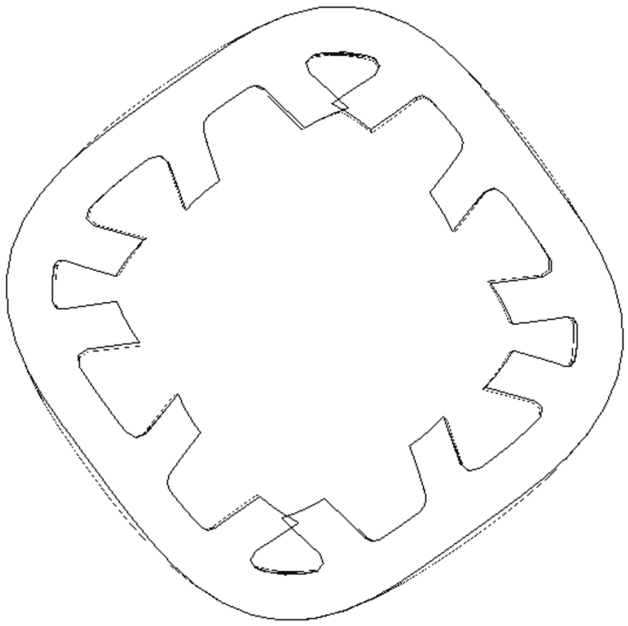

(c)

Figure 6.8: Mode shapes for (a) 12/8 at 6,100Hz (b) 12/10 at 2,200Hz (c) 12/10 at 6,100Hz.

6.5 Conclusions

A three-phase 12/8 switched reluctance machine has been compared with a three-phase 12/10 topology. Conduction angles were selected such that the machines produced 78Nm of load torque at 22,000rpm, while being as close to continuous conduction mode as possible. Under the aforementioned conditions, torque ripple, core loss and stator winding joule loss were found to be approximately equivalent. Torque ripple lowered 7% with the 12/10; however, this improvement is modest compared to the 110% torque ripple inherent in the example 12/8.

Noise and vibration characteristics were also evaluated for both machines. The 12/10 was found to not only have higher peak pole radial forces than the 12/8, but due to the adjacent pole-pair winding and stator design, pole-pair forces effectively aggregate into a single pole. This results in large stator deformation and resonance with the second order mode. The described second order resonance produced the largest sound power of either machine at 124dB, which is 10dB higher than the 12/8 machine. More broadly, the electrical frequency of the 12/10 is greater than the second order resonant frequency in this example. The 12/10 could be reasonably expected to excite most response from the second order mode when the electrical and mode frequencies coincide near 13,200RPM. Electrical frequency being below the resonant mode for the 12/8 suggests, for this investigation, the topology may produce lower sound power than the 12/10 over a wide operating envelope.

Chapter 7

Conclusions

7.1 Main Research Contributions

A review of the present state-of-the-art of switched reluctance machines which operate above 20,000rpm has been presented in Chapter 2. The term 'high-speed' has been investigated and developed by two slightly different concepts, $rpm * \sqrt{P_{kW}}$ and $rpm * P_{kW}$, where machine speed and peak power are interlinked via materials, magnetics and thermal considerations. In Chapter 2, a wide range of machines, drives and control methods have been investigated. The challenges, successes and design strategies of these projects became the basis for a new design methodology for finding maximum power capability at a specified speed is introduced in Chapter 3.

The design method examines structural mechanics prior to examining electro-magnetics, which is traditionally regarded as the first step in machine analysis. This logic flow is enabled by the simplicity of the switched reluctance rotor, which unlike induction and interior permanent magnet machines, is less likely to suffer stress concentrations in the rotor laminations which would make such a design procedure very challenging. Not only does this design flow identify structural problems early in the design

procedure, but the described structural analysis methods are computationally efficient. With an automated setup, mechanical design iterations can be executed in finite element analysis in under 2-3 seconds on a standard computer. The proposed design method uses rotor structural mechanics to identify the power limit of a switched reluctance machine under a set of design constraints, which can then be used to assess future design iterations.

Based on the design procedure specified, a 22,000rpm 150kW switched reluctance machine commensurate with automotive mass manufacturing practices has been outlined. For this example, magnetic evaluation is presented in Chapter 4. The machine was designed with 0.27mm non-oriented silicon steel lamination. Simulations show a 2.6kW/kg specific power and an estimated 94% efficiency, using material and manufacturing methods conventional to the automotive industry.

Using the efficiency and loss distributions from Chapter 4, a thermal design is described in Chapter 5. For a target application such as an electric vehicle, the liquid cooling system is considered with a system efficiency perspective. An efficient motor design with an inefficient cooling system is not an optimal solution for an electric vehicle where range is of prime importance. To achieve this, an encapsulated motor with a cooling jacket and internal cooling are investigated. A counterflow helical cooling jacket is considered for its high thermal efficiency and uniform thermal profile across the stator. Internal cooling pipes are considered around the windings and encapsulation. To achieve most effective internal cooling, material analysis was conducted on both the encapsulation and internal cooling tubes for best manufacturability, structural properties and thermal conductivity. Ultimately, simulations showed winding temperature below Class H insulation rating (180°C) at rated speed and power.

Torque ripple remains a challenge for the 12/8 machine, and so a three-phase non-segmented 12/10 was investigated in Chapter 6 in an attempt to try and reduce torque ripple. While the 12/10 presents a number of interesting advantages over 12/8, torque ripple was

found to be reduced by only a few percent, while noise magnitude increased significantly, a direct result of the 12/10's winding requirements for magnetic functionality. Consequently, the 12/10 was not determined to be advantageous over the 12/8 for this example application.

Reducing torque ripple for high speed switched reluctance machines will undoubtedly remain a challenge without a significant revolution in the state of the art. While the high-speed switched reluctance machine under consideration is believed to be reasonably low cost, reasonably efficient, and have good specific power, a system designer considering the use of high speed switched reluctance machines should be aware of the severity of torque ripple, and understand that any power transmission components will likely need special consideration to accommodate the severe torque ripple associated with switched reluctance machines.

7.2 Machine Parameter Final Summary

Initial design targets were met or exceeded with the machine design. A list summarizing machine parameters is presented in Table 7.1.

Table 7.1: Final Design Specification List

Specification	**Design**	**Target**	**Unit**
Max. Rated Speed	22,000	22,000	rpm
Max. Continuous Power (Out)	150	150	kW
Max. Overload Power (Out)	211	undefined	kW
Base Speed	17,000	undefined	rpm
Min. Stress Safety Factor	1.98	2	n/a
Min. Critical Speed	26,500	26,500	rpm
Magnetic Efficiency	97	undefined	%
Estimated Real Efficiency	94	94	%
Specific Power	2.6	1.4	kW/kg
Magnetic Material Mass	30.5	107	kg
Total Machine Mass	55	unspecified	kg
Rotor inertia	0.0322	unspecified	kg*m^2
Stator Outer Diameter	270	unspecified	mm
Stack Length	100	unspecified	mm
Rotor Outer Diameter	170	unspecified	mm
DC Link Voltage	600	600	VDC
Peak Phase Current	500	480	A
Max. IGBT switch frequency	5000	5000	Hz
Coolant	Water/Glycol	Water/Glycol	n/a
Wire Insulation	Class H	Class H	n/a
Wire Cross Section	rectangular	unspecified	n/a
Equivalent Wire Gauge	10	unspecified	AWG
Number of Turns	30	unspecified	n/a
Lamination Material	Cogent Power NO27	NO low silicon iron	n/a
Lamination Thickness	0.27	$0.18 \leq x \leq 0.35$	mm
Max. SPL @ 1 meter	114 @ 22,000rpm	undefined	dB
Torque Ripple	Up to 138Nm	undefined	n/a

Theoretical mechanical representations of the machine are depicted in Figs. 7.1, 7.2 and 7.3. Table 7.2 provides a brief component description for the items depicted in Figs. 7.1 and 7.2. Figure 7.3 shows the final machine fully assembled with the many fittings for liquid cooling and wire interconnects.

Table 7.2: Machine component identification

	Component	Description
Rotor	A	Rotor laminations
	B	Drive-end end plate
	C	Drive-end bearing
	D	Shaft
	E	Bolts
	F	Ceramic washers for electrical isolation of bolts
	G	Anti-rotation plate
	H	Lock nut
	I	Anti-drive-end bearing
	J	Anti-drive-end end plate
	K	Resolver
Stator	A	Stator laminations
	B	Lamination clamping plate
	C	End-turn cooling tube
	E	Windings
	F	Axial cooling tubes
	G	Nomex slot liner

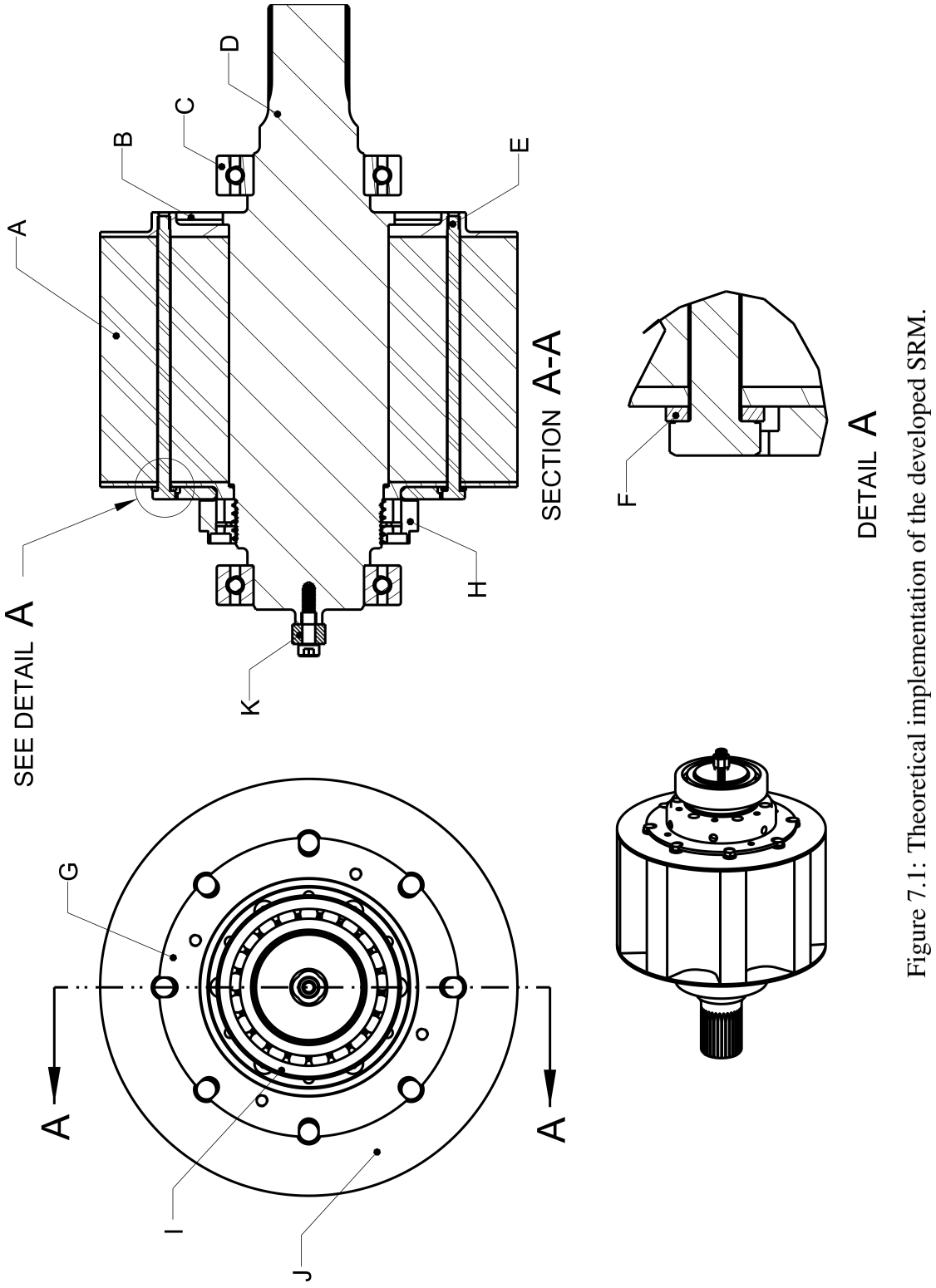

Figure 7.1: Theoretical implementation of the developed SRM.

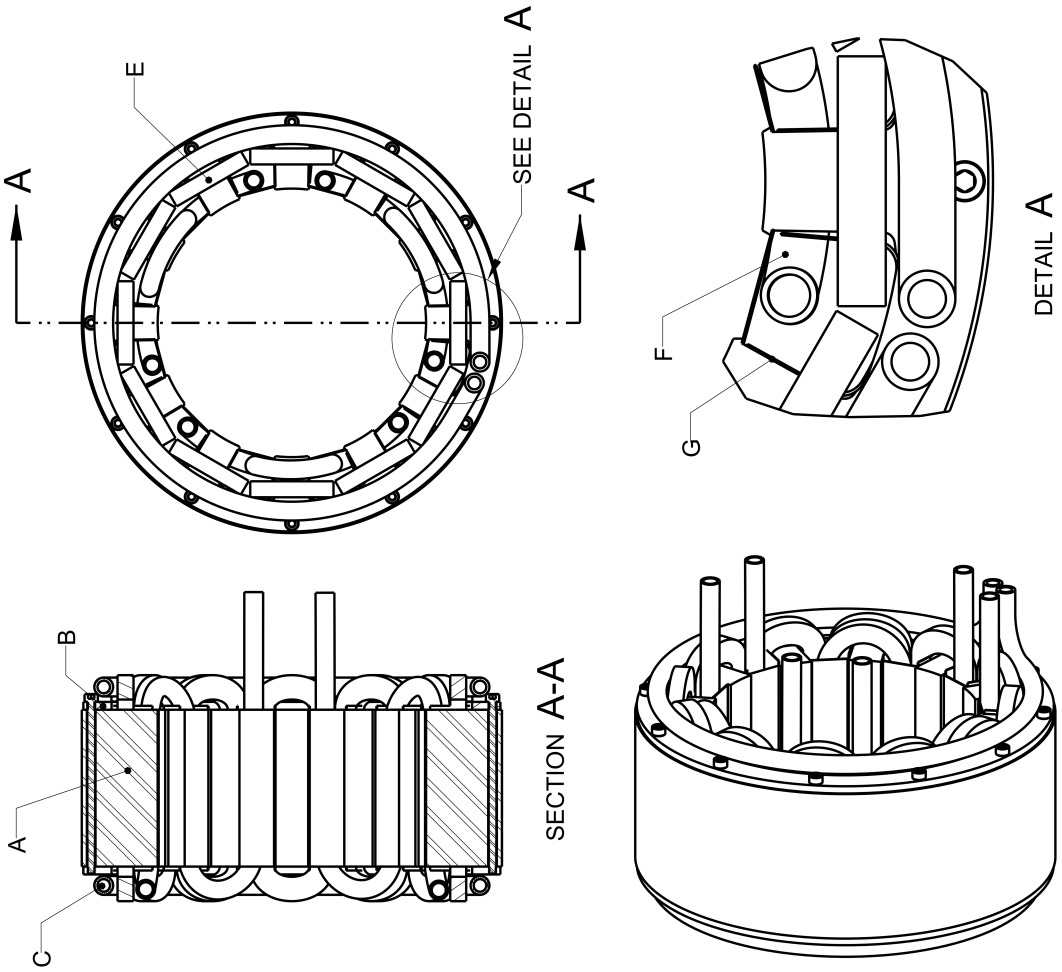

Figure 7.2: Theoretical implementation of the developed SRM. Encapsulation is hidden for visibility

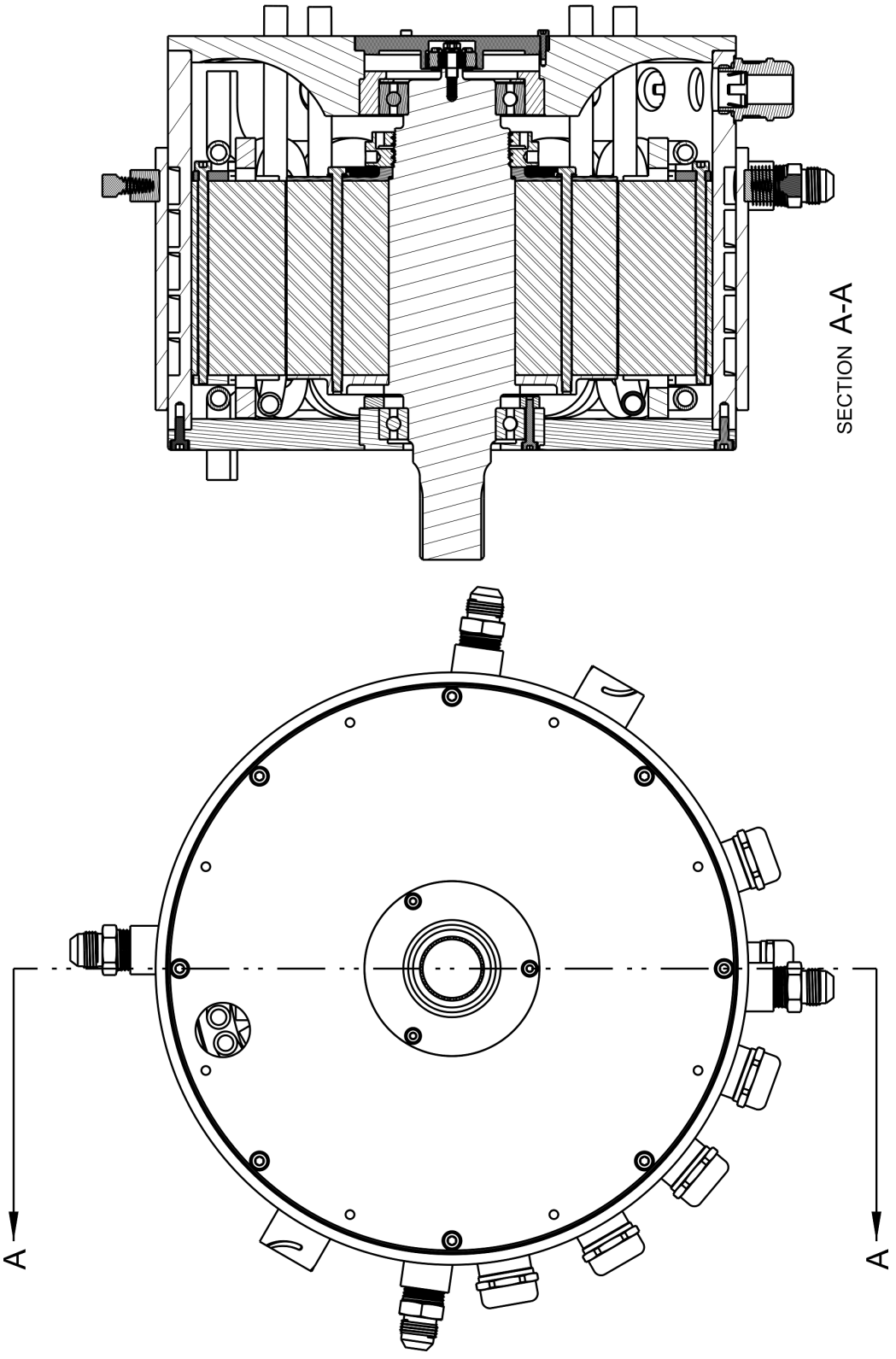

Figure 7.3: Theoretical implementation of the developed SRM.

7.3 Suggestions for Future Research

Recommended future research include:

1. Further magnetic refinement. As described in Chapter 4 an additional design iteration into the number turns, stack length and conduction angles would likely better optimize the machine for the design specifications.

2. Experimental validation. This work is heavily reliant on a multitude of finite element based simulation results. Some phenomena discussed in this research is more complex to simulate and analyze than other phenomena. The next step in validating this design procedure and the findings discovered during the design process would be to build the described machine and correlate results with simulated findings. Recommended experiments for design verification include efficiency mapping, endurance testing, measuring rotor vibrations during a spin up, as well as thermal, noise and vibration characterization at maximum rated speed.

3. More focus on the drive to reduce noise and torque ripple. As mentioned in Chapter 4 and 6.4, noise and torque ripple are fairly significant. These issues can be improved with effective drive and control design. One possible research direction is the Neutral Point Converter, a type of 3-level multiconverter, proposed by Peng [150].

4. More investigation into thermal management methods such as direct cooling systems which can potentially simplify the design and enhance effectiveness.

5. Additional research on rapid identification of the power-speed relationship for electric machines. $rpm\sqrt{kW}$ is not known to be a derivable parameter from basic physics principles. Consequently, the merit of the parameter is not well understood. Being based on empirical evidence, the high-speed index presented by Moghaddam [5] is

believed to be a stronger representation of the relationship between power and speed of electric machines. This thesis serves as a procedural method of identifying the speed-power relationship for SRMs; however, a faster identification method would help preliminary design validation.

7.4 Publications and Other Outcomes

To date, the following publications have resulted from this Ph.D. study:

Journal Publications

1. S. Castano, B. Bilgin, **E. Fairall**, and A. Emadi, Acoustic Noise Analysis of a High-Speed High-Power Switched Reluctance Machine: Frame Effects, IEEE Transactions on Energy Conversion, vol. 31, no. 1, pp. 6777, Mar. 2016.

2. D. Hilgersom, **E. Fairall**, B. Bilgin, T. Hofman, and A. Emadi, Round and Rectangular Winding Loss Analysis and Optimization for a 22,000rpm 150kW Switched Reluctance Machine, Pending publication in the International Journal of Powertrains.

Conference Publications

1. **E. Fairall**, B. Bilgin, and A. Emadi, State-of-the-Art High-Speed Switched Reluctance Machines, in IEEE International Electric Machines & Drives Conference, Coeur d'Alène, ID, USA, 2015.

2. **E. Fairall**, C. Rheberhegen, E. Rowan, J. Lo, B. Bilgin, and A. Emadi, Maximizing thermal effectiveness and minimizing parasitic loss in a liquid cooled switched reluctance machine, in 2016 IEEE Transportation Electrification Conference and Expo (ITEC), Dearborn, MI, USA, 2016, pp. 17.

3. **E. Fairall**, N. Schofield, and A. Emadi, Noise and electromagnetic comparison of a three-phase 12/8 and a 12/10 switched reluctance machine, in 2016 IEEE Transportation Electrification Conference and Expo (ITEC), Coeur d'Alène, ID, USA, 2016, pp. 15.

4. H. Li, **E. Fairall**, B. Bilgin, and A. Emadi, Performance Evaluation of a High-Speed High-Power Switched Reluctance Motor Drive, in IEEE Applied Power Electronics Conference, Charlotte, NC, USA, 2015, pp. 13371342.

Patents

1. **E. Fairall**, B. Bilgin, and A. Emadi, High-Speed High-Power Switched Reluctance Machine, Internal reference number 15-007 and 14/736,106.

References

[1] K. M. Rahman and S. E. Schulz, "Design of high efficiency and high density switched reluctance motor for vehicle propulsion," in *IEEE Industry Applications Society Thirty-Sixth Annual Meeting*, vol. 3, Chicago, IL, USA, Oct. 2001, pp. 2104–2110.

[2] A. Maeda and H. Tomita, "Power and Speed Limitations in High Speed Electrical Machines," in *International Power Electronics Conference*, Yokohama, Japan, Apr. 1995, pp. 1321–1326.

[3] D. Gerada, A. Mebarki, N. L. Brown, C. Gerada, A. Cavagnino, and A. Boglietti, "High-Speed Electrical Machines: Technologies, Trends, and Developments," *IEEE Transactions on Industrial Electronics*, vol. 61, no. 6, pp. 2946–2959, Jun. 2014.

[4] R. D. van Millingen and J. D. van Millingen, "Phase shift torquemeters for gas turbine development and monitoring," in *ASME 1991 International Gas Turbine and Aeroengine Congress and Exposition*, Orlando, FL, USA, Jun. 1991, pp. 1–10.

[5] R. R. Moghaddam, "High speed operation of electrical machines, a review on technology, benefits and challenges," in *IEEE Energy Conversion Congress and Exposition*, Sep. 2014, pp. 5539–5546.

[6] W. Tong, *Mechanical Design of Electric Motors*. Boca Raton: CRC Press, Apr. 2014.

[7] A. Binder and T. Schneider, "High-speed inverter-fed AC drives," in *International Aegean Conference on Electrical Machines and Power Electronics*. Bodrum, Turkey: IEEE, Sep. 2007, pp. 9–16.

[8] "Order a Tesla Model S | Tesla." [Online]. Available: https://www.tesla.com/models/design (Accessed Sep. 25, 2016).

[9] D. Roper, "Tesla Model S," Sep. 2016. [Online]. Available: http://www.roperld.com/science/TeslaModelS.htm (Accessed Sep. 25, 2016).

[10] "Model S Specifications," Jan. 2015. [Online]. Available: https://www.tesla.com/support/model-s-specifications (Accessed Sep. 25, 2016).

[11] "2011 Nissan LEAF First Responders Guide.pdf." [Online]. Available: http://www.nissan-techinfo.com/refgh0v/og/FRG/2011-Nissan-LEAF-FRG.pdf (Accessed Sep. 26, 2016).

[12] "2016 Ford Focus Electric Tech Specs." [Online]. Available: https://media.ford.com/content/fordmedia/fna/us/en/asset.download.document.pdf.html/content/dam/fordmedia/North%20America/US/product/2016/2016-ford-focus-electric-tech-specs.pdf (Accessed Sep. 25, 2016).

[13] Fiat500USA.com, "Fiat 500e Full Vehicle Specifications!" [Online]. Available: http://www.fiat500usa.com/2013/04/fiat-500e-full-vehicle-specifications.html (Accessed Sep. 26, 2016).

[14] "2016 Fiat 500e." [Online]. Available: https://www.fueleconomy.gov/feg/Find.do?action=sbs&id=37156 (Accessed Sep. 26, 2016).

[15] "FIAT 500e Models | Quick Comparison Chart." [Online]. Available: http://www.fiatusa.com/model-compare/quick-chart/?modelYearCode=CUX201604 (Accessed Sep. 26, 2016).

[16] "Battery Pack Laboratory Testing Results 2013 Ford Focus Hatchback," Apr. 2016. [Online]. Available: https://avt.inl.gov/sites/default/files/pdf/fsev/batteryFocus2578.pdf (Accessed Sep. 25, 2016).

[17] "2016 Focus Electric | View Focus Electric Highlights | Ford.com." [Online]. Available: http://www.ford.com/cars/focus/trim/electric/ (Accessed Sep. 25, 2016).

[18] "2016 Ford Focus Electric." [Online]. Available: https://www.fueleconomy.gov/feg/Find.do?action=sbs&id=36978 (Accessed Sep. 25, 2016).

[19] "2016 Nissan LEAF® Electric Car Specs." [Online]. Available: http://www.nissanusa.com/electric-cars/leaf/versions-specs (Accessed Sep. 26, 2016).

[20] "The 2016 BYD e6 Will Get a Longer Driving Range of 400km." [Online]. Available: http://chinaautoweb.com/2015/05/the-2016-byd-e6-will-get-a-longer-driving-range-of-400km/ (Accessed Sep. 26, 2016).

[21] "BYD E6." [Online]. Available: http://chinaautoweb.com/car-models/byd-e6/ (Accessed Sep. 26, 2016).

[22] Z. Shahan, "EV Battery Prices: Looking Back A Few Years, & Forward Yet Again," May 2016. [Online]. Available: https://cleantechnica.com/2016/05/15/ev-battery-prices-looking-back-years-forward-yet/ (Accessed Sep. 25, 2016).

[23] P. Faguy, "Overview of the DOE Advanced Battery R&D Program," Jun. 2015. [Online]. Available: http://energy.gov/sites/prod/files/2015/06/f23/es000_faguy_2015_o.pdf (Accessed Sep. 25, 2016).

[24] N. Schofield and M. K. Jenkins, "High performance brushless permanent magnet traction drives for hybrid electric vehicles," in *IEE Colloquium on Machines and Drives for Electric and Hybrid Vehicles (Digest No: 1996/152)*, Jun. 1996, pp. 4/1–4/6.

[25] J. Dong, Y. Huang, L. Jin, B. Guo, T. Zhou, H. Lin, and J. Dong, "Development of an Air-cooled 150 kW High Speed Permanent Magnet Motor with Gramme Ring Windings for Turbo Blowers," in *International Conference on Electrical Machines and Systems*, Hangzhou, China, Oct. 2014, pp. 3534 – 3538.

[26] M. Rahman, A. Chiba, and T. Fukao, "Super High Speed Electrical Machines - Summary," in *IEEE Power Engineering Society Summer Meeting*, vol. 2, Denver, CO, USA, Jun. 2004, pp. 1272–1275.

[27] W. F. d'Arcier and L. Sérillon, "Thermal modelling of permanent magnet motor for traction," Master's Thesis, KTH Royal Institute of Technology, Stockholm, Sweden, 2007.

[28] Q. Yu, "Thermal and Electromagnetic Modeling of a Canned Switched Reluctance Machine," Ph.D. Thesis, Universiaet der Bundeswehr, München, Neubiberg, Germany, Jun. 2012.

[29] C. Laudensack, Y. Polonskiy, and G. Gerling, "Measurement and Performance Analyses of Dry-running and Canned Switched Reluctance Machines," in *IEEE International Electric Machines and Drives Conference*, Coeur d'Alène, ID, USA, May 2015, pp. 376–382.

[30] S. Li, Y. Li, W. Choi, and B. Sarlioglu, "High-Speed Electric Machines: Challenges and Design Considerations," *IEEE Transactions on Transportation Electrification*, vol. 2, no. 1, pp. 2–13, Mar. 2016.

[31] "Critical Materials Strategy," U.S. Department of Energy, Tech. Rep., Dec. 2011.

[32] "TECHNOLOGY: 5 years after crisis, U.S. remains dependent on China's rare earth elements." [Online]. Available: http://www.eenews.net/stories/1060011478 (Accessed Nov. 7, 2015).

[33] M. Caprio, V. Lelos, J. Herbst, and J. Upshaw, "Advanced induction motor endring design features for high speed applications," in *International Electric Machines and Drives Conference*, San Antonio, TX, USA, May 2005, pp. 993–998.

[34] J. H. Dymond and R. D. Findlay, "Some commentary on the choice of rotor bar material for induction motors," *IEEE Transactions on Energy Conversion*, vol. 10, no. 3, pp. 425–430, Sep. 1995.

[35] C.-H. Jun and A. Nicolas, "Analysis of the mechanical stresses on a squirrel cage induction motor by the finite element method," *IEEE Transactions on Magnetics*, vol. 35, no. 3, pp. 1282–1285, May 1999.

[36] A. Arkadan and B. Kielgas, "Switched reluctance motor drive systems dynamic performance prediction under internal and external fault conditions," *IEEE Transactions on Energy Conversion*, vol. 9, no. 1, pp. 45–52, Mar. 1994.

[37] I. Husain, A. Radun, and J. Nairus, "Fault analysis and excitation requirements for switched reluctance-generators," *IEEE Transactions on Energy Conversion*, vol. 17, no. 1, pp. 67–72, Mar. 2002.

[38] A. V. Radun, "High power density switched reluctance motor drive for aerospace applications," in *Conference Record of the 1989 IEEE Industry Applications Society Annual Meeting*. IEEE, 1989, pp. 568–573.

[39] G. Montague, M. Jansen, B. Ebihara, R. Jansen, A. Palazzolo, R. Tucker, J. Preuss, A. Hunt, J. Trudell, and A. Provenza, "Design and Fabrication of High-Temperature Radial Magnetic Bearing for Turbomachinery," National Aeronautics and Space Administration, Glenn Research Center, Cleveland, OH, USA, Technical Memorandum TM-2003-212300, Jul. 2003.

[40] K. Ha, C. Lee, J. Kim, R. Krishnan, and S.-G. Oh, "Design and Development of Low-Cost and High-Efficiency Variable-Speed Drive System With Switched Reluctance Motor," *IEEE Transactions on Industry Applications*, vol. 43, no. 3, pp. 703–713, May 2007.

[41] J. Widmer, R. Martin, and B. Mecrow, "Pre-Compressed and Stranded Aluminium Motor Windings for Traction Motors," in *IEEE International Electric Machines & Drives Conference*, Coeur d'Alène, ID, USA, May 2015.

[42] A. Hava, V. Blasko, and T. A. Lipo, "A modified C-dump converter for variable reluctance machines," in *IEEE Industry Applications Society Annual Meeting*, vol. vol.1, Dearborn, MI, USA, Sep. 1991, pp. 886–889.

[43] E. Richter and C. Ferreira, "Performance evaluation of a 250 kW switched reluctance starter generator," in *IEEE Industry Applications Conference*, Orlando, FL, USA, Oct. 1995, pp. 434–440.

[44] J. Kunz, S. Cheng, Y. Duan, J. Mayor, R. Harley, and T. Habetler, "Design of a 750,000 rpm switched reluctance motor for micro machining," in *IEEE Energy*

Conversion Congress and Exposition, Atlanta, Georgia, USA, Sep. 2010, pp. 3986–3992.

[45] T. Wichert, "Design and Construction Modifications of Switched Reluctance Machines," Ph.D. Thesis, Warsaw University of Technology, Warsaw, Poland, 2008.

[46] S. H. Won, J. S. Ahn, K. C. Kim, and J. Lee, "Performance Prediction of Switched Reluctance Motor Considering Windage Loss for High Speed Application," in *IEEE Conference on Electromagnetic Field Computation*, Miami, Florida, USA, May 2006, pp. 417–417.

[47] S. H. Won, J. Choi, and J. Lee, "Windage Loss Reduction of High-Speed SRM Using Rotor Magnetic Saturation," *IEEE Transactions on Magnetics*, vol. 44, no. 11, pp. 4147–4150, Nov. 2008.

[48] J. Lin, P. Suntharalingam, N. Schofield, and A. Emadi, "Comparison of high-speed switched reluctance machines with conventional and toroidal windings," in *IEEE Transportation Electrification Conference and Expo*, Dearborn, MI, USA, Jun. 2016, pp. 1–7.

[49] L. Jianing, P. Suntharalingam, N. Schofield, and A. Emadi, "High-Speed Switched Reluctance Machine Design with Toroidal-Windings," in *IEEE Energy Conversion Congress and Exposition*, Dearborn, MI, USA, Sep. 2015, pp. 1789–1794.

[50] M. T. Ebrahim, "A very high speed switched reluctance generator," Ph.D. Thesis, University of Nottingham, Nottingham, UK, Jan. 1995.

[51] L. Chen and W. Hofmann, "Design procedure of bearingless high-speed switched reluctance motors," in *International Symposium on Power Electronics Electrical Drives Automation and Motion*, Pisa, Italy, Jun. 2010, pp. 1442–1447.

[52] L. Chen and W. Hofmann, "Modelling and control of one bearingless 8-6 switched reluctance motor with single layer of winding structure," in *European Conference on Power Electronics and Applications*, Birmingham, UK, Aug. 2011, pp. 1–9.

[53] L. Chen and W. Hofmann, "Analytically Computing Winding Currents to Generate Torque and Levitation Force of a New Bearingless Switched Reluctance Motor," in *Power Electronics and Motion Control Conference*, Portoroz, Slovenia, Aug. 2006, pp. 1058–1063.

[54] L. Chen and W. Hofmann, "Speed Regulation Technique of One Bearingless 8/6 Switched Reluctance Motor With Simpler Single Winding Structure," *IEEE Transactions on Industrial Electronics*, vol. 59, no. 6, pp. 2592–2600, Jun. 2012.

[55] D.-H. Lee and J.-W. Ahn, "Performance of High-Speed 4/2 Switched Reluctance Motor," *Journal of Electrical Engineering and Technology*, vol. 6, no. 5, pp. 640–646, Sep. 2011.

[56] D.-H. Lee, J. Lee, and J.-W. Ahn, "Current control of a high speed SRM with an advanced 4-level converter," in *International Conference on Power Electronics and Energy Conversion Congress & Expo Asia*, Jeju, Korea, May 2011, pp. 109–114.

[57] D.-H. Lee, S.-Y. Ahn, J.-W. Ahn, and J.-M. Kim, "Modified TSF for the high speed Switched Reluctance Motor," in *IEEE International Symposium on Industrial Electronics*, Gdansk, Poland, Jun. 2011, pp. 655–660.

[58] D.-H. Lee, T. H. Pham, and J.-W. Ahn, "Design and Operation Characteristics of Four-Two Pole High-Speed SRM for Torque Ripple Reduction," *IEEE Transactions on Industrial Electronics*, vol. 60, no. 9, pp. 3637–3643, Sep. 2013.

[59] J. Kim and R. Krishnan, "High efficiency single-pulse controlled switched reluctance motor drive for high speed (48k RPM) application: analysis, design, and experimental verification," in *IEEE Industry Applications Society Annual Meeting*, Edmonton, Alberta, CA, Oct. 2008, pp. 1–8.

[60] J. Dang, S. Haghbin, Y. Du, C. Bednar, H. Liles, J. Restrepo, J. Mayor, R. Harley, and T. Habetler, "Electromagnetic design considerations for a 50,000 rpm 1kw Switched Reluctance Machine using a flux bridge," in *IEEE International Electric Machines and Drives Conference*, Chicago, IL, USA, May 2013, pp. 325–331.

[61] J. Dang and R. Harley, "Sensorless control scheme for ultra high speed switched reluctance machine," in *IEEE Energy Conversion Congress and Exposition*, Denver, CO, USA, Sep. 2013, pp. 3830–3836.

[62] H. J. Brauer and R. W. De Doncker, "Thermal modeling of a high-speed switched reluctance machine with axial air-gap flow for vacuum cleaners," in *European Conference on Power Electronics and Applications*, Birmingham, UK, Aug. 2011, pp. 1–10.

[63] L. Morel, H. Fayard, H. Vives Fos, A. Galindo, and G. Abba, "Study of ultra high speed switched reluctance motor drive," in *IEEE Industry Applications Conference*, Rome, Italy, Oct. 2000, pp. 87–92.

[64] T. Fukao, "Principles and Output Characteristics of Super High-Speed Reluctance Generator System," *IEEE Transactions on Industry Applications*, vol. IA-22, no. 4, pp. 702–707, Jul. 1986.

[65] T. Fukao, Z. Yang, and M. Matsui, "Voltage control of super high-speed reluctance generator system with a PWM voltage source converter," *IEEE Transactions on Industry Applications*, vol. 28, no. 4, pp. 880–886, Jul. 1992.

[66] S. Kachapornkul, P. Somsiri, R. Pupadubsin, N. Nulek, and N. Chayopitak, "Low cost high speed switched reluctance motor drive for supercharger applications," in *International Conference on Electrical Machines and Systems*, Sapporo, Japan, Oct. 2012, pp. 1–6.

[67] S. Kozuka, N. Tanabe, J. Asama, and A. Chiba, "Basic characteristics of 150,000r/min switched reluctance motor drive," in *IEEE Power and Energy Society General Meeting*, Pittsburgh, PA, USA, Jul. 2008, pp. 1–4.

[68] S. D. Calverley, "Design of a high-speed switched reluctance machine for automotive turbo-generator applications." Ph.D. Thesis, University of Sheffield, Oct. 2001.

[69] M. Bui, S. Schneider, S. Arnaout, and U. Schaefer, "Torque maximization of a high-speed switched reluctance starter in acceleration test," in *European Conference on Power Electronics and Applications*, Lille, France, Sep. 2013, pp. 1–11.

[70] M. D. Bui, "Maximum torque control of a high speed switched reluctance starter/generator used in more/all electric aircraft," Ph.D. Thesis, Technical University of Berlin, Berlin, Germany, Mar. 2014.

[71] S. Shoujun, L. Weiguo, and U. Schaefer, "Detailed power converter design for a 30kw switched reluctance starter/generator used in aircraft," in *European Conference on Power Electronics and Applications*, Barcelona, Spain, Sep. 2009, pp. 1–10.

[72] S. Song and W. Liu, "Load Effect on Switched Reluctance Starter/Generator System in Aircraft," *International Journal of Electrical and Power Engineering*, vol. 4, no. 1, pp. 19–26, 2010.

[73] S. Shoujun, L. Weiguo, and U. Schaefer, "Thermal analysis of a 30kw Switched Reluctance Starter/Generator system used in aircraft," in *International Conference*

on Power Engineering, Energy and Electrical Drives, Lisbon, PT, Mar. 2009, pp. 331–336.

[74] S. Shoujun, L. Weiguo, D. Peitsch, and U. Schaefer, "Detailed Design of a High Speed Switched Reluctance Starter/Generator for More/All Electric Aircraft," *Chinese Journal of Aeronautics*, vol. 23, no. 2, pp. 216–226, Apr. 2010.

[75] C. A. Ferreira, S. R. Jones, W. S. Heglund, and W. D. Jones, "Detailed design of a 30-kW switched reluctance starter/generator system for a gas turbine engine application," *IEEE Transactions on Industry Applications*, vol. 31, no. 3, pp. 553–561, May 1995.

[76] S. R. MacMinn and W. Jones, "A very high speed switched-reluctance starter-generator for aircraft engine applications," in *National Aerospace and Electronics Conference*, Dayton, OH, USA, May 1989, pp. 1758–1764.

[77] S. R. MacMinn and J. W. Sember, "Control of a switched-reluctance aircraft engine starter-generator over a very wide speed range," in *Intersociety Energy Conversion Engineering Conference*, Washington, DC, USA, Aug. 1989, pp. 631–638.

[78] C. Ferreira, S. Jones, and W. Heglund, "Performance evaluation of a switched reluctance starter/generator system under constant power and capacitive type loads," in *Conference Proceedings of the Tenth Annual Applied Power Electronics Conference and Exposition*, Mar. 1995, pp. 416–424 vol.1.

[79] J. Bartolo and C. Gerada, "The electromagnetic design of a high speed, 45kw, switched reluctance machine having a novel rotor geometry for aerospace application," in *International Conference on Electrical Machines*, Berlin, Germany, Sep. 2014, pp. 2513–2519.

[80] M. Besharati, K. Pullen, J. Widmer, G. Atkinson, and V. Pickert, "Investigation of the mechanical constraints on the design of a super-high-speed Switched Reluctance Motor for automotive traction," in *International Conference on Power Electronics, Machines and Drives*, Manchester, UK, Apr. 2014, pp. 1–6.

[81] M. Besharati, J. Widmer, G. Atkinson, V. Pickert, and J. Washington, "Super-high-speed switched reluctance motor for automotive traction," in *IEEE Energy Conversion Congress and Exposition*, Sep. 2015, pp. 5241–5248.

[82] A. Radun, "High-power density switched reluctance motor drive for aerospace applications," *IEEE Transactions on Industry Applications*, vol. 28, no. 1, pp. 113–119, Jan. 1992.

[83] A. Radun, "Design considerations for the switched reluctance motor," *IEEE Transactions on Industry Applications*, vol. 31, no. 5, pp. 1079–1087, Sep. 1995.

[84] G. Gallegos-Lopez, F. Reiter, Jr., K. Rajashekara, and R. J. Krefta, "300 kW Switched Reluctance Generator for Hybrid Vehicle Applications," SAE International, Detroit, MI, USA, SAE Technical Paper 2002-01-1087, Mar. 2002.

[85] M. Greule and M. Doppelbauer, "Cascaded Design Methodology for Switched Reluctance Motors Considering Optimum Control," in *IEEE International Electric Machines & Drives Conference*, Coeur d'Alène, ID, USA, May 2015, pp. 1651–1657.

[86] E. Richter, J. P. Lyons, C. Ferreira, A. V. Radun, and E. Ruckstadter, "Initial Testing of a 250 kW Starter/Generator for Aircraft Applications," SAE International, Warrendale, PA, SAE Technical Paper 941160, Apr. 1994.

[87] A. Radun and E. Richter, "A detailed power inverter design for a 250 kW switched reluctance aircraft engine starter/generator," SAE Technical Paper, Dayton, OH, USA, Tech. Rep. 931388, Apr. 1993.

[88] C. A. Ferreira and E. Richter, "Detailed Design of a 250-kW Switched Reluctance Starter/Generator for an Aircraft Engine," SAE International, Warrendale, PA, USA, SAE Technical Paper 931389, Apr. 1993.

[89] A. Radun, C. Ferreira, and E. Richter, "Two-channel switched reluctance starter/generator results," *IEEE Transactions on Industry Applications*, vol. 34, no. 5, pp. 1026–1034, Sep. 1998.

[90] R. Krishnan, *Switched Reluctance Motor Drives: Modeling, Simulation, Analysis, Design, and Applications*, 1st ed. Boca Raton, FL: CRC Press, Jun. 2001.

[91] R. De Doncker, D. W. Pulle, and A. Veltman, *Advanced Electrical Drives*, ser. Power Systems. Dordrecht: Springer Netherlands, 2011.

[92] A. Schoppa, H. Louis, F. Pude, and C. von Rad, "Influence of abrasive waterjet cutting on the magnetic properties of non-oriented electrical steels," *Journal of Magnetism and Magnetic Materials*, vol. 254–255, pp. 370–372, Jan. 2003.

[93] A. Schoppa, J. Schneider, and J. O. Roth, "Influence of the cutting process on the magnetic properties of non-oriented electrical steels," *Journal of Magnetism and Magnetic Materials*, vol. 215–216, pp. 100–102, Jun. 2000.

[94] A. Schoppa, J. Schneider, and C. D. Wuppermann, "Influence of the manufacturing process on the magnetic properties of non-oriented electrical steels," *Journal of Magnetism and Magnetic Materials*, vol. 215–216, pp. 74–78, Jun. 2000.

[95] M. Bali and A. Muetze, "Influence of Different Cutting Techniques on the Magnetic Characteristics of Electrical Steels Determined by a Remagraph," in *IEEE International Electric Machines and Drives Conference*, Coeur d'Alène, ID, USA, May 2015, pp. 1190–1196.

[96] F. J. G. Landgraf and M. Emura, "Losses and permeability improvement by stress relieving fully processed electrical steels with previous small deformations," *Journal of Magnetism and Magnetic Materials*, vol. 242–245, Part 1, pp. 152–156, Apr. 2002.

[97] C. Carstensen, "Eddy Currents in Windings of Switched Reluctance Machines," PhD Thesis, RWTH Aachen University, Aachen, Germany, Nov. 2007.

[98] "Hiperco® 50a Alloy." [Online]. Available: http://cartech.ides.com/datasheet.aspx?i=103&e=199&c=TechArt (Accessed Jun. 22, 2016).

[99] G. B. Kliman and E. Richter, "Construction of reluctance motors," U.S. Patent US5 053 666 A, Oct., 1991.

[100] H. Li, E. Fairall, B. Bilgin, and A. Emadi, "Performance Evaluation of a High-Speed High-Power Switched Reluctance Motor Drive," in *IEEE Applied Power Electronics Conference*, Charlotte, NC, USA, Mar. 2015, pp. 1337–1342.

[101] A. Radun, J. Rulison, and P. Sanza, "Switched reluctance starter/generator," SAE International, Anaheim, CA, USA, SAE Technical Paper 921974, Oct. 1992.

[102] A. Radun and J. Nairus, "MCT inverter/converter for the integral starter/generator," in *Intersociety Energy Conversion Engineering Conference*, Hololulu, HI, USA, Jul. 1997, pp. 585–590.

[103] A. V. Radun and Y. Q. Xiang, "Switched Reluctance Starter/Generator System Modeling Results," SAE International, Warrendale, PA, USA, SAE Technical Paper 951407, May 1995.

[104] D.-H. Lee, H. Wang, and J.-W. Ahn, "An advanced multi-level converter for four-phase SRM drive," in *IEEE Power Electronics Specialists Conference*, Rhodes, Greece, Jun. 2008, pp. 2050–2056.

[105] "Singlsyn VR Type Resolver." [Online]. Available: http://www.tamagawa-seiki.com/pdf/download/1570n13ej_shusei.pdf (Accessed Jun. 11, 2016).

[106] S. Jones and B. Drager, "Performance of a high-speed switched reluctance starter/generator system using electronic position sensing," in *Conference Record of the 1995 IEEE Industry Applications Conference Thirtieth IAS Annual Meeting*, vol. 1, Orlando, FL, USA, Oct. 1995, pp. 249–253.

[107] "Vehicle Technologies Program - Multi-Year Program Plan 2011-2015," U.S. Department of Energy, Tech. Rep., Dec. 2010.

[108] E. J. Hearn, "Chapter 4 - Rings, Discs and Cylinders Subjected to Rotation and Thermal Gradients," in *Mechanics of Materials 2*, 3rd ed., E. J. Hearn, Ed. Oxford: Butterworth-Heinemann, 1997, pp. 117–140.

[109] J. E. Vrancik, "Prediction of Windage Power Loss in Alternators," Lewis Research Center, Cleveland, OH, USA, NASA Technical Note TN D-4849, Oct. 1968.

[110] S. Calverley, G. Jewell, and R. Saunders, "Calculation of centrifugal stress in four-pole switched-reluctance rotors," *IEE Electric Power Applications*, vol. 150, no. 1, pp. 97–105, Jan. 2003.

[111] "HI-LITE NO27," Mar. 2016. [Online]. Available: http://cogent-power.com/cms-data/downloads/Hi-Lite_NO27.pdf (Accessed Jun. 22, 2016).

[112] H. Wang, "Experimental study of vibrational behavior of laminated annular disks," *The Journal of the Acoustical Society of America*, vol. 111, no. 4, pp. 1701–1708, Apr. 2002.

[113] "301 Stainless Steel Product Datasheet," 2007. [Online]. Available: http://www.aksteel.com/pdf/markets_products/stainless/austenitic/301_data_sheet.pdf (Accessed Jun. 10, 2016).

[114] K. Kiyota, T. Kakishima, and A. Chiba, "Estimation and comparison of the windage loss of a 60 kW Switched Reluctance Motor for hybrid electric vehicles," in *International Power Electronics Conference*, Hiroshima, Japan, May 2014, pp. 3513–3518.

[115] J. M. Vance, F. Y. Zeidan, and B. Murphy, *Machinery Vibration and Rotordynamics*. John Wiley & Sons, Jun. 2010.

[116] S. Singhal, K. Singh, and A. Hyder, "Effect of laminated core on rotor mode shape of large high speed induction motor," in *IEEE International Electric Machines & Drives Conference*, Niagara Falls, ON, CA, May 2011, pp. 1557–1562.

[117] G. Mogenier, R. Dufour, G. Ferraris-Besso, L. Durantay, and N. Barras, "Identification of Lamination Stack Properties: Application to High-Speed Induction Motors," *IEEE Transactions on Industrial Electronics*, vol. 57, no. 1, pp. 281–287, Jan. 2010.

[118] M. Butner, B. Murphy, and R. Akian, "The Influence of Mounting Compliance and Operating Conditions on the Radial Stiffness of Ball Bearings: Analytic and Test

Results," in *Rotating Machinery and Vehicle Dynamics*, vol. 35, Miami, Florida, USA, Sep. 1991, pp. 155–162.

[119] Y. Guo and R. G. Parker, "Stiffness matrix calculation of rolling element bearings using a finite element/contact mechanics model," *Mechanism and Machine Theory*, vol. 51, pp. 32–45, May 2012.

[120] J. A. Wensing, "On the dynamics of ball bearings," PhD Thesis, University of Twente, Enschede, The Netherlands, Dec. 1998.

[121] "AK Steel." [Online]. Available: http://www.aksteel.com/ (Accessed Feb. 12, 2017).

[122] "Cogent." [Online]. Available: http://www.cogentpowerinc.com (Accessed Feb. 12, 2017).

[123] N. Schofield, S. A. Long, D. Howe, and M. McClelland, "Design of a Switched Reluctance Machine for Extended Speed Operation," *IEEE Transactions on Industry Applications*, vol. 45, no. 1, pp. 116–122, Jan. 2009.

[124] N. Schofield and S. Long, "Generator Operation of a Switched Reluctance Starter/Generator at Extended Speeds," *IEEE Transactions on Vehicular Technology*, vol. 58, no. 1, pp. 48–56, Jan. 2009.

[125] F. Peng, J. Lin, J. Ye, and A. Emadi, "Optimal calculation method for control of switched reluctance motor," in *IEEE Transportation Electrification Conference and Expo*, Dearborn, MI, USA, Jun. 2015, pp. 1–6.

[126] W. Zhang and T. Jahns, "Analytical 2-D slot model for predicting AC losses in bar-wound machine windings due to armature reaction," in *IEEE Transportation Electrification Conference and Expo*, Dearborn, MI, USA, Jun. 2014, pp. 1–6.

[127] M. Torrent, P. Andrada, B. Blanqué, E. Martinez, J. I. Perat, and J. A. Sanchez, "Method for estimating core losses in switched reluctance motors," *European Transactions on Electrical Power*, vol. 21, no. 1, pp. 757–771, Jan. 2011.

[128] V. Raulin, A. Radun, and I. Husain, "Modeling of losses in switched reluctance machines," *IEEE Transactions on Industry Applications*, vol. 40, no. 6, pp. 1560–1569, Nov. 2004.

[129] A. V. Radun, "Development of Dynamic Magnetic Circuit Models Including Iron Saturation and Losses," *IEEE Transactions on Magnetics*, vol. 50, no. 5, pp. 1–10, May 2014.

[130] K. Narita, "JMAG Newsletter," Mar. 2014. [Online]. Available: http://www.jmag-international.com/newsletter/201403/06.html (Accessed Jun. 3, 2016).

[131] Z. Xu, A. La Rocca, S. J. Pickering, C. Eastwick, C. Gerada, and S. Bozhko, "Mechanical and Thermal Design of an Aeroengine Starter/Generator," in *IEEE International Electric Machines & Drives Conference*, Coeur d'Alène, ID, USA, May 2015, pp. 1607–1613.

[132] D. C. Giancoli, *Physics for Scientists and Engineers with Modern Physics*. Pearson Prentice Hall, 2008.

[133] "304/304l Stainless Steel Data Sheet." [Online]. Available: http://www.aksteel.com/pdf/markets_products/stainless/austenitic/304_304l_data_sheet.pdf (Accessed Apr. 8, 2016).

[134] S. D. Pawar, P. Murugavel, and D. M. Lal, "Effect of relative humidity and sea level pressure on electrical conductivity of air over Indian Ocean," *Journal of Geophysical Research: Atmospheres*, vol. 114, no. D2, pp. 1–8, Jan. 2009.

[135] "Properties Handbook: Teflon PTFE." [Online]. Available: http://www.rjchase.com/ptfe_handbook.pdf (Accessed Apr. 8, 2016).

[136] J. Lindstrom, "Development of an experimental permanent-magnet motor drive." Licentiate of Engineering, Chalmers University of Technology, Goteborg, Sweden, Apr. 1999.

[137] J. Hanrahan and G. Neal, "Component performance advantages realized through thermoplastic encapsulation," in *Electrical Insulation Conference and Electrical Manufacturing and Coil Winding Conference*, Cincinnati, OH, USA, Oct. 2001, pp. 297–300.

[138] S. Nategh, A. Krings, O. Wallmark, and M. Leksell, "Evaluation of Impregnation Materials for Thermal Management of Liquid-Cooled Electric Machines," *IEEE Transactions on Industrial Electronics*, vol. 61, no. 11, pp. 5956–5965, Nov. 2014.

[139] H. Li, K. W. Klontz, and D. Barber, "Thermal models and electrical machine performance improvement using encapsulation material," in *IEEE International Electric Machines Drives Conference*, Coeur d'Alène, ID, USA, May 2015, pp. 1336–1341.

[140] C. Rhebergen, B. Bilgin, A. Emadi, E. Rowan, and J. Lo, "Enhancement of electric motor thermal management through axial cooling methods: A materials approach," in *IEEE Energy Conversion Congress and Exposition*, Montreal, QC, CA, Sep. 2015, pp. 5682–5688.

[141] C. Rheberhegen, "The Importance of Electric Motor Thermal Management and the Role of Polymer Composites in Axial Cooling," M.S., McMaster University, Hamilton, ON, CA, Jul. 2015.

[142] J. Bao, Y. Yi, H. Wang, and J. Liu, "Comprehensive analysis of novel three-phase 12/10 switched reluctance motor," in *International Conference on Electrical Machines and Systems*, Busan, Korea, Oct. 2013, pp. 592–596.

[143] T. J. E. Miller, *Switched Reluctance Motors and Their Control*. Hillsboro, OH : Oxford: Clarendon Press, Aug. 1993.

[144] M. Khor and R. Sotudeh, "A 3-phase 12/10 asymmetrical switched reluctance motor," in *2005 European Conference on Power Electronics and Applications*, Sep. 2005, pp. 9 pp.–P.9.

[145] T. Guo, "Double Rotor Switched Reluctance Machine With Segmented Rotors," Master's Thesis, McMaster University, Hamilton, Ontario, Dec. 2014.

[146] R. Pupadubsin, S. Widmer, and B. Mecrow, "Comparison of Vibration and Magnetic Force Behaviours between Different Switched Reluctance Machine Topologies," in *IEEE International Electric Machines & Drives Conference*, Coeur d'Alène, ID, USA, May 2015, pp. 1373–1379.

[147] C. Tuncay, "Segmented Rotor Switched Reluctance Drives," Ph.D. Thesis, University of Newcastle, Newcastle upon Tyne, England, Aug. 2011.

[148] B. C. Mecrow, E. A. El-Kharashi, J. W. Finch, and A. G. Jack, "Preliminary performance evaluation of switched reluctance motors with segmental rotors," *IEEE Transactions on Energy Conversion*, vol. 19, no. 4, pp. 679–686, Dec. 2004.

[149] M. Tanujaya, D.-H. Lee, Y.-J. An, and J.-W. Ahn, "Design and analysis of a novel 4/5 two-phase switched reluctance motor," in *International Conference on Electrical Machines and Systems*, Beijing, China, 2011, pp. 1–6.

[150] F. Peng, “Three-Level Switched Reluctance Motor Drive and Control,” Ph.D. dissertation, McMaster University, Hamilton, ON, CA, 2016.